Computational Studies of Vitrimers, Semicrystalline Polymers and Metals: Deformation, Actuation and Fabrication

by

Gurmeet Singh

A dissertation submitted in partial fulfillment
of the requirements for the degree of
Doctor of Philosophy
(Aerospace Engineering and Scientific Computing)
in the University of Michigan
2023

Doctoral Committee:

Professor Veera Sundararaghavan, Chair
Dr. Umesh Gandhi, Toyota
Professor Daniel J. Inman
Professor John Kieffer

Gurmeet Singh

gmsingh@umich.edu

ORCID iD: 0000-0002-0845-6745

"Insight must precede application"– Max Planck

ACKNOWLEDGEMENTS

Firstly, I would like to express my sincere gratitude to my advisor, Prof. Veera Sundararaghavan. He introduced me to this exciting area of research. He gave me full liberty to pursue problems that I was interested in and gave me time and guidance whenever I needed them. I'd like to thank my committee members, Professors Daniel Inman, John Kieffer, and Dr. Umesh Gandhi from Toyota, for taking the time to review my work. Their invaluable suggestions and feedback have refined this work and also helped sprout ideas for future work. I would also like to thank my collaborators for their insightful discussions and research support: Dr. Vikas Varshney from AFRL, Prof. Sameh Tawfick and his research group from UIUC, and Mr. Ahmad Sheikh from IISc Bangalore, India.

I am grateful for the opportunity to learn from some of the great teachers at UofM, Prof. John Shaw's Mechanics of Elastic Stability, and Prof. Krzysztof Fidkowski's Computational Fluid Dynamics taught me a great deal about these subjects. I would also like to thank my M. Tech. thesis supervisor, Prof. P.M. Mohite from IIT Kanpur for teaching courses and introducing me to research in the field of Solid Mechanics.

I would like to thank my friends: Deepam, Deepak, Srihari, Alex, Aaditya, Siddhartha, Srinivasan, Harsh, Vishnu, Kunal, Xiaosong, and Iman. Their support has played a crucial role in this long and arduous journey. I am thankful to former MSSL group members for their guidance and support: Shardul, Sriram, Pinar, and Abhishek. I would like to acknowledge the support of Angela Farrehi of C.A.R.E. Center and Denise Phelps of Aero during the harder period of my PhD journey. I

would also like to thank my colleagues at Toyota Research Institute North America for their support and help in the last year of my PhD research: Paul, Mizuho-san, Shimokawa-san, Yuyang, Parveen and Royan.

Finally, my family has been my constant source of love and support in this journey, and I owe them my deepest gratitude. I thank my parents for their unwavering encouragement and sacrifice, even when they faced difficulties in their lives. I acknowledge the invaluable help of my brothers, Pawan and Vikram, my sisters-in-law, Rekha and Aarti, my sister Sunita and my brother-in-law, Sanjeev, and the joy of having my nieces and nephews around. I also express my sincere appreciation to my elder brother, mentor, and guru, Rupinder Kumar for inspiring me to pursue science since high school and guiding me to where I am today. Finally, I cherish Deepa, who will soon join me as my life partner, for her companionship and support throughout the past decade.

I also acknowledge the following for financial support: François-Xavier Bagnoud (FXB) Fellowship, Mr. and Mrs. Milo E. Oliphant Fellowship, Rackham Predoctoral Fellowship, MICDE fellowship, PRISMS Center (DOE) funding, and Rackham Travel grant. I would like to acknowledge the Advanced Research Computing at the University of Michigan for their computational resources throughout this work.

TABLE OF CONTENTS

LIST OF FIGURES

Figure

LIST OF TABLES

Table

ABSTRACT

Molecular dynamics (MD) provides valuable insights into the structure, dynamics, and properties of materials, especially when experimental data is scarce or difficult to obtain. In this thesis, we use MD simulations to study three classes of materials: vitrimers, semicrystalline polymers, and metals. These materials exhibit diverse and complex behaviors under thermal and mechanical loads.

Vitrimers are a promising alternative material system that has been recently designed to address the non-recyclability of thermoset plastics. In vitrimers, dynamic cross-links allow for malleability under thermal stimuli. Despite their several advantages, the lack of understanding of their mechanical response has limited the widespread use of these materials for aerospace applications. In this thesis, we develop a capability to simulate dynamic cross-linking reactions of vitrimers under general thermomechanical loading conditions using a topological reaction scheme within MD. We demonstrate the application of the model towards damage healing of a vitrimer system at the molecular level. The work will allow us to: (1) develop innovative computational models of the complex interplay between chemistry and mechanics in vitrimers, (2) link the evolution of thermomechanical properties to underlying molecular mechanisms, and (3) understand the molecular-scale mechanisms of the creep behavior of vitrimers which is hard to characterize by experiments.

Another application studied is the simulation of semicrystalline polymer-based twisted and coiled polymer actuators (TCPA). These actuators can achieve large actuation strokes by exploiting the material anisotropy due to the amorphous and crystalline

phases of Nylon. An all-atom molecular dynamics (MD) simulation is used to investigate the thermal behavior of the two phases and to determine their coefficients of thermal expansion (CTE) and glass-transition temperature, separately. Based on this data, we develop a finite element model for TCPA and validate the results against experimental data. The model is used to explore the effects of actuator parameters such as chirality, twist angle, and material anisotropy on the actuation performance. The CTE anisotropy is found to be the dominant factor as compared to the elasticity tensor for the large actuation. This study provides a comprehensive understanding of the physics of TCPA and provides directions for their optimization and performance. The final application studied is Additive manufacturing (AM) of metal parts. Additive manufacturing involves a gradual modification in the size and shape of solids due to the addition of new layers of the material on top of the existing ones that result in large thermal gradients under non–equilibrium phenomena. Atomistic simulations are used to model the additive manufacturing process at the nanoscale to establish process-property correlations. To this end, we study the evolution of defect structure as a function of process parameters: cooling time, melt thickness, substrate temperature, and soft vs. hard inclusions. We find that the defect content can be significantly reduced by raising the temperature of the powder bed to a critical temperature. A critical advantage of this approach is that simulations can be used to perform alloy design, as demonstrated by simulating the effect of the addition of a hard and soft inclusion on the defect structure.

CHAPTER I

Introduction

1.1 Motivation

This dissertation provides insights from computational studies of three materials systems investigated using all-atom molecular dynamics simulations. The material systems are explained below:

1.1.1 Properties of vitrimers

Polymers are categorized into broadly two types, based on their ability to be reformed: thermoplastics and thermosets. They both are made of long chains of molecules. However, they have different physical and chemical properties, and they show different behaviors when exposed to heat. Thermoplastics can be melted and reshaped by heating them after they are cured, which means they can be recycled and reused for different purposes. This is due to the long chains they form during curing that form a solid structure as a result of the non-bonding interaction of inter-chain positions [4, 5, 6, 7, 8]. Thermoset polymers, on the other hand, form strong chemical bonds between the polymer chains when they are cured, which makes them hard and rigid. Owing to their 3D rigid network of molecular chains, they cannot be melted or reshaped by heating them again, which means they are more durable and resistant to high temperatures, but also more difficult to recycle. Figure 1.1 shows the schematic of

the difference in inter and intra-chain connections in thermoplastics and thermosets. Some examples of thermoplastics are polyethylene, polypropylene, polystyrene, and nylon. Some examples of thermoset polymers are bakelite, epoxy, polyester, and vulcanized rubber.

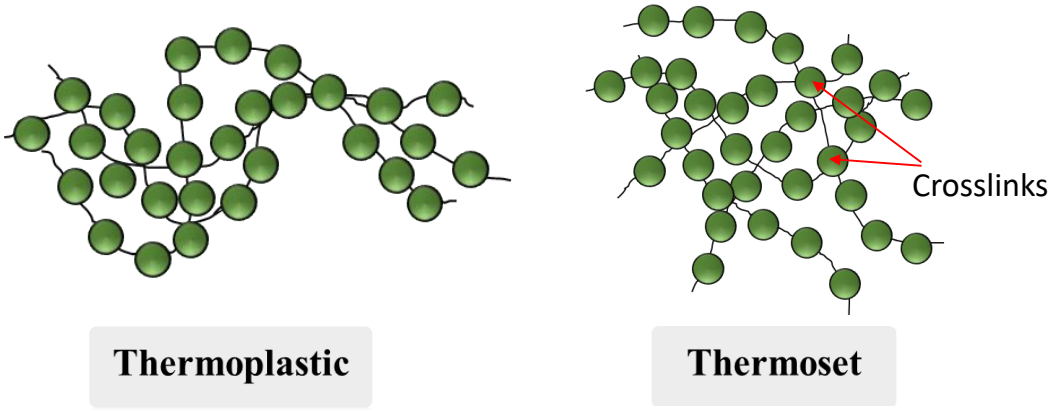

Figure 1.1: Difference in inter and intra–chain connections between thermoplastics (on left) and crosslinks in thermosets(right)

Thermoset polymers, such as epoxies, offer great mechanical strength, high-temperature tolerance, and chemical stability, which makes them an ideal candidate for automotive and aerospace applications. However, their inability to melt or reform makes them extremely challenging to recycle or manage their waste toward the end of their life cycle [9, 10]. Their conventional alternative, thermoplastic polymers, do not match their performance in critical applications. Therefore, an alternative was designed by using a new chemistry, vitrimers [11, 12, 13]. These are a new class of polymers that offers the best of both kinds: the strength and performance of an epoxy, and the malleability and reformability of a thermoplastic. They have a 3D crosslinked network when cured, however, they have special sites where they can exchange bonds when heated beyond a certain temperature (referred to as vitrimer topology freezing temperature). They achieve malleability beyond this temperature by means of adaptable covalent bonds, which means the network has the same number of bonds even after such bond swaps take place, therefore retaining the topology of the solid.

An example of a dynamic bond exchange reaction is shown in Figure 1.2. In this case, two chain segments A–B and C–D lead to a reformed network segments C–B and A–D as a result of a disulfide-based dynamics bond exchange reaction. This is how a 3D crosslinked polymer network achieves malleability in a vitrimer system. There are other types of chemistry that lead to swappable covalent adaptable networks such as amines[14, 15], transesterification reactions[16], Diels-Alder reaction [17], radical formation[18], etc. Vitrimers have been recently incorporated in carbon fiber composites[19, 20] and nanocomposites[21] which expands their scope of applications in performance-critical environments.

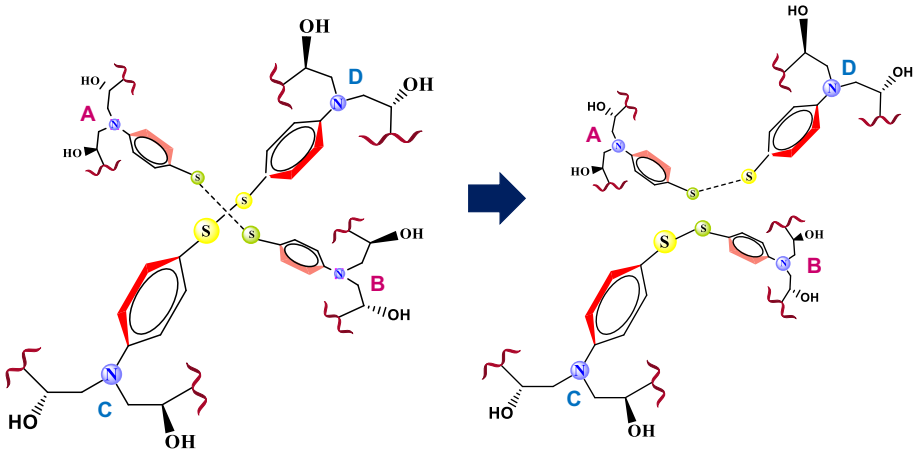

Figure 1.2: An example of dynamic bond exchange reaction in a vitrimer where chains A–B and C–D result in chains C–B and A–D

Vitrimers offer a great advantage of reformability with a thermoset-like performance, however, it comes with a cost, and they are more prone to creep as compared to their thermoset counterparts. Vitrimers' DBER accelerates beyond a temperature or in the presence of a catalyst under which they become malleable, however, even at lower temperatures, a fraction of these reactions can take place and result in some creep behavior. Managing their creep and viscoelastic response is an important aspect in order to utilize these new class polymers well in high-performance applications such as aerospace components. The present work focuses on developing a computational

framework to model and understand the thermomechanical response of vitrimers. Specifically, we study the self-healing behavior and creep behavior of the vitrimer system using nanoscale simulations of vitrimers in Chapter II and III, respectively.

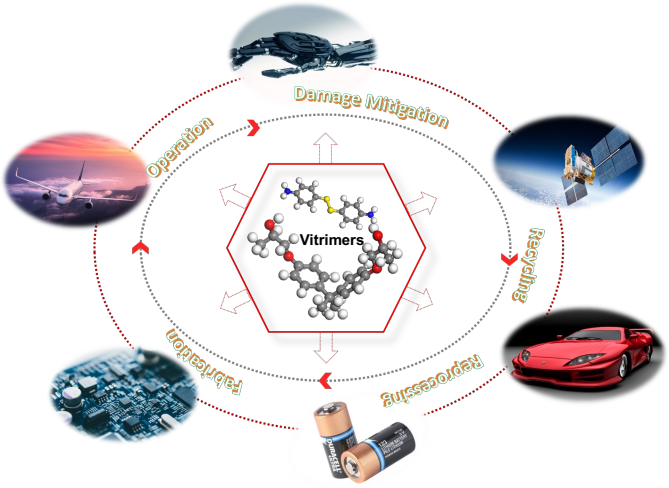

Figure 1.3: Application space of vitrimers towards sustainability

1.1.2 Semi-crystalline polymers-based actuators

Actuation is important to convert different forms of energy to mechanical work. They can be powered by different sources of energy, such as electricity, hydraulics, pneumatics, or human power [22]. Some examples of actuators are electric motors, solenoids, hard drive stepper motors, comb drives, etc. There are different types of actuation approaches developed over the past few decades toward mechanisms or systems, such as valves, switches, robots, and machines. Nickel-Titanium (NiTi) alloy based has been one of the prominent choices for developing high-speed actuators [23, 24].

Polymers are long chains of molecular segments which are bonded via van der Waals forces, covalent bonds, or hydrogen bonds[5, 25]. They usually form randomly ordered bulk (amorphous), however, some polymers can form ordered regions due to hydrogen bonds for instance. These are referred to as semi-crystalline polymers that have both ordered and disordered regions in their molecular structure. The ordered regions are

called crystallites or lamellae, which form larger structures called spherulites[1, 26, 25]. The disordered regions are called amorphous. Semi-crystalline polymers can crystallize from melt, stretching, or solvent evaporation [27, 28]. The degree of crystallinity affects the optical, mechanical, thermal, and chemical properties of the polymer. Some examples of semi-crystalline polymers are Nylon, polyethylene, polypropylene, polyethylene terephthalate, polytetrafluoroethylene, etc. Semi-crystalline polymers are used to make fibers, films, blends, and composites for industrial use [25, 29, 30]. Other areas of applications include packaging materials, such as polyethylene terephthalate bottles, and engineering plastics, such as polytetrafluoroethylene for non-stick coatings and electrical insulation[30].

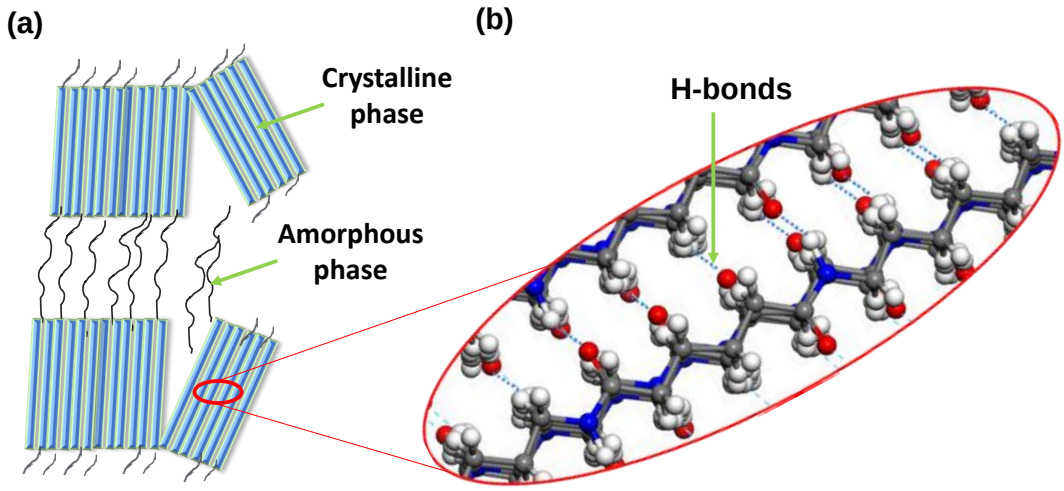

Figure 1.4: (a) Phase-wise realignment in a highly drawn semi-crystalline polymer fiber and (b) ordered phase with H-bonding in Nylon 6,6

Despite having an anisotopic crystalline phase, semi-crystalline polymers demonstrate an isotropic at a macroscopic scale due to the random orientation of the ordered phase uniformly in 3D space. However, semi-crystalline polymer, when drawn, is formed into monofilament fiber that results in the alignment of the crystalline phase along the fiber axis. This realignment leads to transversely isotropic properties of the drawn fiber (shown in Figure 1.4). This property of drawn fibers, such as in fishing

line (Nylon 6,6 or Polyethylene), is harnessed to develop large stroke twisted and coiled polymer actuators (TCPA) [31, 32]. Modeling the physics involved in these actuators is one of the focuses of this work. The detailed description of a multi-scale computational framework developed to investigate the actuation mechanisms of these actuators is discussed in Chapter IV.

1.1.3 Metal additive manufacturing

Additive manufacturing (AM) is now being routinely used in the industry to build metal parts due to the flexibility it allows in part design. Additive manufacturing involves a gradual increase in the size and shape of solids due to the addition of new layers of the material on top of the existing ones. Thermally enabled metal additive manufacturing (MAM) consists of fast heating (e.g. using lasers) of the powder beds leading to large thermal gradients followed by high cooling rates due to the small volumes that are exposed at a time [33, 34]. A resolution of up to 20 μm per layer [35] and components with functionally graded materials has been realized [36]. The defect formation during additive manufacturing is a subject of ongoing in-depth studies as it relates to the accelerated fatigue and fracture of a manufactured part [37]. There is a high dependence on several processing parameters which dictates the mechanism and properties of the final product [38, 34, 39, 40]. Wang et al. studied the influence of both the laser scan rate and laser power on the residual stresses in the fabricated samples [41, 42]. Their findings revealed that higher laser power led to an increase in the residual stress in the build direction and laser speed influences the stresses in transverse directions of the additive sample [42]. Figure 1.5 shows a schematic of the metal additive manufacturing process (center) with a resulting representative microstructure.

To understand the microstructure evolution and defect formation as a function of process parameters, it is important to comprehend the solidification processes in the

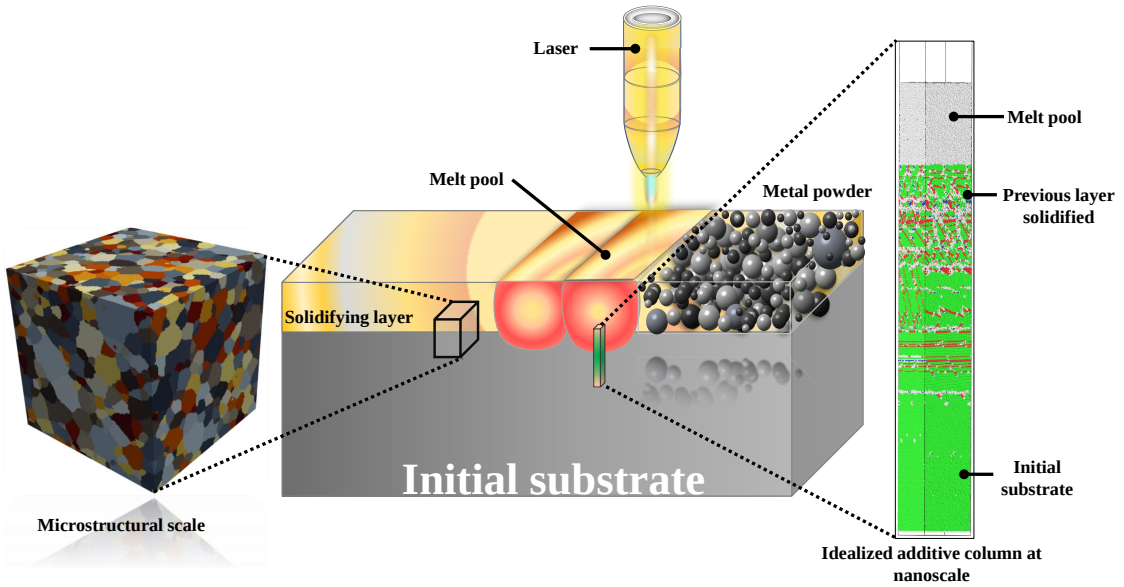

Figure 1.5: A schematic of the additive manufacturing process (center), microstructure at mesoscale (center), and the idealized additive process at the nanoscale (right)

melt and how it influences the defect structure in an additive column. Several simulation methods have been applied to study the solidification phenomenon at different scales [43, 44]. Cellular automata in conjunction with temperature history from a finite element analysis (FEA) [45], finite volume [46], or finite difference solutions [47] have been implemented to predict the grain size and texture during solidification under arc welding or additive manufacturing process. A continuum scale model by Prabhakar et al. [48] was implemented that employs FEA and thermal history to simulate the deformation and distortion of the part. Another popular choice for simulating structure at meso scales is phase–field (PF) modeling [49, 50]. However, because of the length scale and extreme heating and cooling rates, melt solidification is a highly non-equilibrium process, and continuum methods alone are not sufficient. During the solidification of grains, various defect structures form that are either unstable (e.g. self–interstitial) which are relieved during reheating, or more stable defect structures (e.g. high angle grain boundaries) that persist after the process. Understanding the formation of defects as a function of parameters such as cooling rates,

particle bed temperature, presence of inclusions, etc. has not yet been carried out via molecular simulations. In this work, we use molecular dynamics simulations to understand the evolution of the defects during a layer-by-layer addition of melt-pool on a solidified part. We investigate the process-parameter dependence on such defect structures, the simulation methods, results, and fundamental insights are discussed in Chapter V.

1.2 Molecular Dynamics Modeling

1.2.1 Overview of Molecular Dynamics

The core idea of classical molecular dynamics simulations is that the trajectories of particles are solved by evolving a dynamical system over time. These particles can be atoms, a group of atoms (beads in coarse-grained modeling). Consider a system of particles in three-dimensional space where each particle has three degrees of freedom. Therefore, the entire system has $6N$ degrees of freedom where $3N$ spatial positions and $3N$ velocities for N particles in the system. Each particle is described using a spatial position and a velocity, hence the system can take many states with particles having different values in this six degrees of freedom space which are referred to as phase space or state space of a dynamical system. Newton's second law can be written for each particle in vector form:

$$m\mathbf{a} = \mathbf{F}(\mathbf{r}) = -\nabla V(\mathbf{r}) \tag{1.1}$$

where m is the mass of the particle, $\mathbf{a}$ and $\mathbf{F}(\mathbf{r})$ are the acceleration and force acting of the particles, respectively. ∇ denotes the gradient operator, and V is the potential energy of the particle as a result of the interaction with the rest of the system. Note that the potential and force depend on the position vector ($\mathbf{r}$) of the particle. The force on a particle is computed using the sum of the forces exerted due to the

interaction with all other particles. Evaluating interaction due to all particles is a computationally expensive task, therefore, the region of interaction is truncated to a finite spherical (or circular in two-dimension) subdomain. The force on a particle due to other neighboring particles in the defined region of influence can be written as a gradient of potential energy (V) due to the interaction among those particles. The potential energy of a particle is computed using the defined interaction referred to as interparticle or interatomic potentials and will be discussed in the following subsection. The system of particles is given an initial position and velocities, then considering Eqn. 1.1 for all particles leads to a total of $6N$ equations that are not easy to solve exactly, therefore, are solved numerically and will be discussed in the next subsection. The series of key steps followed in MD simulations is shown in Figure 1.6.

1.2.2 Ergodic Hypothesis

Another important idea used in evaluating the properties of interest in MD simulations is the Ergodicity of the system. The Ergodic Hypothesis is a concept in physics and thermodynamics that relates the time average and the ensemble average of an observable property of a system [51]. It states that for a system with a fixed energy, the time spent by the system in a region of its phase space is proportional to the volume of that region. This means that all possible states of the system with the same energy are equally likely to occur over a long period of time. It also means that the average of a property over time is the same as the average over many copies of the system. The Ergodic Hypothesis is useful for some problems in physics and thermodynamics, but not all systems follow it. Some systems may have different behaviors depending on their initial conditions or external factors. We assume the Ergodic hypothesis holds true for our MD simulations in this work.

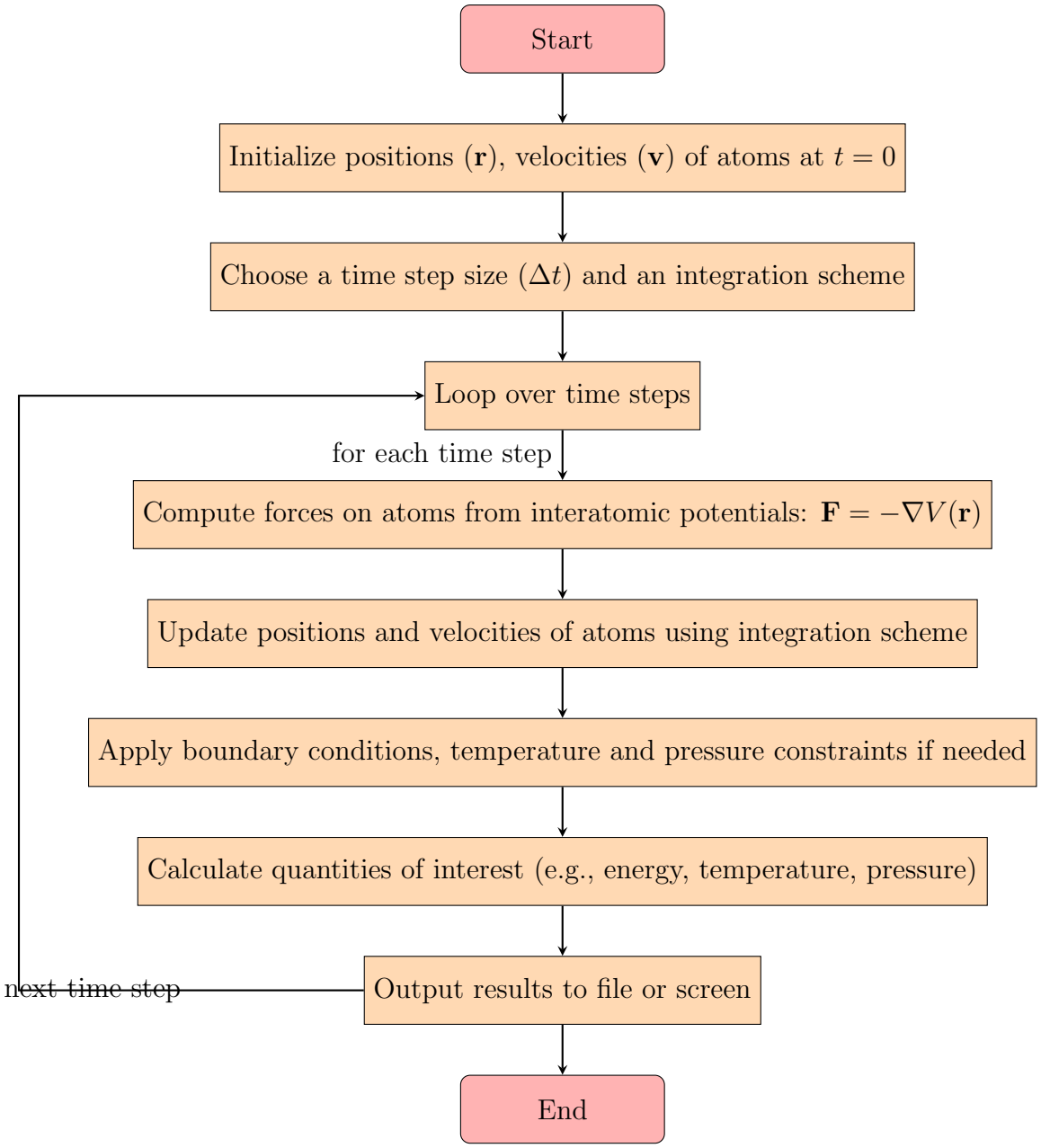

Figure 1.6: Flow of the steps followed in a typical molecular dynamic simulation

1.2.3 Time integration Schemes

In classical MD simulations, Newton's equations of motion are solved for a system of particles. The system is initialized with their positions and velocities. The equations are solved numerically by using time integration schemes with finite discretized steps. Owing to its order of accuracy, the most popular position integration algorithm is

Velocity Verlet [52, 53]. This algorithm is used to find the direction and distance that particles move given some time-step. The Velocity Verlet algorithm can be derived from a Taylor series expansion of the position function. Eqn. 1.1 can be reconsidered in terms of the second-order differential equation in position vector:

$$\ddot{\mathbf{r}} = \mathbf{a} \tag{1.2}$$

where $<\dot{}>$ represents a time derivative and $\mathbf{a} = \mathbf{F}/m$ with initial conditions $\mathbf{r}(t_0) = \mathbf{r}_0,\ \dot{\mathbf{r}}(t_0) = \mathbf{v}_0$. The velocity Verlet algorithm updates the positions and velocities of the particles following equations of motion shown in Eqn. 1.2:

$$\mathbf{r}(t + \Delta t) = \mathbf{r}(t) + \mathbf{v}(t)\Delta + \frac{1}{2}\mathbf{a}(t)\Delta t^2 \tag{1.3}$$

$$\mathbf{v}(t + \Delta t) = \mathbf{v}(t) + \frac{\mathbf{a}(t) + \mathbf{a}(t + \Delta t)}{2}\Delta t^2 \tag{1.4}$$

where Δt represents the time step (temporal discretization). Note that the position update requires the information of the system at previous time steps, however, velocity requires the acceleration at the next time step to update the velocity at that time step (Eqn. 1.4). The acceleration at $t + \Delta t$ can be evaluated from the updated positions and hence using the force from Eqn. 1.1. This algorithm assumes that acceleration $\mathbf{a}(t+\Delta t)$ only depends on position $\mathbf{r}(t+\Delta t)$ and does not depend on velocity $\mathbf{v}(t+\Delta t)$.

1.2.4 Interatomic potentials

For MD simulations, the interatomic interactions are dictated by the choice of a *force field* which describes the evaluation of the potential energy of an atom in the presence of the neighboring atoms. There have been several types of force fields developed depending on the nature of the system and the environment of interest to be simulated. For example, embedded atom model (EAM) potential is used for

metals [54], modified embedded atom method (MEAM) for metals with covalent bonding [55, 56], consistent valence force field (CVFF) for organic molecules [57, 58], Morse potential [59, 60, 61], polymer consistent force field (PCFF)[62], many-body potential [63, 64] Leonard-Jones (LJ) potential for van der Waals interaction [65], reactive potential such as reactive empirical bond order potentials (REBO) [66, 67] and ReaxFF [68, 69, 70]. These parameters for these potentials are calibrated against experiments and/or density functional theory-based *ab-intio* calculations. In this work, CVFF and PCFF are used to describe the interaction of atoms of the vitrimer and Nylon 6,6 semi-crystalline polymer, respectively. For simulating the additive metal manufacturing process at the nanoscale, we used EAM potential. The details of each of these potentials will be discussed in subsequent chapters.

1.2.5 Periodic Boundary Conditions

In any computational framework, the cost of computation increases with the degrees of freedom simulated. A simulation where each atom is modeled as a particle puts limitations on the size of the system to be simulated. Therefore, a finite system has to be constructed such that the chosen domain represents the bulk of the material. If we consider such a system that has finite ends can have different behavior than a system with larger systems with farther ends. One workout around this problem is the usage of periodic boundary conditions (PBC). PBC is a common technique to simulate bulk properties of materials or fluids using a finite number of particles. The idea is to replicate the system in all directions and assume that the particles interact with their nearest images as if they were real. This way, the effects of the boundaries are minimized and the system behaves as if it were infinite. PBC requires that the shape of the simulation box is space-filling, meaning that it can be tiled without gaps or overlaps, for example, cubic or parallelepiped boxes that can be repeated in 3-dimensions.

1.2.6 Modeling reactive systems

Modeling reactions in molecular dynamics simulations is a challenging task that requires the ability to change the bond topology of the system during the simulation. Traditional fixed valence force fields do not allow such changes and are limited to modeling systems with constant chemical composition. Reactive force fields, such as ReaxFF [70, 71, 72], Density functional theory[73], Brenner Force Field (Brenner FF)[74], reactive empirical bond order (REBO)[75] can overcome this limitation by using complex potential energy expressions that depend on bond order and distance. However, reactive force fields are difficult to parameterize and computationally expensive. Another approach is to use algorithms that can incorporate multi-step reaction mechanisms into atomistic molecular dynamics simulations using conventional force fields [76, 77]. These algorithms use predefined rules or templates to modify the bond connectivity of the system according to certain criteria, such as distance, angle, or energy. This way, they can simulate complex chemical processes such as polymerization, crosslinking, catalysis, or combustion [78].

1.3 Outline of Thesis

The focus of this thesis is to develop computational frameworks for polymers, and additively manufactured metals and enhance the understanding of the phenomenon spanning multi-scales. We look into modeling the thermomechanical response of the vitrimers while they undergo dynamic cross-linking reactions. We specifically model their self-healing phenomenon and their creep behavior under isothermal conditions. The MD simulations are able to answer the chain dynamics that result in the unique secondary creep behavior of vitrimers in contrast to conventional epoxies. In another study, we develop a multi-scale computational model of the semi-crystalline polymer-based actuators. At different scales, we look at the thermal behavior and

how it influences the actuation behavior of the twisted and coiled polymer actuators (TCPA). A continuum-scale finite element model helps understand the key characteristics of the precursor fiber that lead to such large actuation in them. In the last study, we investigated the non-equilibrium phenomenon of metal additive manufacturing at the nanoscale. We use MD simulations to look at the defect evolution in a layer-by-layer addition of melt on a solidified part. We investigate the influence of the different process parameters on the defect content in the additive column. The thesis is organized as follows:

Chapter 2 outlines the MD model of vitrimers for simulating dynamic cross-linking reactions with thermomechanical loading. We propose a temperature-dependent reaction probability to simulate the topology freezing temperature of vitrimers. We also quantify the self-healing behavior of a damaged vitrimer by comparing the recovered stiffness after undergoing a heating and cooling cycle.

Chapter 3 makes an attempt to understand the creep behavior of vitrimers. We use MD simulations to investigate the reaction mechanisms that are responsible for experimentally observed secondary creep in vitrimers. The free-volume evolution is probed for vitrimers and compared their response with epoxies. Then the chapter will conclude with the effect of loading and reaction probability or catalyst concentration on the creep response of vitrimers.

Chapter 4 details the multi-scale framework for semi-crystalline polymer-based actuation devices. The MD simulations at the nanoscale and finite element analysis at the continuum scale are conducted for the Nylon 6,6 TCPA actuator. The results from different scales are compared with experimental observations and the continuum-scale model is further used to investigate the underlying mechanisms responsible for large

actuation of TCPAs.

Chapter 5 outlines the modeling of a metal additive manufacturing (MAM) non-equilibrium phenomenon at the nanoscale. The evolution of the defect content in the process is studied as a function of the process parameters. We also look at the influence of different kinds of inclusions on the defect content in a MAM process.

Chapter 6 summarizes the main contributions and proposes future directions beyond the scope of the thesis.

CHAPTER II

Modeling Self-Healing Behavior of Vitrimers in Molecular Dynamics Simulations

Vitrimers are a special class of polymers that undergo dynamic cross-linking under thermal stimuli. Their ability to exchange covalent bonds can be harnessed to mitigate damage in a composite or to achieve recyclable aerospace composites. This work addresses the primary challenge of modeling dynamic cross-linking reactions in vitrimers during thermomechanical loading. Dynamic bond exchange reaction probability change during heating and its effect on dilatometric and mechanical response is simulated for the first time in large-scale molecular dynamics simulations. Healing of damage under thermal cycling is computed with mechanical properties predicted before and after self–healing.

2.1 Background

Thermoset polymers find applications in fields ranging from robotics, aerospace, automobile, electronics, and batteries either as is or as a part of fibrous composites [79]. There are some challenges in their usage that need to be addressed, for instance, the inability to recycle and re-process due to the irreversibility of the cross–linking bonds and damage evolution in structurally loaded components. Vitrimers are a promis-

ing alternative material system that has been recently designed to address these issues[13, 20, 80, 81, 18]. Vitrimers contain dynamic cross–links that enable them to behave like thermosets at low temperatures and behave like thermoplastics at higher temperatures [11]. This enables self–healable aerospace composites where damage can be reversed through heating, or recyclable matrix materials where the matrix can be reclaimed after use [82, 83, 79]. Numerous covalent bond exchange mechanisms have been discovered in the recent past such as amines[14, 15], transesterification reactions[16], Diels-Alder reaction [17], radical formation[18], etc. Vitrimers have been recently incorporated in carbon fiber composites[19, 20] and nanocomposites[21] which expands their scope of applications.

Molecular dynamics (MD) models of conventional thermosets have now found use in the aircraft industry. In recent years, these models have demonstrated reliable prediction of the glass transition temperature [84], gelation point[85], thermal expansion coefficient [86], thermal conductivity [87, 88, 89, 90], elastic properties [91, 92, 93], and even complete yield surface [94] without any experimental inputs allowing for computational materials design. The primary challenge for vitrimers is the presence of temperature dependent reversible cross–link reactions that dynamically alter the mechanical response. Exchange reactions have been modelled in the past via methods such as embedding Monte Carlo (MC) moves into molecular dynamics (MD) or fully MD (using specialized three body potentials) or fully MC simulations to simulate bond swaps [95, 96, 97, 98, 99]. These simulations have typically employed coarse grained models (bead–spring) that provide high computational efficiency while approximating the mechanical response. For more quantitative modelling, all–atom MD methods are attractive[100, 101], however, these methods become computationally demanding when simulating slow chemical and mechanical dynamics. Yang et al.[102] modelled bond exchange reactions in all–atom MD by implementing a distance–based reaction cutoff, which greatly accelerates the chemical dynamics. Bonds were created

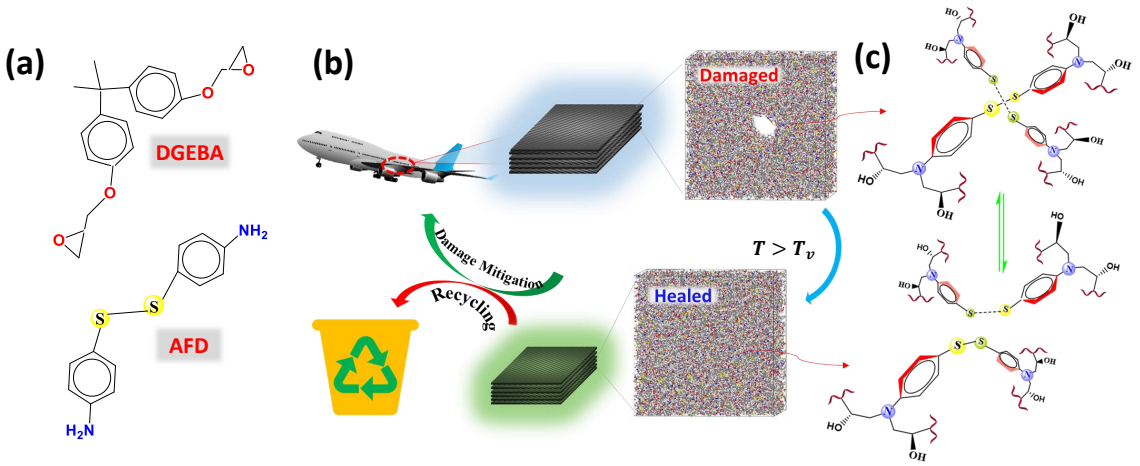

Figure 2.1: (a) Vitrimer monomer units, (b) shows the importance of vitrimer based fibrous composites towards damage mitigation and recycling during operational cycles via (c) the dynamic di-sulfide bond exchange reaction

based on the proximity of reacting atoms and the topology was accepted based on the energy of the new bond. However, the simulation had to be started with a low distance cutoff for stability considerations (to avoid large changes in energies due to initial reactions) and the cutoff was subsequently increased. In this paper, we avoid this issue using an algorithm for chemical reactions based on a pre and post–reaction templates with fixed proximity cutoff [76, 103]. Our approach employs an explicit temperature dependence of reaction probabilities drawn from experimental insights. The approach allows, for the first time, modeling of mechanical property changes in vitrimers during thermal cycling above and below topology freezing point (Tv) while demonstrating healing of damage and subsequent recovery of mechanical properties. In this work, we considered epoxy monomer diglycidyl ether of bisphenol A (DGEBA) cross-linked with 4-aminophenyl disulfide (AFD) vitrimer (structures shown in Fig. 2.1(a)). This particular system was chosen due to its ability to achieve dynamic cross-links in the absence of catalysts[104]. This isomer of AFD also demonstrates mechanochromatic behavior within the visible spectrum (due to the position of amine group at ortho position[105]) which is useful for damage detection. Further, this is

one of the few vitrimeric systems that has been integrated into a fiber composite [106]. Through reconfigurable sulfur–sulfur (S–S) linkage (Fig. 2.1(c)), the network can change its topology, preserving the number of bonds but at the same time relaxing its stresses. When the temperature decreases (cooling), the exchange reactions slow down and the network topology appears to be fixed on experimental time scales. Hence, it behaves like an elastic thermoset (elastomer). Thermoset composites are prone to damage during operation and which diminishes their performance (shown in Fig. 2.1(b)). Upon heating vitrimers above the topology freezing point, the dynamic bond exchange reactions accelerate (Fig. 2.1(c)) and the viscosity decreases due to preference towards linear chains, causing the vitrimer to become malleable. Such behavior can be used to heal damage and to recover elastic properties upon cooling back to temperatures below the topology freezing point [105]. In this paper, we have employed a temperature dependent probability model for the dynamic di-sulfide bond exchange reaction to simulate this effect.

2.2 Methods

We started with a simulated cell containing a monomer mixture with DGEBA:AFD. The typical synthetic epoxy to hardener stoichiometric ratio of 2:1 was employed [107]. We repeat this unit by $8 \times 8 \times 8$ to get a simulation box with 2,048 DGEBA and 1,024 AFD units, with a total of 68,608 atoms. Consistent valence force field (cvff) is assigned to all the atoms with pair, bond, angle, dihedral and improper coefficients modeled[57]. The non-bonded interactions are modeled using Lennard-Jones (LJ) and Coulombic pairwise interaction with a cutoff. The mixture is compressed to a liquid density of 1.0 gcm^{-3} at 300 K and 1 atm NPT. Then the mixture is cured via curing reaction modeling in LAMMPS[103]. This is not a force-field-based reaction modeling, but a bonding procedure for two atoms which mimics a chemical reaction [76] and the sites are identified by the pre– and post– reaction templates as well as on the mapping

between the two templates[76] (a schematic shown in Figure A.1 of Appendix A). The primary and secondary amine reactions are modeled with their respective reaction templates as well as their reaction maps (refer Figure A.1 of Appendix A). The cut-off distance between C and N atoms is set to be 3.5 Å and 5.0 Å for the primary and secondary amine reactions, respectively. In addition to bonding cutoff distance, a reaction probability of one was assigned for the curing reaction. The system is able to achieve up to 95% cross-linking density (Figure A.3 and A.4of Appendix A). The cured model is then annealed by heating and cooling cycles at 1 K (below T_g) and 600 K (well above T_g) under NPT conditions at 1 bar until the density converges to a $\rho = 1.18$ gcm^{-3} for neat vitrimer at 1 K (refer Figure A.5 of Appendix A). The equilibrated structure is used to further study thermo-mechanical properties and self–healing behavior under dynamic S–S bond exchange processes.

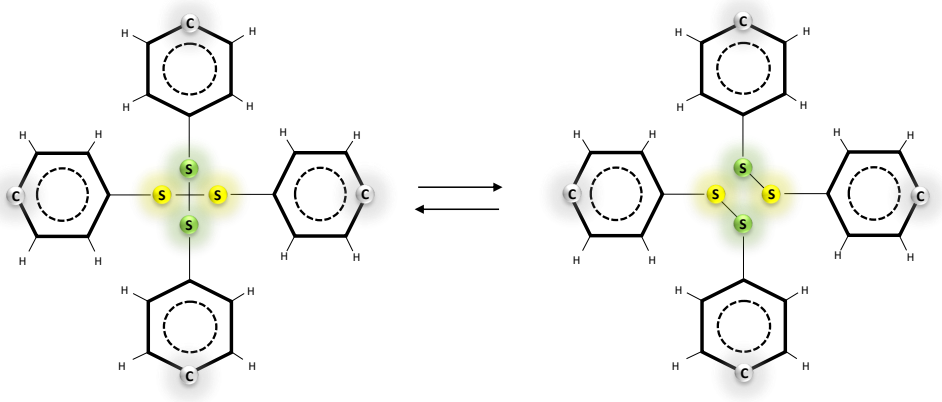

Figure 2.2: Reaction template for S-S bond exchange reaction of the vitrimer with pre (on left) and post (on right) reaction templates (each contains 44 atoms). One green and one yellow colored sulfur are the initiator or bonding atoms, and the C atoms shown here denote the edge atom in the templates

The dynamic S–S bond exchange process is modeled in terms of two-step reactions. A pre– and post–reaction templates are constructed for both reactions along with a reaction map (refer Figure 2.2). When two pairs of di-sulfide sites come together, they can exchange the chains attached to them as shown in Fig. 2.1(c). The bond

exchange reaction can happen when the distance between any sulfur atoms from different chains comes within a cutoff distance of 4.12 Å (double of the S–S bond length[108], 2.06 Å) and when such sites are identified, the probability of the reaction is modeled as a function of temperature. For vitrimers, the temperature at which the acceleration of the reaction rate occurs is referred to as topology freezing temperature (T_v) and this value can be different or close to the glass transition temperature (T_g) of the vitrimer[80, 109]. In this paper, we assumed both the transitions occur at the same temperature ($T_v = T_g = 403$K). However, in the case of different transition temperatures, the vitrimer behavior can be modeled by considering T_v as the reference for dynamic bond exchange reaction probability. It is observed in experiments that the dynamic bond exchange reactions are very slow at room temperature but can accelerate near or above the topology transition (T_v) temperature of this vitrimer system [104, 105]. The modulus is seen to soften and the mobility of the chains accelerates around the transition temperature in a sigmoidal manner[110]. Based on this insight, we model the topology transition by accelerating the dynamic bond exchange reactions in a sigmoidal manner around the vitrimer transition temperature. Note that the actual experimental time scales of the exchange reactions are slower[111], and accelerated rates serve to realistically capture the thermomechanical behavior within the time scale of molecular dynamics simulations[100, 101]. To model the onset of the dynamic exchange reaction phenomenon in the current model, we assign the probability of the S–S bond exchange reaction as a function of the temperature as shown in Fig. 2.3.

The probability of the dynamic bond reaction as a function of temperature is given by Equation 2.1.

$$p(T) = \frac{1}{\left[exp\left(-a\left(T - T_v\right) - ln\left(\frac{p_{T_v}}{1-p_{T_v}}\right)\right) + 1\right]} \tag{2.1}$$

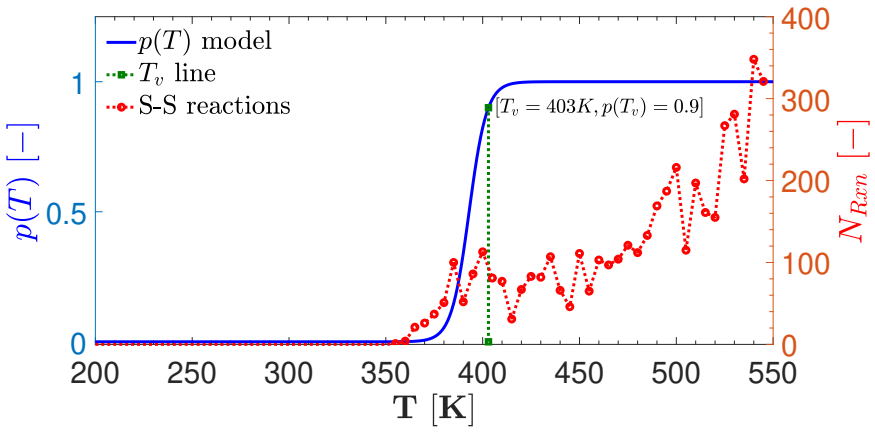

Figure 2.3: The reactions probability and the resulting number of S–S bond exchange reactions (N_{Rxn}) vs. temperature

where, $a = \frac{2p_{T_v}}{w(1-p_{T_v})}$ is determined by w which is the measure of the width of the transition from glassy to rubbery phase measured, for example, using the modulus vs temperature response (we consider, $w = 20$ K), and $p_{T_v} = 0.9$ is the probability of the dynamic bond exchange reaction at T_v (T_v line in Fig. 2.3), we assume that at T_v, most of the transition starts occurring but it is not complete hence $p_{T_v} = 0.9$. And, we assume that at the beginning of the transition window, $T_v - w$, the probability is $p(T_v - w) = 1.0 - p_{T_v} = 0.1$. This is considered in order to obtain a smooth increase in the reaction rate near T_v.

2.3 Results and Discussion

We first analyze the molecular dynamics model without dynamic S–S bond (indicated in plots as 'static' model) and with dynamic S–S bond exchange modeled. The annealed structure is equilibrated for 150 ps [112] at each temperature starting from 200 K to 550 K at an increment of 5 K. The change in volume is computed and normalized with respect to the initial volume at 200 K (V_0). The algorithm keeps a cumulative count of bond exchange reactions that occurred in the system[76]. In this system, the number of bonds remain conserved, and hence, bond breaking is accompanied with new S–S bond formation (as sketched in Fig.2.1(c)). The number

of S–S bond–exchange reactions occurring at each temperature is depicted as a red line in Fig. 2.3 alongside the chosen reaction probability (in blue). This plot indicates that the number of reactions begin to increase as we get close to T_v and stabilizes around T_v. At temperatures well beyond T_v (when the probability of reaction is 1.0), the number of reactions increase further with increase in temperature. This is attributed to an increase in the frequency of collision events of bonding atoms at higher temperatures. These features are achieved by developing a reaction probability centered around the topology freezing transition point based upon experimental insights[104, 105]. If the vitrimer transition temperature were lower than the glass transition temperature, then the reaction rates will be lower owing to higher stiffness of the polymer which will significantly decrease the collision frequency. As an example, we find that the number of exchange reactions over 150 ps was 53% lower for T_v set at 200 K vs 403 K for this polymer. By changing the T_v value, we expect the model to capture the topology transition behavior for other such vitrimers as well.

Fig. 2.4 shows the V-T characteristic of the neat vitrimer for static and dynamic S–S bond modeled in the simulation. The plot clearly shows that there is no change in the volume expansion for dynamic and static S–S bond until the reactions start picking up near $T_v - w = 403\text{K} - 20\text{K} = 383$ K when the probability of the reaction is $1 - p_{T_v} = 0.1$. We also observe that the dynamic S–S bond model has a higher coefficient of thermal expansion as compared to the static S–S model in the rubbery region beyond T_v. This is expected due to the added mechanical flexibility owing to dynamic rearrangements of chains[13]. The static coefficient of thermal expansion below T_v of $41.1 \pm 2.7 \mu K^{-1} (= \frac{\Delta V}{3V_o})$ falls at the lower end of the range reported ($45.0 - 65 \mu\ K^{-1}$) for cured epoxy resins [113]. The model is next employed in a first attempt in literature, to the best of the authors' knowledge, to understand the effect of dynamic bond exchange reaction on mechanical behavior at different temperatures.

In Fig. 2.5, stress–strain relationship as a result of stretching the simulation box

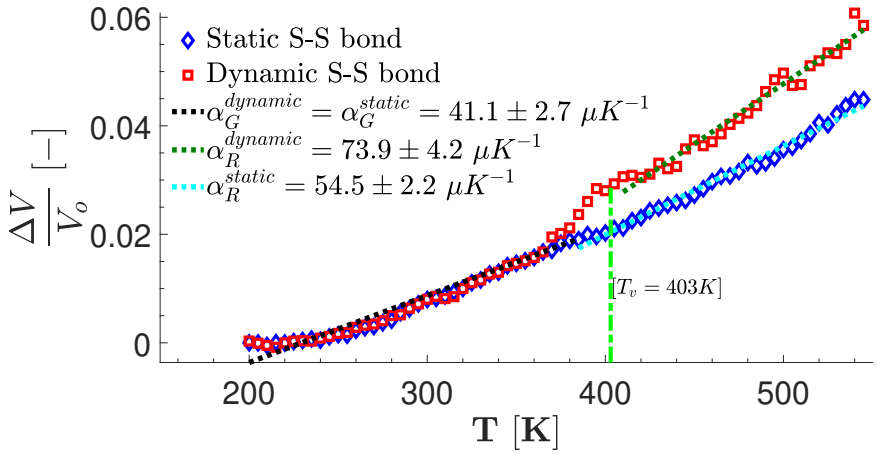

Figure 2.4: Volumetric expansion vs. T for model with and without modeling S–S bond reactions. R and G represent rubbery and glassy phases of the glass transition, respectively.

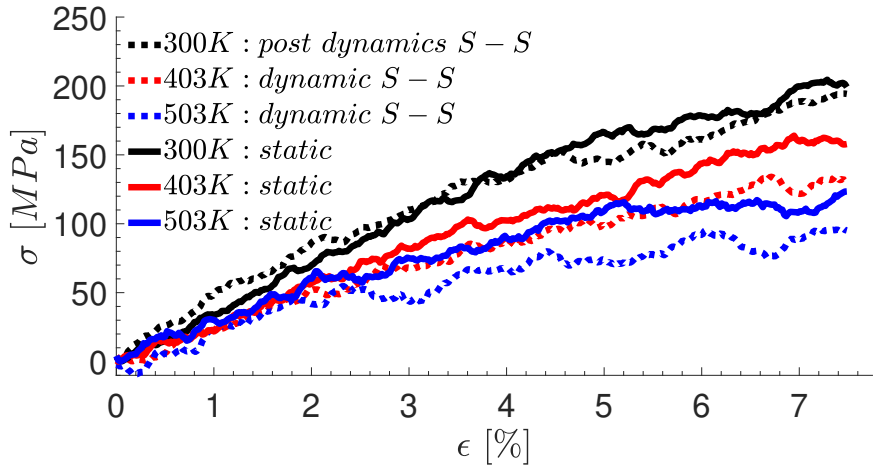

Figure 2.5: Influence of dynamic S–S bond modeling under uni-axial tension

along an axis at a strain rate of $2 \times 10^8 s^{-1}$ at different temperatures is shown. At higher temperatures, both models show softening behavior. However, the difference in the stress-strain behavior is pronounced at high temperatures ($T_v + 100$K) where dynamic bond exchange dominates and vitrimeric material remains softer. The dynamic bond exchange model is taken to 503 K for 250 ps and relaxed back to 300 K to compare the room temperature behavior after thermal cycling. In this case, the post dynamic bond and the static S–S bond cases follow each other well, which shows that despite the model having undergone dynamic bond exchange reactions upon heating,

the elastic response is retained at room temperature (300K). This is inline with the understanding of the response of the recycled vitrimers[80, 81]. Note that due to inherently high strain rates employed in molecular dynamics, the Young's modulus of DGEBA:AFD vitrimer remains overpredicted (4.5 ± 0.21 GPa) compared to experiment (2.6 GPa) under quasi-static loading[106] conditions at 300 K. MD simulations have predicted in the range of 3.4 GPa to 5.8 GPa for epoxies[114, 115, 116, 117] in literature. Note that while a vitrimer behaves like a viscous fluid beyond the topology transition temperature (T_v)[20, 19, 21], molecular dynamics results show sustained stresses beyond T_v due to the high loading rates (as is also seen in MD literature [100, 101]).

We now exploit the dynamic S–S bond exchange reaction capability to demonstrate healing of vitrimers in MD simulations. The damage corresponds to a carbon nanotube (CNT) pullout from the matrix[118, 119, 120]. We first insert a (12,12) single walled CNT of 91Å length along $z-$axis, and displace the atoms radially in xy plane. The rest of the curing protocol, described in the methods section, remains same as the neat vitrimer model with a final density of $\rho = 1.19$ gcm^{-3} at 1 K (refer Figure A.5 of Appendix A). To generate the damage, the CNT was removed out of the equilibrated simulation box. Then the simulation box is heated up to a temperature $T_v + 100$K$= 503$ K for 250ps. The hole heals under the influence of dynamic S–S bond exchange reactions. The healed system is then relaxed back to analyze its elastic response at room temperature. Fig. 2.6 shows the elastic response of the damaged and healed vitrimers (averaged of three different direction stretches with the bounds shown by light colors) at 300 K. We observe that the stress–strain response of the healed vitrimer is consistently higher than that of the initial damaged sample along all three loading directions demonstrating healing. In order to plot the elastic properties over a range of temperatures, we computed the stiffness by linear regression in $\epsilon = 4\%$ range and the elastic modulus was averaged in all three directions. Fig. 2.7

demonstrates that the healed structure is able to recover the pristine vitrimer elastic modulus over the range of the temperatures below topology freezing point. Snapshots of damage healing showing the hole left by CNT pullout being filled via a dynamic bond exchange mechanism post T_v are shown as inset (refer animation in SI).

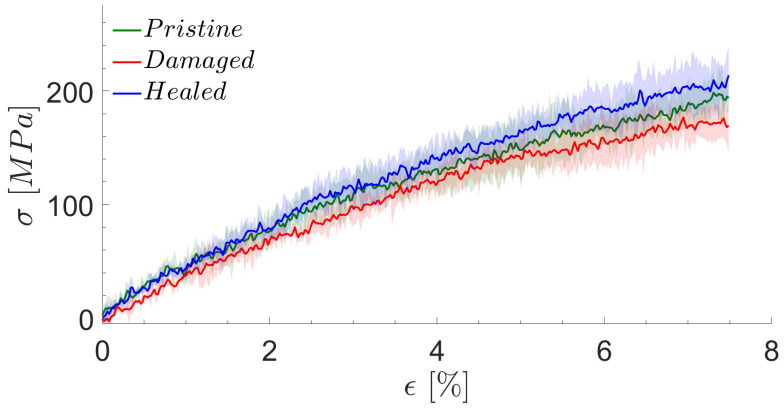

Figure 2.6: Stress-strain response under uniaxial tension in different directions at 300 K for damaged and healed samples.

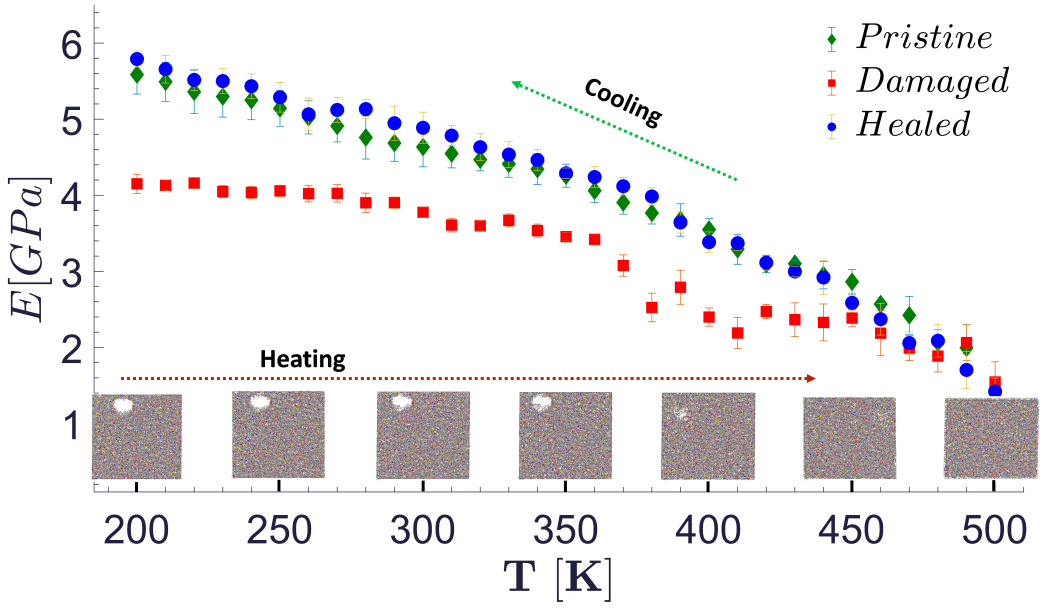

Figure 2.7: Stiffness enhancement post damage healing via S–S dynamic bond exchange reactions.

2.4 Conclusions

In conclusion, a vitrimer's ability to dynamically reform covalent bonds during thermal cycling allows one to achieve superior behavior over traditional thermosets such as damage healing. To model this behavior, we have developed a novel temperature dependent reaction probability which is integrated with molecular dynamics modeling of vitrimers. The reaction probability is empirically based on the observed reaction kinetics of dynamic bond exchange near or above topology freezing transition temperature (T_v). It is shown that the model captures the onset as well as the increase in number of reactions above this transition point owing to higher mobility of chains, without the need to alter reaction distance cutoffs. The vitrimer is seen to achieve softer behavior around and beyond topology freezing transition temperatures while maintaining the glassy behavior at pre-transition temperatures upon thermal cycling. In the simulation of the healing of a cylindrical pore created due to CNT pullout, the model is able to show both the healing of the vitrimer and complete recovery of elastic modulus upon cooling. Such modeling capability can be further used to achieve insights into the interplay of mechanics and chemistry in a variety of other dynamic bond exchange materials.

CHAPTER III

Understanding Creep Mechanisms in Vitrimers

Vitrimers offer a promising sustainable alternative to conventional epoxies due to their recyclability. Vitrimers are covalent adaptive networks where some bonds can break and reform above the vitrimer transition temperature. While this can lead to desirable behavior such as malleability, this also leads to undesirable rheological behavior such as low-temperature creep. In this work, we investigate the molecular mechanisms of the creep of vitrimers using molecular dynamics simulations. The interplay between dynamic bonding with mechanical loading is modeled using a topology-based reaction scheme. The creep behavior is compared against cross-linked epoxies with dynamic reactions to understand the unique aspects related to dynamic bonding. It is found that the free volume that arises from tensile loads is reduced in vitrimers through dynamic bond rearrangement. An important feature that explains the difference in secondary creep behavior between conventional epoxies and vitrimers is the orientation of the dynamic bonds during loading. In vitrimers, the dynamic bonds preferentially align orthogonal to the loading axis, decreasing the axial stiffness during secondary creep, resulting in larger creep strain compared to epoxies. Over longer timescales, such increased strain leads to void growth, resulting in tertiary creep. Thus, chemistry changes or additives that can prevent the initial realignment of dynamic bonds, and therefore subsequent void growth, can be an effective strategy to

mitigate creep in vitrimers.

3.1 Background

Epoxy is a thermoset polymer that is widely used in automobile, aerospace, robotics, and wind energy industries[121, 122]. Due to their thermal and chemical stability, they have played an important role in the emergence of advanced high-performance composites. However, the thermoset nature of epoxies has limited their life cycle due to the lack of damage mitigation or recycling capabilities[123, 124]. Another class of polymers, thermoplastics, are easy to recycle but are limited by their thermomechanical performance in critical structural applications[125, 126]. Vitrimers are a new class of polymers that offer the best of both thermosets and thermoplastics via dynamic cross-link reactions in the polymer network. They behave like a cross–linked thermoset at room temperatures and demonstrate malleable properties of a thermoplastic when heated beyond a temperature where dynamic bonds become active[11, 12, 127]. This ability of vitrimers makes them a promising candidate towards damage mitigation during operation and recyclability afterwards[128, 129].

A major challenge associated with the usage of vitrimers is associated with low-temperature creep[130, 131, 132]. Creep is the deformation of the material with time under the application of constant stress. Creep strain in polymers is simplified to Findley's power law, $\epsilon = \epsilon_0 + \epsilon^+ t^n$, where t is time and ϵ_0, ϵ^+ and n are constants for a given stress level[133]. Polymers, whose glass transition (glassy to rubbery transition) temperatures are relatively closer to room temperature, are prone to experiencing creep at room temperature. Often, creep can lead to an undesirable amount of deformations that compromise the integrity and function of a structure[134, 135, 136]. Therefore, it is important to understand the creep behavior and underlying mechanisms for improved molecular design of vitrimers.

Creep in polymers and fiber composites is a well-studied phenomenon both experimentally[134,

135, 136, 137] and computationally[138, 139, 140, 141]. Creep under uniaxial tension is found to follow three stages. In primary creep, the strain increases at a rapid rate during initial loading but continues to slow down over time. The second stage, termed secondary creep, is characterized as a region of uniform strain rate. Tertiary creep is the final stage of creep where the material strain accelerates and leads to a rupture. Molecular scale experiments by Lee et al. on crosslinked poly(methyl methacrylate) reinforce the notion that stress-induced chain mobility allows polymer glasses to flow during creep[142]. In addition, Bradley et al. found that the creep in vinylester resins reduces with the duration of resin curing due to higher cross-linking[137]. While adding reinforcing fibers was found to reduce creep, the exponent n was found to be largely unchanged.

Unlike conventional epoxies, understanding of the creep in vitrimers is rather limited. It is difficult to probe and investigate the underlying dynamic bonding mechanisms in vitrimers experimentally and this is where molecular simulations provide an exciting alternative to further such understandings[101, 143]. A recent experimental study by Hubbard et al. sheds light on the possible molecular mechanisms in the stages of vitrimer creep, where it is postulated that secondary creep in vitrimers is associated with network rearrangement due to dynamic reactions[144]. It was also noted that at low temperatures and catalyst concentrations, vitrimers simply behave as a traditional epoxy material. Dynamic cross-linking reactions tend to accelerate beyond the topology freezing temperature (T_V), however, a small extent of these reactions at lower temperatures can influence creep behavior[132, 145].

In this work, we employ all–atom molecular dynamics (MD) simulations to study the creep behavior in vitrimers, which is carried out for the first time to the best of the authors' knowledge. The MD framework has been widely utilized to predict the properties of metals[146, 147] and polymers including mechanical[91], thermal expansion[86], thermal conductivity[88, 87], heat capacity[87], and glass transition[91, 148] proper-

ties. In particular, MD simulations have also been utilized to model the creep behavior of metals[146, 149, 150, 151] as well as polymers[138, 140, 152, 153]. Several of these molecular models, specifically polymers, simplify atomic interactions using coarse-grained/bead-spring models to model chain dynamics. While such models capture conformational changes, they poorly describe chain-to-chain interactions that determine the free volume evolution. A recent all-atom MD study of creep shows that secondary creep is mechanistically related to void nucleation, while tertiary creep is related to void growth and coalescence[154]. Furthermore, MD simulations by Li et al. describe creep in epoxies in the context of the free-volume change theory of Fox and Flory. With increasing stress and temperature, the creep correlated with increases in the free volume in the simulation cell[155]. It is to be noted that the time scale of creep at the macro scale is in the range of hours or even days. However, for the purpose of understanding the underlying deformation mechanism of creep, MD simulations of creep need to be performed using elevated stress and/or temperature, and at high strain rates.

The primary challenge for the MD approach is the modeling of the temperature-dependent reversible cross–link reactions. Exchange reactions have been modeled in the past via methods such as embedding Monte Carlo (MC) moves into molecular dynamics, fully MD (using specialized reactive potentials), or fully MC simulations to simulate bond swaps[95, 96, 97, 98, 99]. These simulations have typically employed coarse-grained (bead–spring) models that provide high computational efficiency while approximating the mechanical response. For more quantitative modeling, all–atom MD methods are attractive[101, 100]. Previously, bond exchange reactions in all–atom MD have been implemented using distance–based reaction schemes based on pre and post–reaction templates[148, 76]. The approach accelerates the slow reaction dynamics and allows the modeling of mechanical property changes in vitrimers during thermal cycling.

Typically, creep in epoxies is simulated by applying stress and letting the system evolve over time under NPT dynamics[155]. However, in a vitrimer system with dynamic bond exchange reactions, NPT dynamics can become unstable due to energy fluctuations caused by local topology modification whenever dynamic cross-linking reactions occur. In this work, we devise a new strategy to simulate the creep behavior of vitrimer with dynamic reactions by alternating loading and equilibration steps. In parallel to the experimental work by Hubbard et al., the approach is used to differentiate creep response in vitrimers and traditional epoxies to identify mechanisms fundamentally derived from their dynamic bond exchange reactions[11, 12, 144, 156].

3.2 Methods

We employ classical MD simulations to simulate the creep behavior of vitrimer system, composed of diglycidyl ether of bisphenol-A (DGEBA) cross-linked with 4-aminophenyl disulfide (AFD), the chemical structures shown in Figure 1(a). Large-scale atomic/molecular massively parallel simulator (LAMMPS)[157, 158] is used to carry out all of the simulations in this study. consistent valence force field (CVFF) is assigned to all the atoms with energy contributions from the pair, bond, angle, dihedral, and improper interaction terms[57]. Additionally, the energy contributions from the non-bonded interactions are modeled using Lennard-Jones (LJ) and Coulombic pairwise interaction with a cutoff of 12 Å. A time step of 1 fs is used for all of the MD simulations in this work.

3.2.1 Polymer system preparation

The polymer system for MD simulations is prepared using polymerization reactions (primary and secondary amine reactions) for curing the monomer mixture. In this approach, the *fix bond/react* feature in LAMMPS is utilized that enables the modeling of reactions by changing the local topology[76, 77]. First, a mixture of monomers with

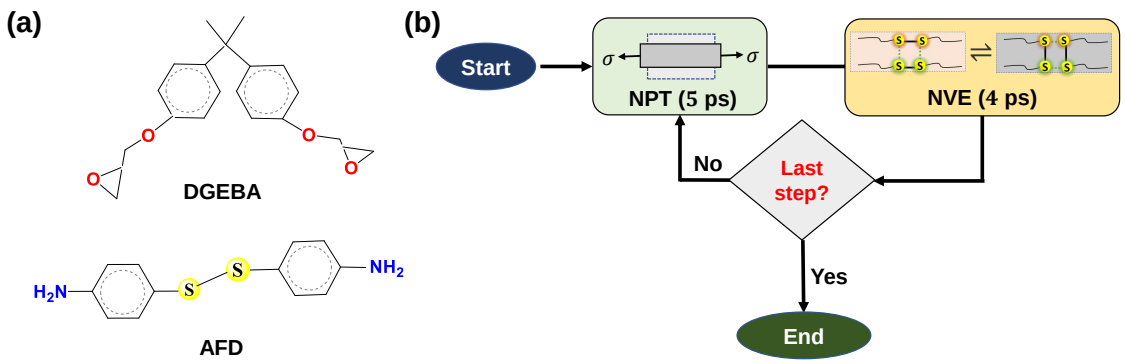

Figure 3.1: (a) Monomer structures, and (b) Methodology for simulating creep with dynamic S−S reactions

two DGEBA units and one AFD unit is constructed. The typical synthetic epoxy to hardener stoichiometric ratio of 2:1 is employed[124, 159]. The repeating unit that contains the monomer mixture is shown in Figure 3.2. It is to be noted that we have created DGEBA structure with epoxied ring open to having a simpler one-step reaction for curing. The epoxy bond in the DGEBA unit is considered to be open as it will reduce the steps in the curing amine reactions. We repeat this unit by $8 \times 8 \times 8$ to get a simulation box with 1,024 DGEBA and 512 AFD monomer units, with a total of 68,608 atoms. Periodic boundary conditions are applied in all three directions. Then, the constructed monomer mixture is equilibrated using the NVT ensemble (constant number of particles, volume, and temperature). Subsequently, the mixture is equilibrated to a density of 1.0 gcm^{-3} using an NPT ensemble (constant pressure and temperature). Nose-Hoover thermostat and barostat are used to maintain the temperature and pressure in the simulation box, respectively.

The pre– and post–reaction templates are prepared for both primary and secondary amine reactions and can be found in our previous work[148] and in Chapter II. The cutoffs between N and C atoms are set to 3.5 Å and 5.0 Å for initiating the primary and secondary amine reactions, respectively. The mixture is then allowed to have primary and secondary amine reactions under the NVT ensemble. After the system is cured to 95%, it results in a system with internal stresses in the box. Therefore,

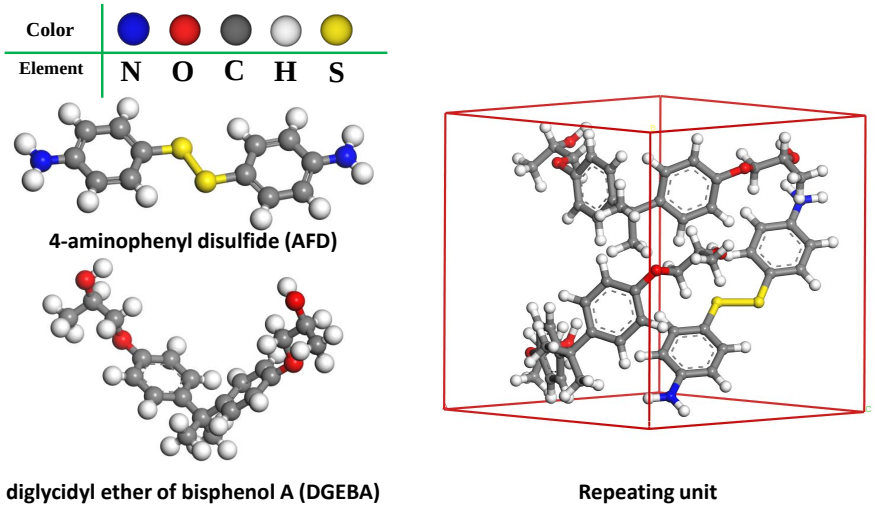

Figure 3.2: Monomer structures (left) and a periodic repeat unit box that contains DGEBA:AFD in 2:1 ratio (right)

to relieve these stresses, the system is annealed by undertaking the box to cooling and heating cycles of 1 K and 600 K, respectively with a simulation time of 50 ps at each of these temperatures under NPT (pressure of 1 bar), as also reported previously[148]. This process releases the stresses built in the box and brings the system to an equilibrated density of $\rho = 1.184$ gcm^{-3} at 1 K, and the converged density at 300 K of $\rho = 1.159$ gcm^{-3} which is in agreement with values for a typical epoxy system from literature[160]. The resulting MD simulation box is shown in Figure3.4(a), where the inset shows a section of the chain segment highlighting the presence of singly and doubly reacted Nitrogen atoms as a result of curing. The inset also shows a potential site for a disulfide bond exchange reaction where two S−S bond chain segments come in close vicinity to result in an exchange of chains as illustrated in Figure3.4(b). These are the characteristic reactions of this vitrimer system which accelerate above its topology transition temperature and result in the rearrangement of the network. The disulfide reactions are modeled using the topology-based update, and the pre- and post-reaction templates for these vitrimer reactions are shown in

Figure S.2 of the supplementary information. The reaction occurs when any two sulfur atoms from two disulfide pairs come within a cutoff of 4.12 Å. Then the reaction can proceed with an assigned probability, where, the probability of 0.0 implies no S–S reactions while 1.0 means all such eligible disulfide pairs can have a bond exchange reaction.

3.2.2 Simulating creep

Computational experiments of creep are simulated under constant stress applied in the loading axis while other transverse directions are kept stress-free[161, 162, 151]. In this work, this is achieved using Nose-Hoover anisotropic barostat and thermostat under NPT conditions on the box. An anisotropic barostat allows individual stress components to be prescribed on the box. For simulating uniaxial creep, the prescribed state of true stress is: $\sigma_{yy} = \sigma_o,\ \sigma_{xx} = \sigma_{zz} = 0$ where the constant true stress σ_o is maintained in $y-$axis. All three shear stress components are left unspecified which implies the shear strains on the box are kept to zero, therefore, the box stays orthogonal during the creep simulations.

For an epoxy system, creep could be simulated by applying a constant value of stress and letting the system evolve over time under NPT dynamics. However, in a vitrimer system with dynamic bond exchange reactions, NPT dynamics can become unstable under applied pressure due to local fluctuations in temperature and pressure tensor caused by local molecular topology changes during reaction events[76, 77]. Furthermore, under stress-controlled loading (such as in creep), the box can change the dimensions suddenly and the dynamic cross-linking reactions can result in the loss of bonds or atom images across box boundaries which can lead to simulations failure. In the case of strain-controlled loading, given it is small, the dynamic bond reactions can take place while deforming the box slowly as reported in our previous work[148]. In the present study, to simulate the creep behavior of vitrimers, which is

a stress-controlled loading, we have devised a new strategy as shown in Figure 3.1(b). Here, we break the application of stress into two parts, first, an NPT is run for 5 ps followed by an NVE for 4 ps under which the dynamic S−S reactions happen. The S–S reactions are allowed to happen only once in this reaction step, and which is controlled by specifying the reaction frequency in *fix bond/react* card in LAMMPS. The NVE step allows the system to have reactions when there is no deformation happening (constant volume) and adequate time to relax the system after the reactions occur. The NPT step is then invoked where the system deforms under creep, and these steps are repeated. For comparison with the case of epoxy, the effect of the additional NVE step on creep response is discussed in Figure 3.3. The dynamic

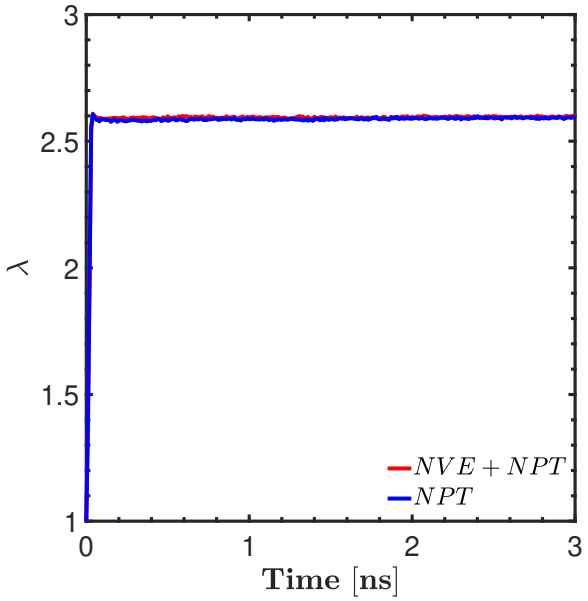

Figure 3.3: Comparison of running NPT only and NPT+NVE for the case of vitrimer without reaction

bond exchange reaction (DBER) of this vitrimer system involves the rearrangement of the chains due to the disulfide bond which is simulated by topology change-based reactions[76, 77]. The pre- and post-reaction templates for this DBER are shown in Figure 2.2. The reaction is initiated based on the cutoff distance between the initiator atoms (either one of the green or yellow sulfur atoms).

To simulate, it is required to prescribe a stress-controlled loading, and as result, there can be sudden large dimension changes in the simulation box. The presence of dynamic bond exchange reaction (local topology change) along with the sudden large change in the box dimensions lead to missing image flags of bonds and atoms across the periodic boundary. Therefore, we use a step-wise alternating loading with NPT (constant number of particles, pressure tensor, and temperature) and reactions under NVE (constant number of particles, volume, and energy) conditions. Figure 3.3 shows the effect of the addition of the NVE step along with NPT for an 'epoxy' (vitrimer system with no reactions). This shows that the addition of an NVE step does not introduce any alteration to the chain mobility.

To accelerate the creep phenomenon in MD simulations, we apply a high value of uniaxial stress at high temperatures. The value of the applied stress dictates the resulting creep response of vitrimers, the role of which is also discussed in the later sections. The resulting response is characterized by the stretch ratio (λ) in the loading direction, which is defined as:

$$\lambda = \frac{l}{l_o} \tag{3.1}$$

where, l is the current length and l_o is the initial or undeformed length of the simulation box along the loading direction. In this work, the following studies are conducted: (a) the comparison of the creep response of a vitrimer and an epoxy; (b) the influence of applied stress or loading on vitrimer creep; and (c) the effect of S–S reaction probability on the creep response of vitrimers.

3.2.3 Free volume of voids

The free volume or the void volume is the region of space where atoms are not present and it is computed using an *alpha-shape* method[163] implemented in OVITO software[164]. All the simulations are visualized using OVITO by performing surface mesh construction analysis. The probing sphere has a finite radius and for the analysis

in the present study, we have considered it to be 3.5 Å and the details of which can be found from OVITO documentation[164]. This approach helps us identify the actual material volume as well as the void volume for any time instance during the simulation of creep. The volume fraction of the void is computed using a Python script for OVITO. The percent volume fraction of the void (V_f^{void}) is defined as:

$$V_f^{void} = \frac{V_{void}}{V_{cell}} \times 100 \tag{3.2}$$

where, V_{void} and V_{cell} are the volume of the empty region and the total volume of the MD simulation cell at a given time instance, respectively.

3.2.4 Bond orientation

The vitrimer undergoes large deformation under creep in these simulations, therefore, it is important to probe the molecular mechanisms contributing to different aspects of the creep deformation and system evolution. MD simulations offer the capabilities to look into various quantities during the system evolution. One such quantity of interest is the orientation of the disulfide bonds when they undergo dynamic cross-linking reactions during deformation. Bond orientations of the S−S bonds are computed for the entire simulation box and used to analyze the results of the vitrimer with both, dynamic reactions and with reactions turned off as a baseline. The bond vector is computed using the coordinates of the two sulfur atoms:

$$\boldsymbol{v}^{\text{S-S}} = \boldsymbol{x}_1 - \boldsymbol{x}_2 \tag{3.3}$$

Since the simulation box is periodic in all dimensions, the coordinates of the two sulfur atoms are corrected based on the image flag of the atom. The bond vector projection

of an S−S bond pair on the loading axis ($y - axis$ in this case) is computed as:

$$v_y^{\text{S-S}} = \left| \boldsymbol{v}^{\text{S-S}} \cdot \boldsymbol{y} \right| \tag{3.4}$$

The average value of the bond vector projection on the loading axis is evaluated as:

$$\overline{v}_y^{\text{S-S}} = \frac{1}{N} \sum_{i=1}^{N} \left| \boldsymbol{v}_i^{\text{S-S}} \cdot \boldsymbol{y} \right| \tag{3.5}$$

where, $< \cdot >$ denotes the dot product of two vectors, $\boldsymbol{y} = [0\ 1\ 0]^T$ is the loading axis vector and N is the total number of S−S bonds in the simulation box. This computation is implemented in OVITO using the python scripting interface. First, all the S−S (disulfide) bonds are selected and then their connecting atoms are identified. The coordinates of the connecting sulfur atoms are used to evaluate the S−S bond orientation vector.

3.3 Results and Discussion

Creep is an inherently slow phenomenon, beyond the time–scales of MD simulations when simulated at ambient conditions. Simulations of creep using atomistic simulations make an inherent assumption that the mechanisms that drive creep under ambient conditions also exist at extreme conditions at which accelerated creep occurs. Accelerated creep occurs at extreme conditions such as at high tensile loads close to or exceeding the yield stress and at higher temperatures where vitrimer reactions occur rapidly. In order to test all regimes of vitrimer creep, we employ extreme conditions in our simulations such that creep can occur rapidly and the mechanisms can be systematically analyzed. Another important assumption is that bond rupture of crosslinked epoxy bonds is not simulated. While such bond rupture occurs at high strains during extreme loading, it is necessary to suppress such mechanism of failure

to study the actual mechanisms that might occur in ambient conditions where creep processes are much slower. In later subsections, we systematically reduce the extremity of loading to study the trends in the creep behavior as we move toward ambient conditions.

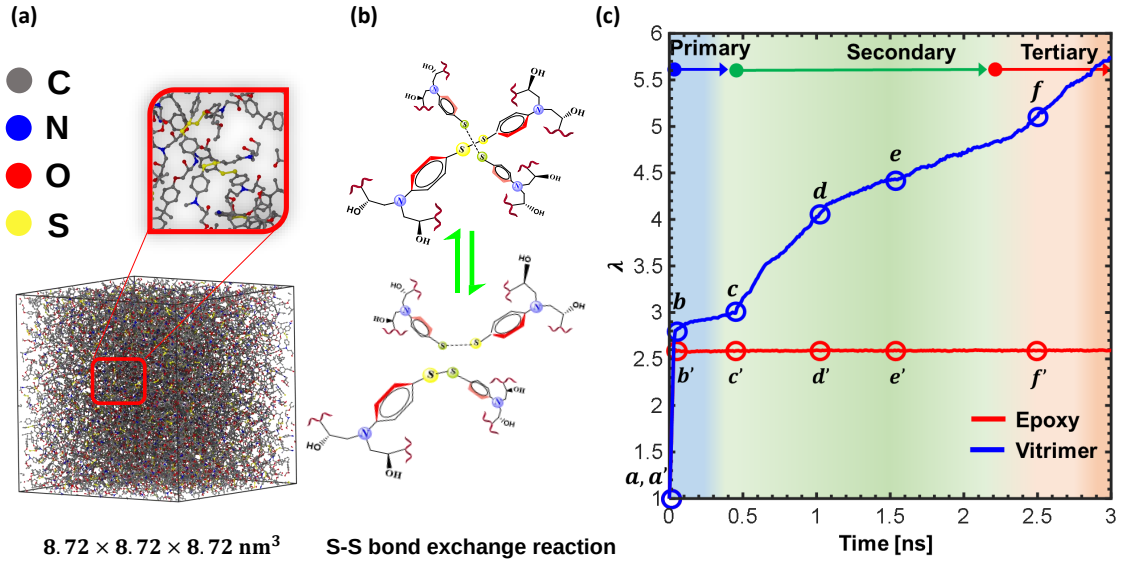

Figure 3.4: (a) Cured and annealed periodic polymer system shown with H atoms hidden, (b) schematic of a disulfide bond exchange reaction in the vitrimer system, and (c) comparison of stretch ratio (λ) response vs. time for vitrimer and epoxy under constant uniaxial stress of 500 MPa at 600 K, the points from $a(a')$ to $f(f')$ refer to key chosen snapshots during creep deformation as discussed in the text. Three creep regimes of a vitrimer are marked with different colors.

3.3.1 Creep in vitrimer vs. epoxy

Figure 3.4(c) shows the time-dependent deformation response of the vitrimer with and without the dynamic bond exchange reactions under uniaxial stress of 500 MPa at 600 K. This is an extreme case where the temperatures are well above the topological transition temperature, hence, we specify the probability of the S−S bond reactions to be $p = 1.0$. When the dynamic reactions are switched off, the material behaves like a conventional epoxy. Henceforth, the case with no reactions is thus referred to as the 'epoxy' and the case with reactions is referred to as the 'vitrimer'. With the

application of tensile stress, both vitrimer and epoxy show an immediate increase in the strain, referred to as the primary creep response. The vitrimer is slightly more compliant than epoxy in this regime. The interesting difference arises after the primary creep wherein the epoxy does not show a significant increase in the creep strain. However, the vitrimer shows a marked increase in the strain after the primary regime. We refer to this regime as the secondary creep, which occurs in vitrimers due to dynamic reactions. A third regime called 'tertiary creep' indicated as 'f' in Figure 3.4(c) is also observed at which void growth is observed to occur (shown and discussed in detail later in the manuscript). These three regimes of creep are shown using different colors which a gradual transition between them.

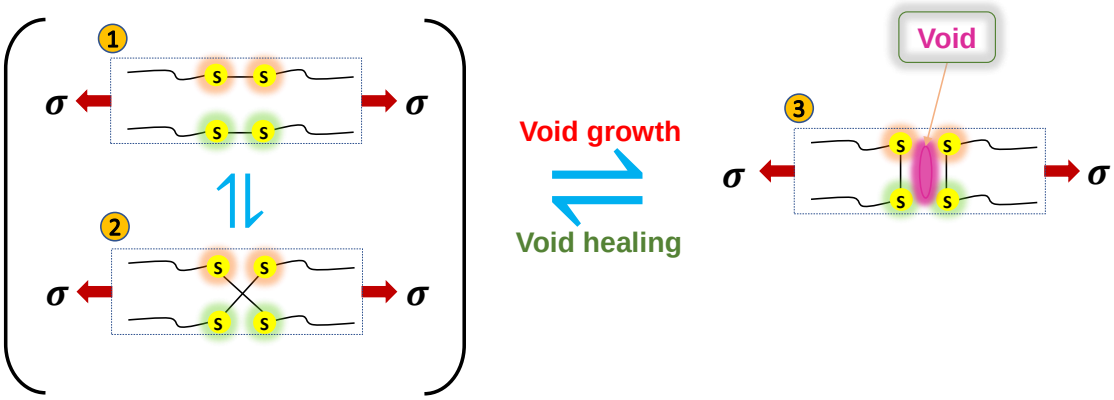

Figure 3.5: Possibilities of reaction pathways of the idealized chains opening due to S−S reactions under creep in vitrimers: ①-parallel, ②-crossed, and ③-perpendicular to the loading axis

For now, we focus on the mechanistic aspects of the secondary creep effect due to dynamic reactions in a vitrimer. Here, the types of chain arrangements are idealized into three configurations based on the orientation of the S−S bonds pairs in the vicinity ($\leq$ 4.12 Å) of each other, where the exchange between these configurations could lead to different outcomes on the bulk behavior of the vitrimer. To simplify the chain arrangements, we assume that the S−S bonds in the two chains are aligned in parallel, perpendicular, or in a crossed formation with respect to the loading axis.

Figure 3.5 shows the possible chain rearrangements due to S−S reactions between these three configurations. The dynamic exchange between configurations ① and ② leads to neither void healing nor growth since the axial loading can be accommodated by the chains in both of these configurations.

On the other hand, in case of a bond exchange from configuration ① to ③ or ② to ③, the chains can no longer bear the axial loads and this exchange will lead to a growth in the voids in ③. In the bulk, such reactions will lead to a reduction in the load-bearing ability and a stretch along the loading axis. The reverse of this exchange will heal the gap between the two S−S chains. This configuration switch (from ③ to ① or ②), however, can become increasingly less likely as void growth progresses under the application of stress. Based on the alignment of two S−S bonds with respect to the loading axis, configuration ③ will result in the incremental stretching of the box, which is the responsible factor towards high secondary creep in vitrimers. To evaluate the possibilities of these transformations quantitatively, we look into the values of the S−S bond orientation with respect to the loading axis and their evolution over time during creep. Note that the bonds are aligned normal to the loading axis in the void growth configurations ③ while in all other configurations, there is a significant component of the bond vector oriented along the loading. The average value of the bond vector projected onto the loading axis is used to quantify the differences in these configurations. A high value indicates that most of the chains are aligned to the loading axis and a relatively lower value indicates the prevalence of type ③ configuration which leads to a decrease in stiffness along the loading axis and hence, an increase in creep strain. Figure 3.6(a) shows the time variation of the mean value of the S−S bond projection on the loading axis ($\overline{v}_y^{\text{S-S}}$, from Eqn. 3.5). In the case of epoxy where these reactions do not occur and any realignment is due only to the chain mobility. This differentiates the projected bond length magnitude from that due to chain mobility versus those occurring due to dynamic reactions.

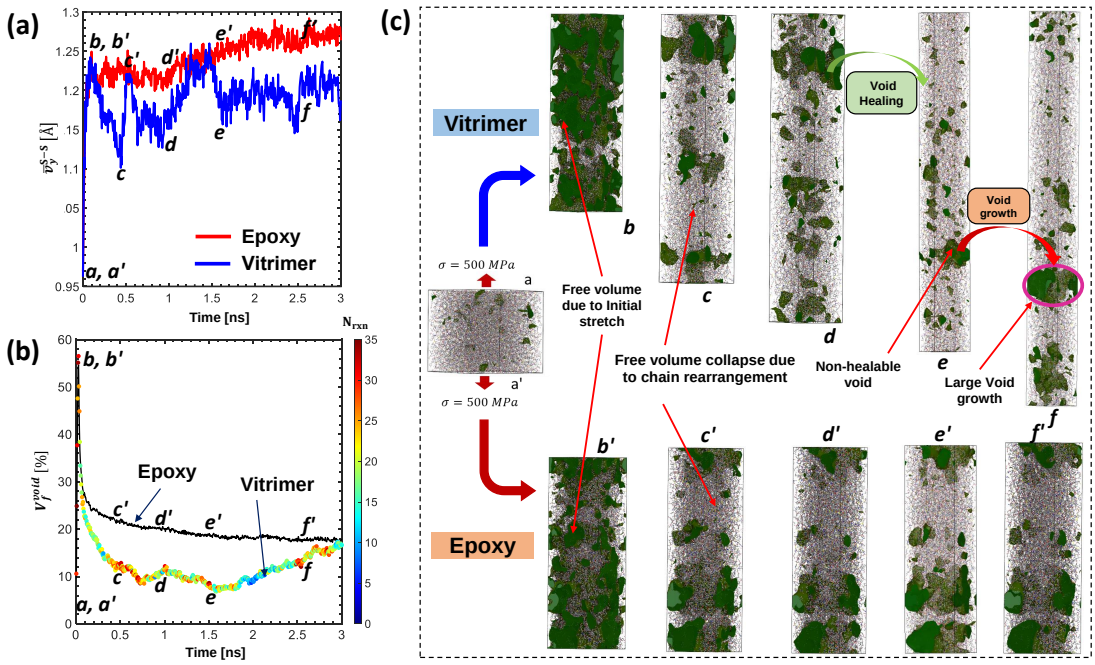

Figure 3.6: Comparison of creep in vitrimer and epoxy: (a) mean value of bond vector projection on loading axis (b) evolution of free volume fraction and number of S−S reactions in vitrimer, and (c) snapshots of the simulations box with free volume (green region) at different time instances of creep

In Figure 3.6(a), the mean bond orientations for vitrimers with and without dynamic bond reactions increase together in the initial phases of the primary creep regime (upto time $b(b')$). The vitrimer follows the epoxy initially because the total number of dynamic reactions occurring during the initial window is limited due to the small time window and rapid stretch due to high applied stress. The time period from $b(b')$ to $c(c')$ shows a clear difference between epoxies and vitrimers, at which point the effect of dynamic bonds show up. In epoxies, this region has a relatively stable state of the mean bond orientation with time concomitant with a decrease in free volume occurring due to chain mobility and accommodation. However, in the case of vitrimers, the mean bond projection decreases as the dynamic bond reactions result in the S−S bonds aligning towards a plane transverse to the loading axis. Figure 3.6(b) shows the void fraction (in percentage) as a function of time for both epoxy and the vitrimer cases. Initially, both epoxy and vitrimer show a rapid rise in void

fraction (a(a') to b(b')) which is attributed to the observation that the simulation box is not able to instantaneously relax lateral dimensions (perpendicular to loading direction) in response to high applied stress. In the region b(b')) to c(c'), the vitrimer case shows a steeper drop in the void fraction and lower void fraction indicating void healing due to dynamic bonding.

In vitrimers, the realignment of bonds reaches its peak at time c (Figure 3.6(b)). The time period between c and e is categorized as the secondary creep stage in the vitrimer. In epoxy, the void distribution achieves a stable state around time c' and slow changes in free volume beyond c' (Figure 3.6(c) - bottom) are driven by limited chain mobility. In vitrimers, this regime is related to the formation of smaller voids throughout the volume as shown in Figure 3.6(c) at times d' and e'.

The mean orientation increases in this regime as compared to time c indicating that the chains are preferring to align along the loading axis, while the void fraction remains somewhat constant (similar to the epoxy). In spite of this, large increases in strain are seen in the secondary creep stage in vitrimers. This can be explained using two processes that are acting in concert. First, there is elongation due to chain rearrangement (similar to epoxy), and second, there is a sudden burst in dynamic bond reactions driving the realignment of S−S bonds orthogonal to the loading direction (as seen in the rise and drop in projected bond length between c to d in Figure 3.6(a)), which is decreasing the stiffness along the loading axis. This, in turn, further increases the creep strain. In Figure 3.6(b), the points for vitrimers are colored according to the computed number of reactions occurring at each time step. The reactions are seen to accelerate in the secondary creep regime from c to d, which led to a significant increase in the creep strain as seen in Figure 3.4(c).

The stability of void fraction from c to e in vitrimers follows from the fact that the voids created during loading are balanced by the healing of voids via dynamic bonding and subsequent chain rearrangement in new configurations. The effect of dynamic

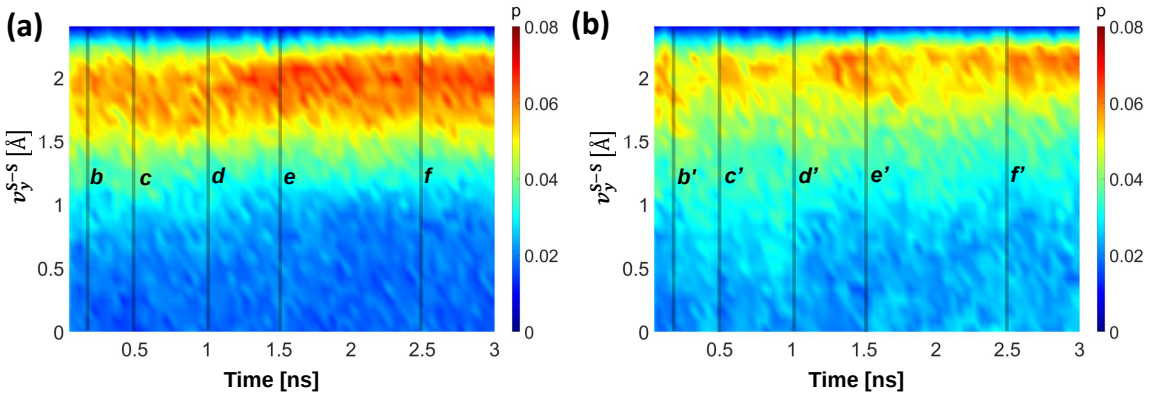

Figure 3.7: Probability distribution function of S−S bond vector projection on loading axis (v_y^{S-S}) at each time step for (a) epoxy and (b) vitrimer. The vertical lines mark the key time stamps pertaining to the creep response discussed in the text

bonding can be more clearly seen from a probability distribution function of the bond projection at each time step. While the plot in Figure 3.6(a) only contained the mean at each time step, Figures 3.7(a) and (b) show time-varying probability density of the bond projection (v_y^{S-S}) for epoxy and vitrimer, respectively, showing the complete distribution at each time step. We can see that for epoxy, more number of bonds are clustered towards a bond value of 2.0 Å and hence showing a higher mean value with a smaller standard deviation over the c'-e' regime. On the other hand, for vitrimer (Figure 3.7(b)), the probability is less than epoxy near (v_y^{S-S} = 2.0 Å) which is the equilibrium bond length of the S−S bonds. It also shows a larger spread in the probability throughout the duration of creep. Therefore, the bond exchange reactions lead to more transversely oriented S−S bond chains and can result in a configuration ② and ③. The former will contribute towards healing of the voids whenever they appear and the latter will result in a global strain increment as well as void growth. In vitrimers, the region between e and f is characterized by an increase in the volume fraction of voids. Such behavior is typically associated with tertiary creep. The increase in void-fraction in the vitrimer is related to one large void shown in Figure 3.6(c) that begins to grow and cannot be healed anymore. The number of dynamic bond exchange reactions also declines in this regime and the dynamic bond alignment

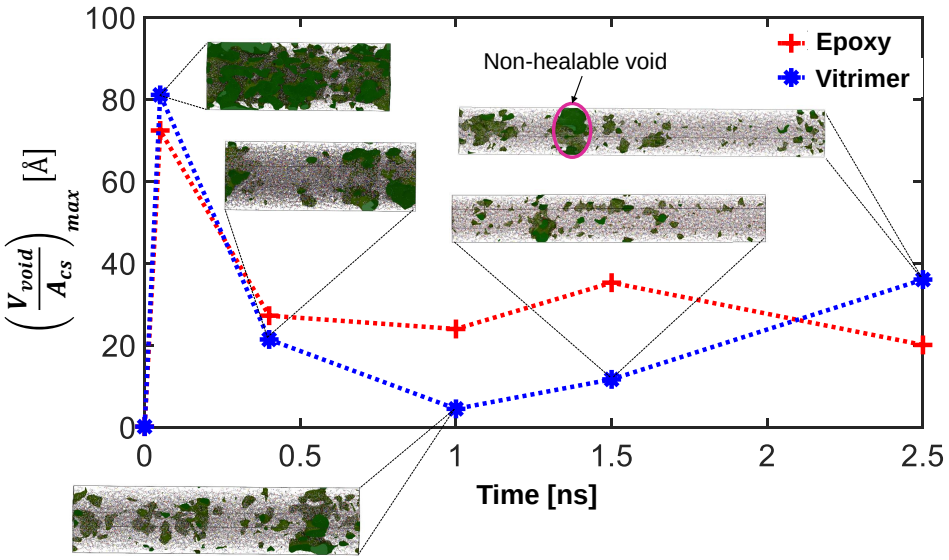

Figure 3.8: Largest void volume (normalized with the cross-sectional area) at various time stamps during creep of a vitrimer and epoxy. The plotted points correspond to time instances from a to f.

becomes stable. However, the large void grows resulting in an increase in the creep strain. Figure 3.8 plots the volume of the largest void in the unit cell normalized to the cross-sectional area. The y–axis corresponds to the effective height of the void if the largest void were to span the entire cross-section. An increase in the largest void (non-healable) is seen from e to f in the case of the vitrimer which is shown in the inset and is indicative of tertiary creep in the vitrimer system.

The values of stress and reaction probability dictate the extent and the rate of creep in materials. In the previous section, the accelerated creep was studied under extreme conditions. In the following section, we will look into the phenomena under smaller stresses and dynamic bond reaction rates to understand how the creep rates scale in typical laboratory conditions.

3.3.2 Influence of loading

Figure 3.9(a) shows the creep stretch response over time under the application of different values of applied uniaxial tensile stress. It is evident that primary creep strain increases with the magnitude of applied stress. The void fraction shown in Figure 3.9(b) remains stable for the lower stress cases over time due to healing processes. This indicates that the increase in creep strain during secondary creep is primarily a result of dynamic bonding driving the realignment of bonds orthogonal to the loading direction leading to decreased axial stiffness. The void fraction in the extreme case of 500 MPa is higher initially due to the higher chain mobility, however, healing processes eventually lower the volume fraction of voids to around 10% beyond which tertiary creep processes take over that increases the void volume fraction again. Tertiary creep behavior is not seen at lower stress levels due to lower chain mobility slowing down the progression of creep as well as a greater probability of healing as evident by the larger number of dynamics reactions at lower applied stress as shown in Figure 3.9(c).

At higher stresses, the creep strains are higher which increases the total volume of the system and thereby reduces the total number of dynamic S−S bonds available to interact per unit volume. This reduction in the number of reactions is seen over time in all the systems as the creep strain increases and is shown in Figure 3.9(d). The changes in the number of chemical reactions as a function of time shown in this figure also depict intermittent increases in dynamic reactions accompanying an increase in creep strain. This is followed by intermittent drops in the number of reactions that stabilize the creep strain but at the same time increase the void volume fraction. The creep strain occurs in step-like manner for higher loads due to increases in the types of bond-exchange reactions that lead to void growth and stretch (transformations to configuration ③) followed by void healing processes (transformations to configuration ②). While we observe these step-like increments in creep strain due to the nanoscopic

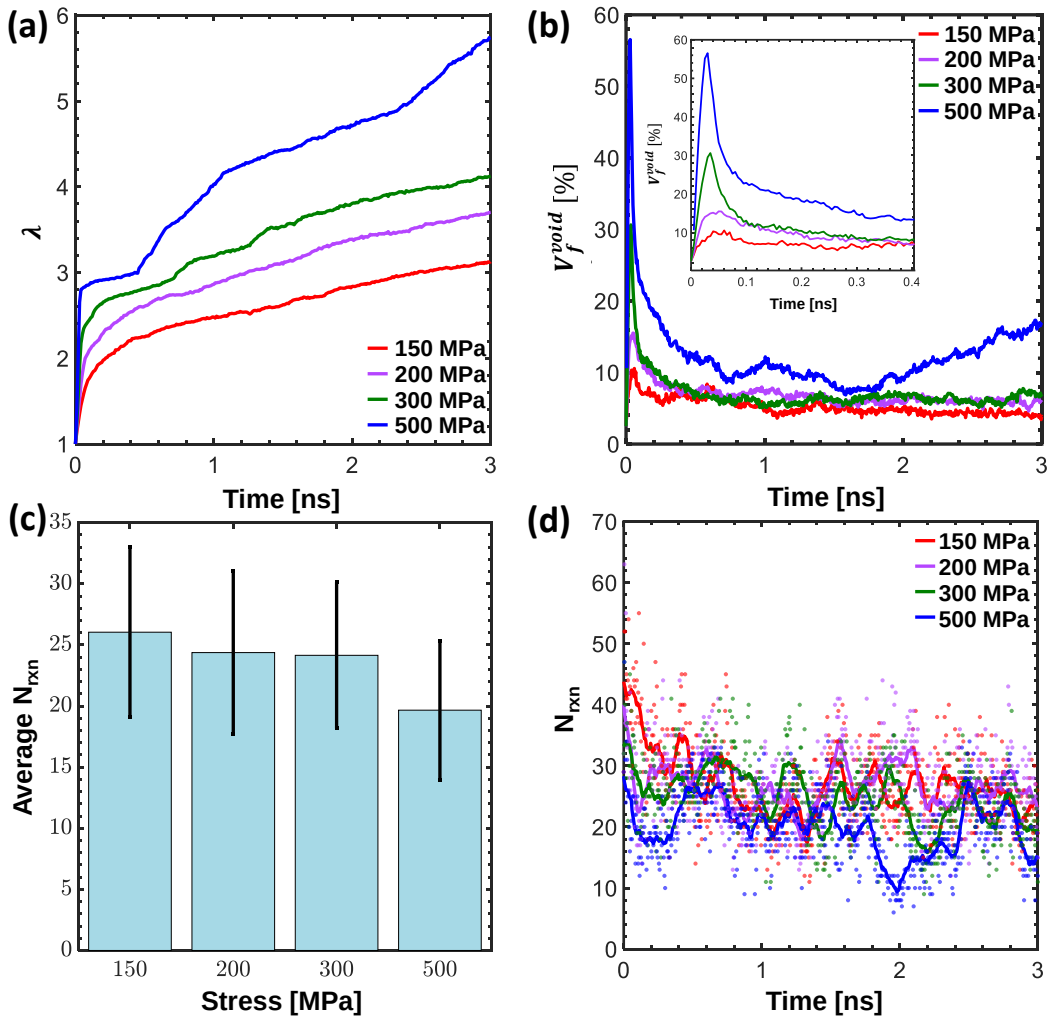

Figure 3.9: Vitrimer creep under various levels of applied stress (a) stretch ratio (λ) vs. time and (b) void volume fraction (c) the average number of reactions per loading step, and (d) number of reactions (N_{rxn}) at each time step shown in with data points and a moving average shown with line plot

nature of MD simulations (limited number of atoms), a more continuous response is expected to be observed at the macroscopic level, where multiple such step-like increments may be happening at random locations at different times resulting in continuous macroscopic strain response. For a lower stress value, the stress is not enough to cause such drastic 'sudden' increases in creep strain as the chains are unable to rapidly overcome inter-chain interactions (due to lower mobility).

3.3.3 Influence of reaction probability

Interestingly, the evolution of strain in secondary creep in Figure 3.9(a) shows that the strain rate remains stable with an increase in applied stress from 150 to 300 MPa. In all these cases, the reaction probability is taken as one, indicating the complete conversion of dynamic bonds when the S-S atoms interact during the simulation. The strain rate is constant for these stress levels indicating that the dynamic bond reaction rates are the controlling factor for differences in the strain rate in secondary creep. A recent experimental study by Hubbard et al. noted that at low temperatures and at low catalyst concentrations, vitrimers simply behave as a traditional epoxy material and the secondary creep rates increase with the amount of catalyst[144]. This effect of the extent of reactions can be simulated by controlling the probability of the disulfide reactions in our model. Figure 3.10 shows the influence of the probability of the dynamic cross-linking reactions for the vitrimer on the creep behavior at an applied stress of 500 MPa. A small increase in primary creep with an increase in the reaction probability is observed. The primary creep strain is relatively unaffected by the reaction probability as the initial strain happens rapidly enough such that the number of dynamic reactions during this stage is low.

However, the reaction probability (as a proxy for the amount of catalyst and temperature) has a strong effect on the strain rate during secondary creep as observed in experiments[144]. At a very low value of reaction probability (1%), secondary creep behavior mirrors that of epoxy (Figure 3.10(a)). However, increasing the reaction probability to 10% causes a significant increase in the creep strain as the finite number of reactions drives more compliant behavior. Reaction probability also has a significant effect on the void fraction evolution as shown in Figure 3.10(b). Due to void healing in the presence of dynamic reactions, the general trend is that the void fraction is lower with an increase in reaction probability. In the extreme case of a reaction probability of 1.0, the tertiary creep behavior emerges resulting in an increase

in the void fraction at later times. Experimental data also show that the tertiary behavior at later times is specific to cases with high amounts of catalysts[144].

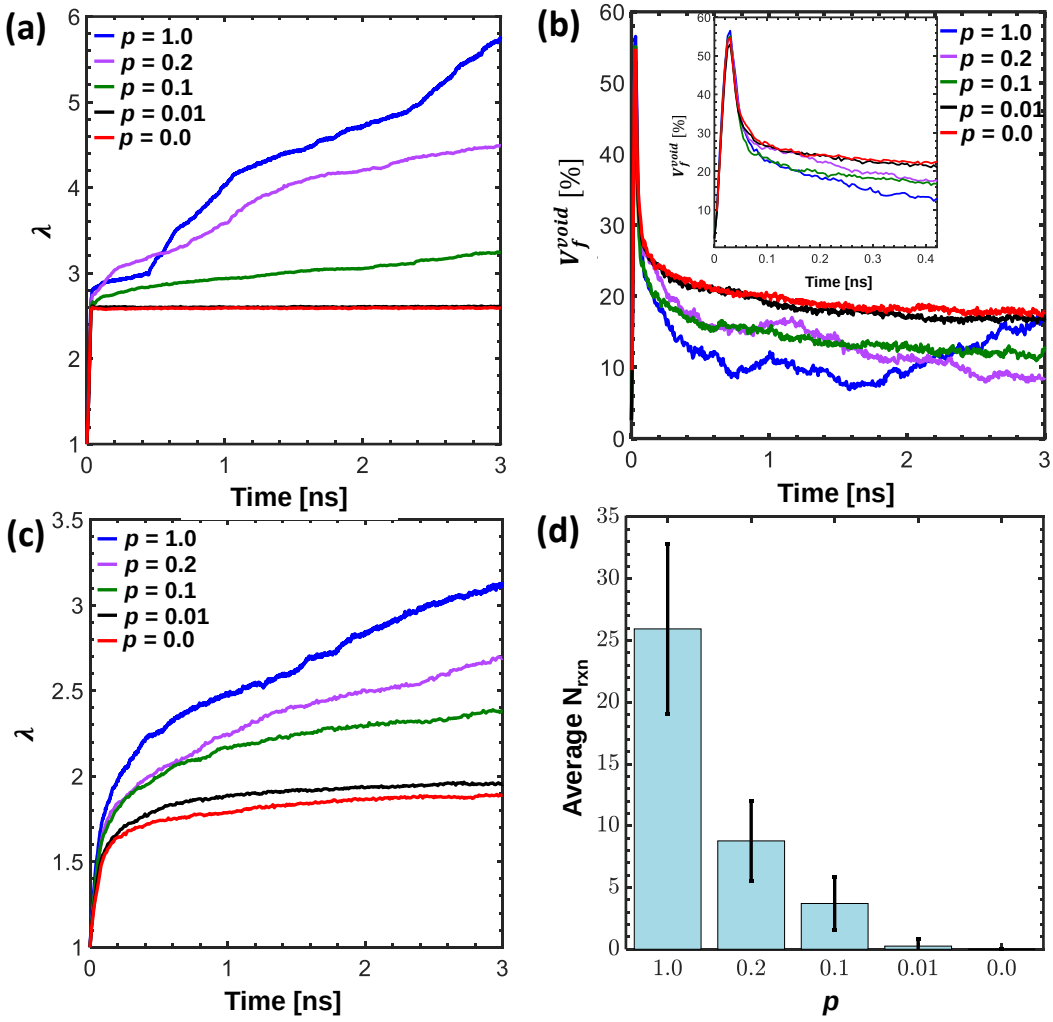

Figure 3.10: Vitrimer under different S−S reaction probabilities at 600 K (a) stretch ratio vs. time at 500 MPa, (b) Void evolution at 500 MPa (c) stretch ratio vs. time for a lower stress level $\sigma = 150$ MPa, (d) average number of reactions per deformation step at 150 MPa

The inset of Figure 3.10(b) shows the rapid increase in void fraction during primary creep is almost identical for all reaction probabilities initially due to the rapidity of loading. Beyond the peak in void fraction, all cases show a drop in the void fraction as the chain mobility leads to a decrease in free volume. However, the general trend of lower void fraction with increased reaction probability is seen during secondary creep

once sufficient time is available for the healing of voids via dynamic reactions. Figure 3.10(c) shows the trends in the creep strain versus time behavior under loading at a relatively lower stress level of 150 MPa. The primary creep regime is more gradual for a lower stress case for all probability cases indicating a closer representation of the laboratory setting of creep experiments (even though the temperature is still elevated). Figure 3.10(d) shows that the increase in the number of reactions per deformation step is consistent with the increase in reaction probability. In Figure 3.10(c), the trend of the increase in the secondary creep rate with an increase in reaction probability can be seen. However, the creep strains at 150 MPa in Figure 3.10(c) are significantly lower than those at 500 MPa in Figure 3.10(a), and the transition from primary creep to secondary creep is smoother due to lower chain mobility at lower applied stresses.

3.4 Conclusions

Vitrimers represent the next generation of epoxies, bringing forth the benefits of processability and recyclability. However, the added benefit of dynamic bonds that allow processability also leads to undesired creep behavior. This paper employed MD simulations to understand the nature of creep mechanisms in polymers with dynamic bonding as compared to cases where there is no dynamic bonding. A model disulfide bond exchange-based vitrimer system was investigated using all-atom large-scale molecular dynamics simulations. A novel approach was developed to simulate creep in vitrimers using topology-based bonding and a combination of NVE and NPT simulations to provide stable simulations in the presence of chemical changes. The following conclusions can be drawn from this study:

- Vitrimer without reaction (equivalent to epoxy) shows a primary creep response which is driven by chain rearrangement and a very slow secondary creep response

due to chain mobility around free-volume.

- Vitrimer with dynamic reactions shows either two or three creep stages depending upon the probability of chemical reactions (equivalent to catalyst concentration and/or temperature).

- In all cases, the first stage is primary creep showing an initial increase in voids due to chain rearrangement as soon as the load is applied followed by a rapid decrease and stabilization of void volume. This behavior is equivalent to epoxy although the void volume is lower in vitrimers due to some healing.

- The second stage of creep is the secondary creep where two processes are in concert: elongation due to chain rearrangement (as in primary creep) but also sudden bursts in chemical reactions driving realignment of bonds orthogonal to the loading direction, thus decreasing the stiffness along the loading axis and increasing the creep strain. Very little void growth is seen, as the voids created during loading are balanced by healing via dynamic bonding.

- Tertiary creep is seen in high reaction probability and high applied stress cases. In addition to the secondary creep mechanisms of void healing, the growth of an isolated large void(s) occurs in this regime which cannot be healed anymore.

Since the slow secondary creep stage is the rate-determining step in the eventual failure of the material, methodologies to mitigate that should be prioritized in vitrimers. As observed in the simulations, the difference between the secondary creep phenomena in epoxies and vitrimers is the ability of dynamic bonding to reorient the bonds with respect to the loading direction. Thus, chemistry changes or additives that can prevent the initial realignment of dynamic bonds can be an effective strategy to mitigate creep in vitrimers. Indeed, a recent work shows that the addition of metal complexes that decrease chain-to-chain interactions can significantly reduce creep in vitrimers[165].

CHAPTER IV

Multi-Scale Modeling of Semi–Crystalline Polymer Actuators

4.1 Background

Fabricated from polymer fibers twisted and coiled into a helix, twisted and coiled polymer actuators (TCPAs) are a novel type of artificial muscle that works by thermal stimulation[31]. They can contract axially or twist when heated above the glass transition temperature of the polymer and return to their original shape when cooled down[31, 32]. The actuator has demonstrated impressive performance in terms of tensile strain (49%), power density (27.12 $\mathrm{kWkg^{-1}}$), and specific work (2.48 $\mathrm{kJkg^{-1}}$)[166]. These capabilities have attracted attention to the potential applications of TCPAs in smart materials, soft robotics, and artificial muscles[167, 168]. TCPAs offer many benefits, such as high contraction ability, high work output, low-cost materials, and simple fabrication, which make them suitable for applications in biomedical devices, soft robotics, and energy-harvesting equipment[32, 168, 169, 170]. However, controlling TCP actuators in a convenient and effective way still poses some challenges[168]. TCPAs-based mechanisms offer large-stroke and a gradual stroke as opposed to the shape-memory alloys(SMAa) which show smaller and sudden stroke due to rapid phase transformation. They actuate upon the stimuli of various forms: electrical,

thermal, and change in pH, etc.[168, 171]. These actuators are made of polymer monofilament fibers that are twisted and coiled in a particular way to create a helically coiled structure. These actuators can contract or extend during their actuation, depending on the twist direction w.r.t the coil axis, cooling or heating, etc. Despite a promising scope of potential applications of TCPAs in various fields, there are also some key challenges associated with these actuators that limit their usage, such as their relatively slow response times and difficulty in controlling their complex motion, creep behavior, and sensitivity to moisture. Ongoing research is focused on developing new materials, heating and cooling strategies, and understanding their performance, design strategies, and alternative materials toward large actuation forces to address these challenges and improve the performance of TCPA muscles[172].

Developing computational models with predictive capabilities is important to understand the actuation mechanisms, and improve the performance metric of the TCPA actuators. A numerical model can help explore the design space of material parameters, fabrication processes, geometric parameters of the coil, and the nature of loading conditions (both thermal and mechanical). There have been several analytical models, energy-based models, and beam theory-based models developed[173]. Pawloski el al. proposed a beam formulation-based model that includes the change in coil length as a function of temperature. However, such a model assumes the load vs. deflection relationship is known from tests conducted under different conditions of the muscle as a whole. Zhang et al. developed a model for the supercoiled TCPA that captures the hysteresis which is an important[174]. An analytical model that captures the multiphysics of the electroactuation via Joule's heating, models the TCPA using Love's beam theory.[175]. The majority of such beam formulations-based models lacks to capture the large deformations and deflections that a TCPA undegoes. Towards this aspect, in a study by Sun et al., the TCPA is modeled using Elastica cosserat rod theory that captures the large deflections[176]. However, this model lacks the inclu-

sion of the microstructure and how the twist changes it and its effect on the situation response, instead, it models the bulk-level behavior of the twisted fiber[176]. An energy-based semi-analytical formulation was proposed by Yang and Li that takes into consideration of the nano-scale deformation mechanisms of a continuum-scale model[177]. It captures the twist by modeling the orientation rotation as a function of the radius. It is a computationally efficient model that captures the material non-linearity and spatial variation well. However, it also lacks the full description of the geometry. Its applications are limited to a simple coil-shaped geometry which is present in most cases, however, it fails to consider the non-linear large geometrical deformations.

These models use either curve-fitting of the actuation or lack the detailed material and geometrical description that influences the extent of physics captured in the model. A full 3D finite element model with detailed material properties assignments has not been developed and used to look into the actuation mechanisms of a TCPA, and which is the focus of this work. We use the multi-scale description of the twisted fiber proposed by Yang and Li which is discussed in the method section in detail.

4.2 Methods

4.2.1 MD simulations of Nylon 6,6

The highly drawn fibers, such as the fishing line made of Nylon 6,6, acquire their transversely isotropic material properties as a result of the difference in the material properties of the crystalline and amorphous phases[178, 179, 180]. Nylon 6,6 achieves a crystalline phase as a result of hydrogen bonds between partially positively charged amine hydrogen and partially negatively charged oxygen atoms in the adjacent layers[179]. The molecular dynamics simulations of the amorphous phase of Nylon 6,6 are conducted to look at the thermal expansion behavior of both phases,

separately.

4.2.1.1 Amorphous Nylon 6,6

Nylon6,6 is synthesized by polycondensation reactions between Hexanedioic acid (also known as adipic acid) and Hexane-1,6-diamine (commonly known as hexamethylenediamine). Figure 4.1 shows the molecular structures of the monomers and the periodic cell containing the monomer mixture that is used from the work of Gissinger et al. [76]. The mixture is equilibrated at a density of 0.8 gcm^{-3} followed by the polycondensation reactions which happen in two steps, first, the nitrogen of hexamethylenediamine forms a bond with the carbon atom of the carboxylic acid site, then the proton released from nitrogen forms the water molecule with the remaining OH, therefore, releasing a H_2O molecule. The pre– and post–reaction templates for this reaction can be found in the work of Gissinger et al.[76]. The polymer consistent force field (PCFF) is used to define the bonded interactions and a cutoff value of 12.5 Å for the non-bonded interactions prescribed by Coloumbic and LJ potentials.

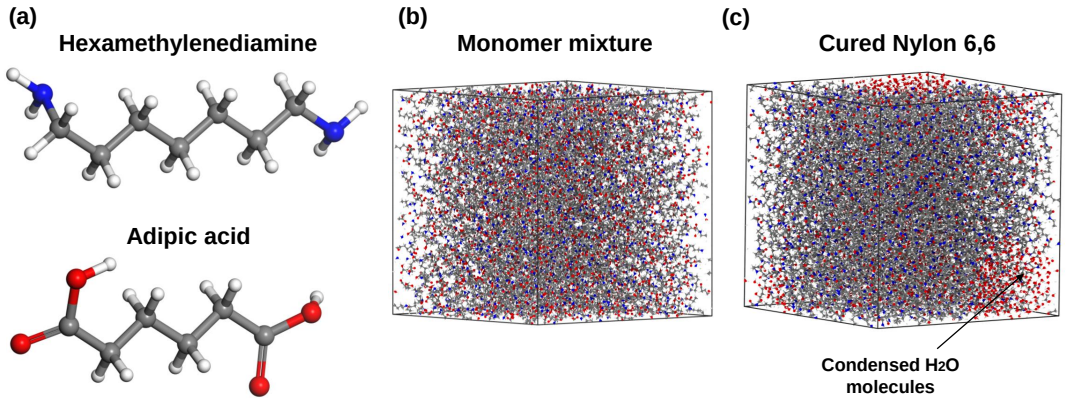

Figure 4.1: (a) Monomer structures and (b) 3D periodic box containing monomer mixtures and (c) the cured Nylon 6,6 with condensed water molecules in the MD box

The reactions were run every 20 ps and for a total of 1 ns, resulting in the degree of cure of $\sim$ 99% in all 3 replicas. The cured system by reactions inherently has

high intra-chain stresses, therefore, the MD box is annealed by heating to 600 K and cooling down to 10 K under 1 bar pressure (NPT conditions), and these cycles of 200 ps are repeated until an equilibrated density is achieved. Figure 4.2 shows the thermal cycling carried out for 5 ns. Then the box is equilibrated at 300 K for 1 ns saturating the mass density at $\rho = 1.026$ gm^{-3} which is close to predicted in an all-atom MD study in literature[181]. The experimentally measured pure amorphous phase Nylon 6,6 density is 1.085–1.090 gm^{-3} [182, 180, 179], therefore, the MD simulations are able to achieve the density within 5% of error at 300 K. This validates the applicability of the PCFF force field for volumetric packing of the amorphous structure.

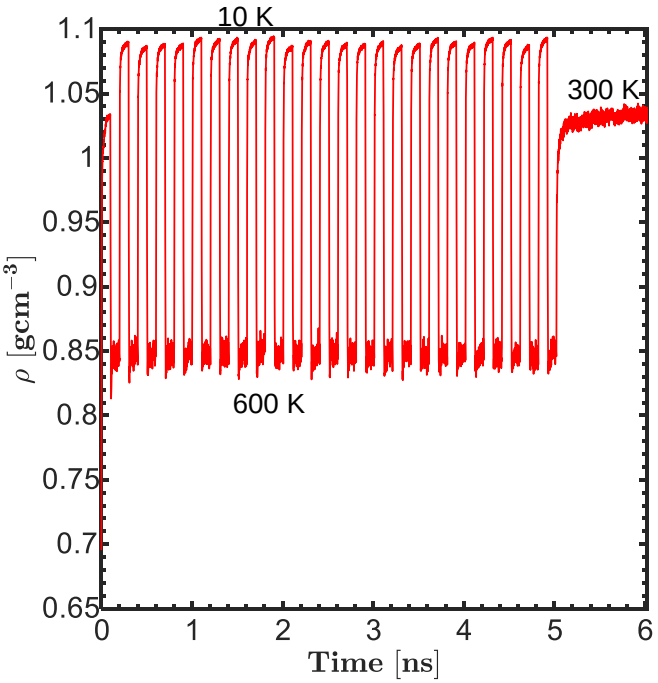

Figure 4.2: Mass density vs. time during annealing cycles of cured amorphous Nylon 6,6

The dilatometric behavior of the pure amorphous phase is studied by cooling it down from 600 K to 100 K in the steps of 10 K where the MD box is relaxed at each temperature step for 200 ps. The volume and the density are averaged for the last 10 ps for each temperature step and used to evaluate the thermal expansion behavior and the glass transition temperature of the Nylon 6,6. The thermal expansion computation

and the results are discussed in the later sections.

4.2.1.2 Crystalline Nylon 6,6

The fishing line made out of Nylon 6,6 comprises crystalline and amorphous phases. In this work, we also focus on the pure crystalline phase of Nylon 6,6 and specifically we look at the dilatometric behavior of $\alpha-$triclinic structure of the crystalline phase which is more prominently observed in these fibers. The structure of a single chain is constructed in Material Studio and placed in a triclinic box with lattice parameters: $a = 4.9$ Å, $b = 5.4$ Å, $c = 17.2$ Å and unit cell angles, $\alpha = 48.5^o$, $\beta = 77^o$, $\gamma = 63.5^o$. A single chain in the periodic unit cell is shown in Figure 4.3(a) and (b), respectively show a unit cell and the constructed MD box containing 38,000 atoms by repeating this unit cell in all three dimensions 10 times.

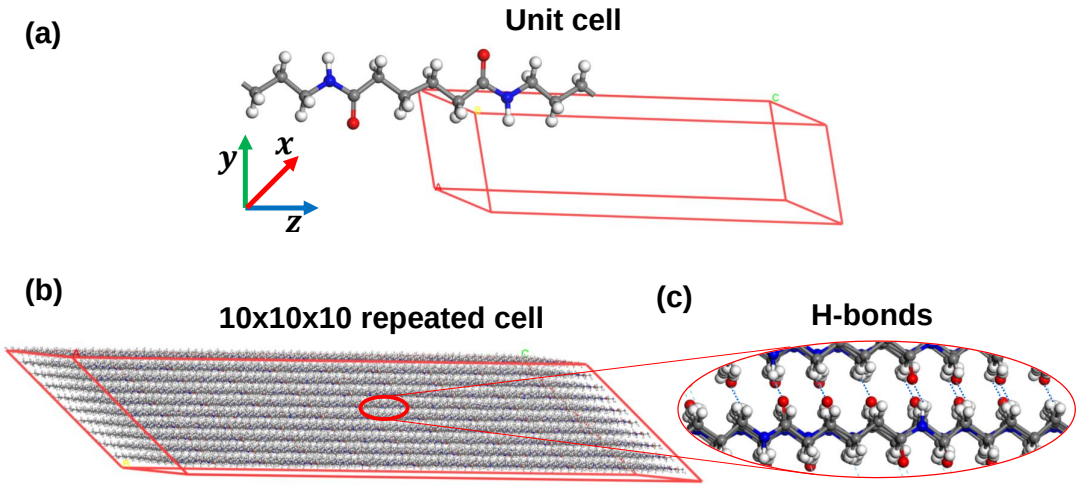

Figure 4.3: (a) The unit cell of the $\alpha-$triclinic crystal, (b) $10 \times 10 \times 10$ repeated units making an MD box with dimensions $4.9 \times 5.4 \times 17.2$ nm^3 of Nylon 6,6, and (c) the hydrogen bonds between adjacent molecular chains formed between amine hydrogen and double bonded oxygen

The nitrogen in the amine group pulls electrons towards itself, resulting in a slightly positively charged hydrogen, on the other hand, oxygen in the carboxylic group is partially negatively charged[183, 180, 184, 1, 26, 185, 2, 186]. Therefore, an inter-

chain Hydrogen bond forms that are responsible for the crystalline structure of Nylon 6,6 in this arrangement (shown in a zoomed view in Figure 4.3(c))[187]. It is to be noted that this H-bonding forms only in one plane, therefore, flat platelets-like structures are the building blocks that stack together to form the 3D crystal. In a unit lattice of a crystal, the bonds are repeated over the periodic boundary which makes it an infinitely long chain. However, the repeating chains are ended by adding extra hydrogen on the ends in the longest dimension of the box. This is done to simulate the system with finitely long chains. The MD box shown in Figure 4.3(b) is exported for simulations in LAMMPS. The PCFF force field is used to describe all the interactions as discussed in the case of the amorphous-phase MD simulations. The box is equilibrated by running an NPT simulation at 1 bar and 300 K conditions, and the relaxed mass density is $\rho = 1.19$ gcm^{-3} which is within 3% accuracy of the experimentally measured value of $\rho = 1.22$ gcm^{-3}[180]. Therefore, the PCFF is an adequate choice of force field that is able to atomic packing the lattice. We use this model to look at the thermal expansion behavior of the crystalline Nylon 6,6 and the results are discussed in the later sections.

4.2.2 Finite element model of the TCPA

In this work, a micro-structure-based finite element model is developed for the twisted and coiled polymer actuators. The drawing process of the semi-crystalline polymer leads to anisotropy in the fibers of which the TCPAs are made. These monofilament fibers are transversely isotropic in nature[184, 1, 26, 185, 2, 186]. The crystalline phase is preferentially aligned along the fiber axis as a result of a high draw ratio[2]. The TCPA muscles are fabricated by twisting a straight semi-crystalline fiber followed by coiling the twisted fiber by itself or around a mandrel [31]. These fibers are drawn from the semi-crystalline polymer pallets to a high draw ratio. This drawing process leads to the fiber being transversely isotropic [1, 2]. The drawn fibers have a micro-

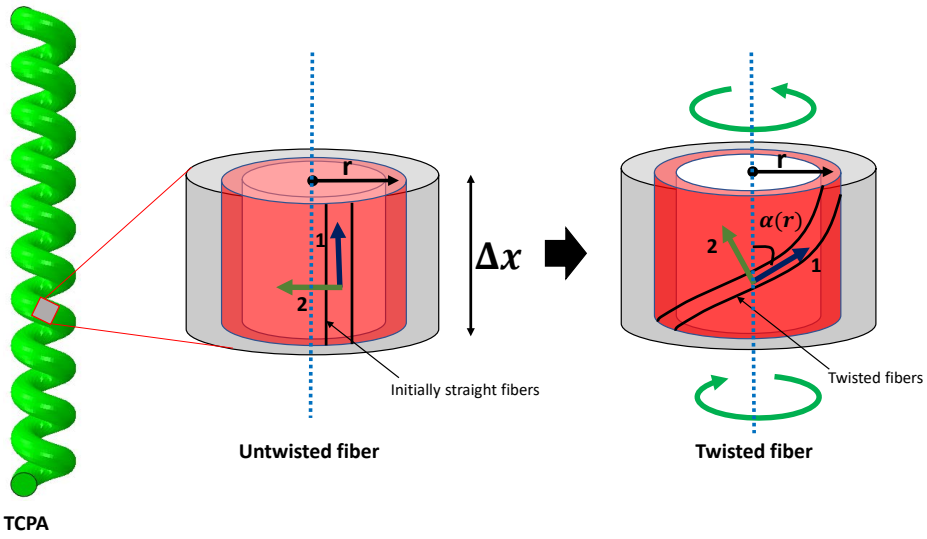

Figure 4.4: Initially straight fibers and twisted state of semi-crystalline material fibers in a TCPA

structure with the crystalline phase being highly oriented along the draw direction and randomly oriented in the fiber cross-section [26]. The basis of the model lies in the assumption about the microstructure rotates with the geometric twist introduced in the Nylon fiber during the fabrication process of the actuator[177]. Consider an infinitesimal segment of the fiber in the muscle, upon introducing the twist in these fibers, the crystalline phase short fiber-like structures subtend an angle with the fiber axis as shown in Figure 4.4. This angle or orientation varies with the radius (r) of the fiber as [177]:

$$\alpha(r) = \arctan\left(\frac{r}{r_f}\tan(\alpha_f)\right) \tag{4.1}$$

where r_f is the fiber radius and α_f is the twist angle at the surface of the fiber and this can be determined from the measurements in the experiments. The angle of twist ($\alpha(r)$) is a continuous function of radial location from the fiber axis. In this FE model, we divide the fiber cross-section into concentric laminates with the radially varying orientation given by Eqn. 4.1.

The following key assumptions are made about the drawn fiber after it is formed in a TCPA muscle:

- No residual stress is present after annealing of the TCPA.
- Microstructure is not altered by the annealing during the fabrication process.
- The amount of twist is a function of the radial location on the fiber and follows a geometric relation given by Eqn. 4.1
- No creep occurs i.e. assuming the model to be time-independent

The precursor fiber is annealed before it is used for the fabrication of the TCPA. The annealed fiber is tested along the axial direction under temperature sweep in a dynamic mechanical analyzer (DMA). Figure 4.5(a) shows the coordinate system used to label the material properties, Figure 4.5(b) to (d) show the temperature-dependent properties of the precursor fiber elastic properties. The Posson's ratio in all three directions is assumed to be 0.33 and temperature independent. The thermal properties of the highly drawn Nylon 6,6 fiber are shown in Figure 4.6(a)-(b), where the data points are taken from the work of Choy et al., and a non-linear curve is fit and extrapolated to higher temperature ranges[1, 2].

4.2.2.1 Transversely isotropic materials

A general three-dimension fully anisotropic elasticity tensor has 21 independent. If there are three planes of symmetry, the number of independent constants in the elasticity tensor reduces to 9. Transverse isotropy is a special case of an orthotropic elasticity tensor with one plane of isotropy where the properties in that plane are rotation independent. A transversely isotropic elasticity tensor has 5 independent constants. One of the common examples of a transversely isotropic material is fibrous composite lamina or a laminate made up of laminae stacked in the same direction.

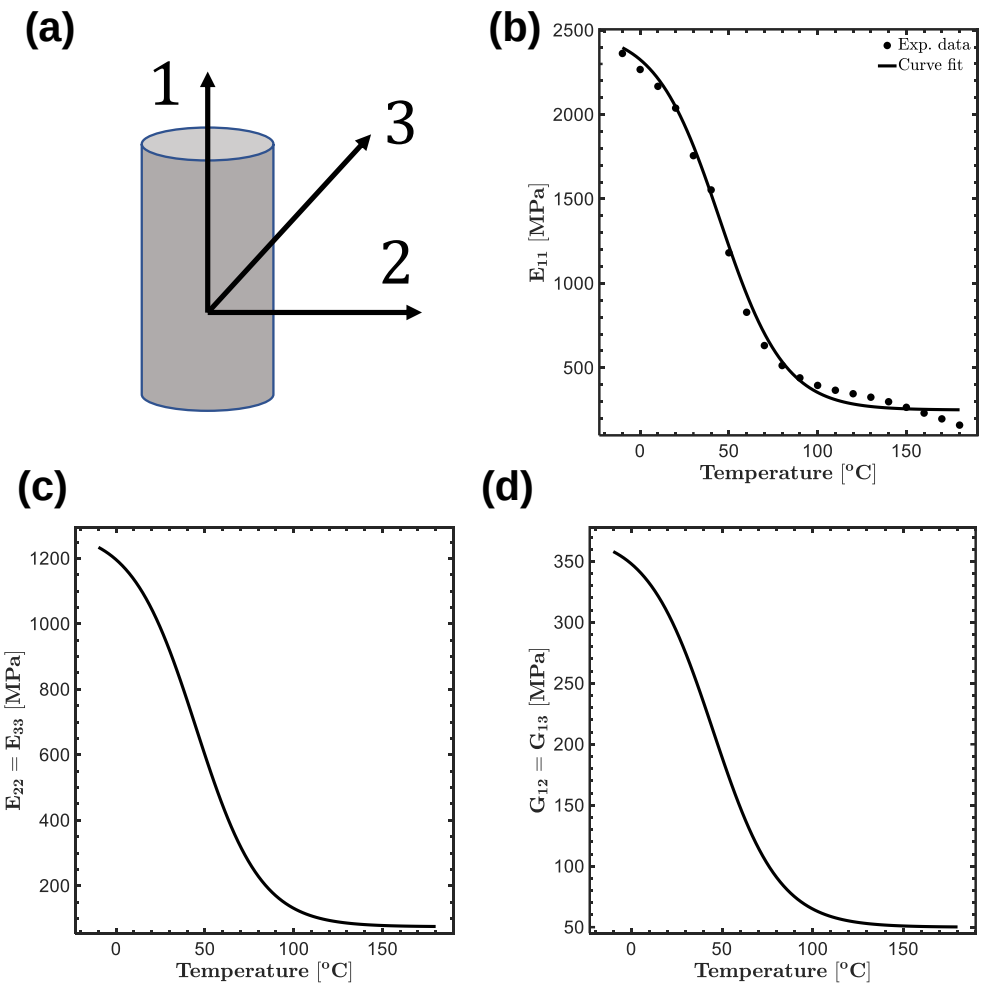

Figure 4.5: (a) Coordinate system for the precursor fiber, (b) the modulus along the fiber-axis (courtesy of Prof. Sameh Tawfick's research group at UIUC), (c) elastic modulus in the radial or transverse direction, and (d) the shear modulus along the torsional direction of the fiber

Hooke's law for a transversely isotropic material relates the stress and strain tensors as follows:

$$\sigma_{ij} = C_{ijkl}\epsilon_{kl} \tag{4.2}$$

where C_{ijkl} is the fourth-order stiffness tensor of material properties or elastic moduli. For a transversely isotropic material, the stiffness tensor has the form:

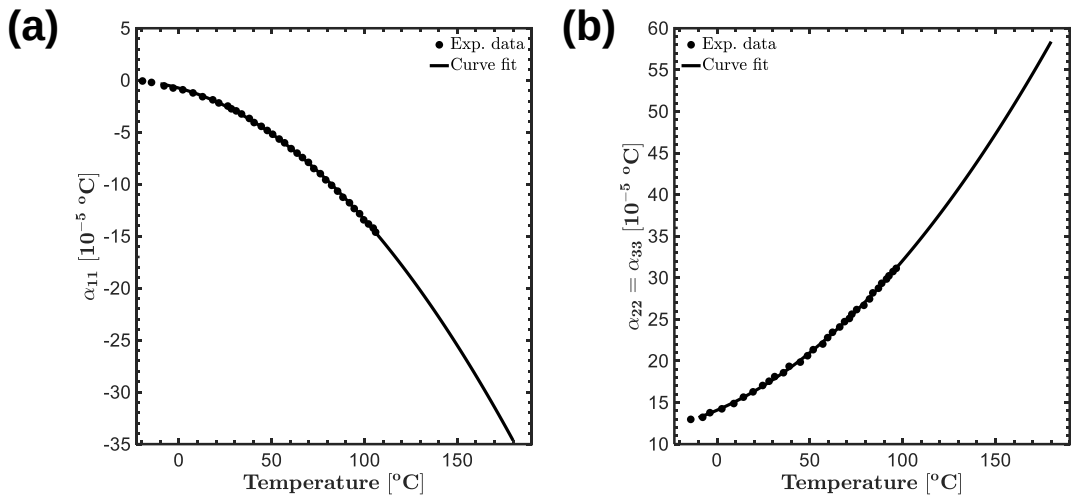

Figure 4.6: (a) The coefficient of thermal expansion along the fiber axis ($\alpha_{11}(T)$) and (b) in transverse or radial directions ($\alpha_{22}(T) = \alpha_{33}(T)$), the data points are considered from Choy et. al[1, 2]

$$\begin{bmatrix} \sigma_x \\ \sigma_y \\ \sigma_z \\ \tau_{xy} \\ \tau_{xz} \\ \tau_{yz} \end{bmatrix} = \begin{bmatrix} C_{11} & C_{12} & C_{13} & 0 & 0 & 0 \\ C_{12} & C_{11} & C_{13} & 0 & 0 & 0 \\ C_{13} & C_{13} & C_{33} & 0 & 0 & 0 \\ 0 & 0 & 0 & C_{44} & 0 & 0 \\ 0 & 0 & 0 & 0 & C_{44} & 0 \\ 0 & 0 & 0 & 0 & 0 & (C_{11} - C_{12})/2 \end{bmatrix} \begin{bmatrix} \epsilon_x \\ \epsilon_y \\ \epsilon_z \\ \gamma_{xy}/2 \\ \gamma_{xz}/2 \\ \gamma_{yz}/2 \end{bmatrix} \tag{4.3}$$

An inverse relation can be written as:

$$\epsilon_{ij} = S_{ijkl}\sigma_{kl} \tag{4.4}$$

where S_{ijkl} is a fourth-order compliance tensor which can further be written in terms

of engineering constants of the material as follows:

$$\begin{bmatrix} \epsilon_x \\ \epsilon_y \\ \epsilon_z \\ \gamma_{xy}/2 \\ \gamma_{xz}/2 \\ \gamma_{yz}/2 \end{bmatrix} = \begin{bmatrix} 1/E_1 & -\nu_{12}/E_1 & -\nu_{12}/E_1 & 0 & 0 & 0 \\ -\nu_{12}/E_1 & 1/E_1 & -\nu_{23}/E_3 & 0 & 0 & 0 \\ -\nu_{12}/E_1 & -\nu_{23}/E_3 & 1/E_3 & 0 & 0 & 0 \\ 0 & 0 & 0 & 1/G_{23} & 0 & 0 \\ 0 & 0 & 0 & 0 & 1/G_{13} & 0 \\ 0 & 0 & 0 & 0 & 0 & 1/G_{12} \end{bmatrix} \begin{bmatrix} \sigma_x \\ \sigma_y \\ \sigma_z \\ \tau_{xy} \\ \tau_{xz} \\ \tau_{yz} \end{bmatrix} \tag{4.5}$$

4.2.2.2 TCPA geometry and choice of mesh

The coil is partitioned into 5 concentric helical annulii and is created by revolving a circular cross-section about the coil axis. Figure 4.7(a) shows the geometry of 5 coils modeled to reduce the computational expenses. The TCPA coil is defined by the fiber diameter (d_f), coil diameter (D_{coil}), and coil pitch (p_{coil}), therefore, the total length of the coil considered in the FE model is $L_{coil} = 5 \times p_{coil}$. The top face shows five partitions created and their respective orientations are assigned, the procedure for the same is described in the next subsection. The 3D geometry is discretized using second-order tetrahedron elements (C3D10) mesh (shown in Figure 4.7(b)). The nodes on the top face are constrained in all translation directions ($u_x = u_y = u_z = 0$). The bottom face nodes are constrained to a rigid-body reference node which is constrained in rotation about global $y-axis$ and a load is applied downward as done experimentally.

4.2.2.3 Material orientation in ABAQUS

As described in the previous subsection, the TCPA can be modeled as a set of the finite number of concentric laminate made up of the same ply with a rotated material orientation by an angle described by Eqn. 4.1. Figure 4.8(a) shows a coil with concentric partitions. Now, the objective is to assign a local material orientation to material points of the TCPA based on their radial location from the helix axis.

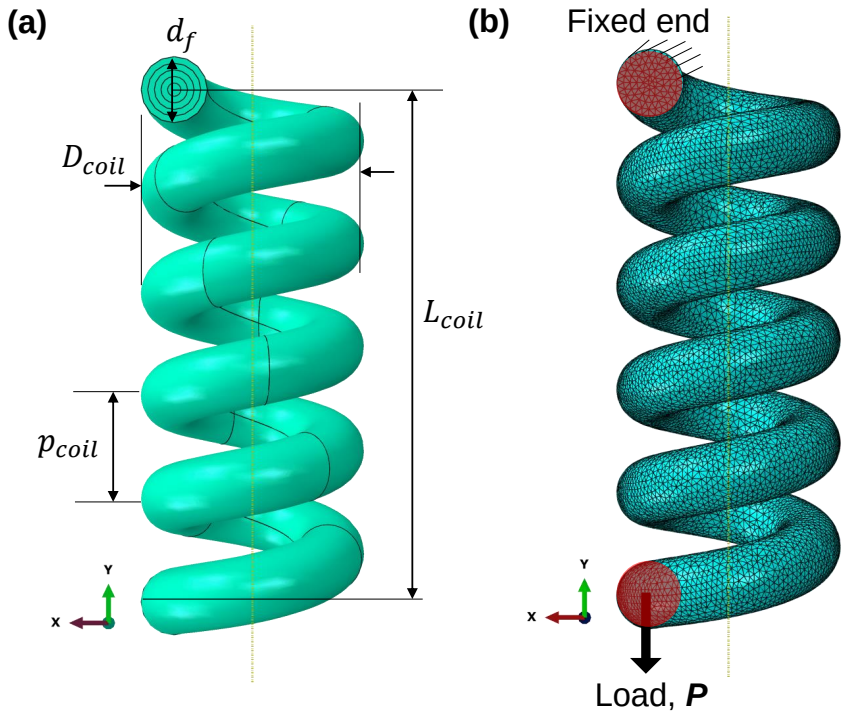

Figure 4.7: (a) Geometry of a TCPA coil with concentric helical annular partitions showing different coil dimensions and (b) the finite element mesh showing the boundary conditions at the top and bottom ends of the coil

It can be achieved by writing a material orientation subroutine but ABAQUS/CAE offers a simpler approach. We utilized the simplicity of the helix geometry to assign the material orientation in this problem. We used the discrete material orientation option in ABAQUS/CAE[188]. We use the normal of the coil surface as one direction $(3-axis)$, the helix axis as the second direction $(2-axis)$, then the third direction $(1-axis)$ is automatically computed which aligns along the circumference of the helix at a fixed location on its axis (shown in Figure 4.8(b)). Now the twist angle can be assigned by rotating this coordinate system about $3-axis$ which is normal to the coil surface. The solid arrows show the orientation computed based on geometry and the dashed arrows indicate the rotated direction after assigning the angle of twist. This rotation angle $(\alpha(r))$ is computed for a partition based on its mean radial location and shown in Figure 4.8(c).

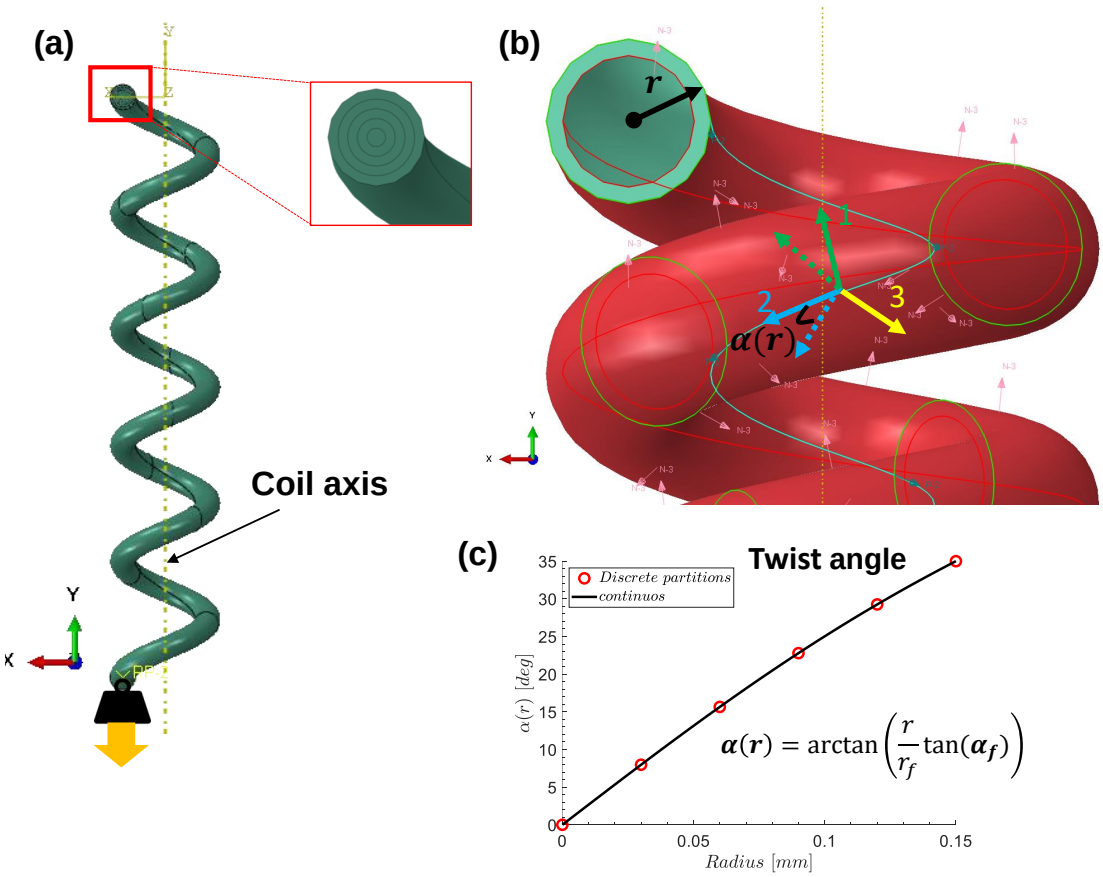

Figure 4.8: (a) The solid model of the coil with inset showing the concentric partitions, (b) discrete orientation definition based on the surface normal $(3-axis)$ and helix direction $(2-axis)$ and the rotation of $3-axis$ to assign the twist value, and (c) the angle of twist as a function of radial location of the concentric partition

4.3 Results and Discussion

Computational studies of semi-crystalline polymer-based twisted and coiled actuators are conducted in this work. We utilize a multi-scale approach to understand the thermal behavior of the semi-crystalline polymer at the nanoscale, and we develop a finite element model of the TCPA muscle at a continuum scale that captures the physics of the fabrication process. In this section, the results are discussed for the following studies:

- **MD simulations at nanoscale**: The thermal response of the Nylon 6,6 in its pure amorphous and pure crystalline phases.

- **FE simulations at continuum scale**: The results of the continuum scale of the twisted and coiled actuator are discussed and an in-depth actuation origin is studied with parametric studies based after validating the FE model.

4.3.1 Thermal Response of Nylon 6,6

Molecular dynamics simulations are conducted for the dilatometric behavior of Nylon 6,6 in its pure amorphous and pure crystalline states.

4.3.1.1 Amorphous phase

The equilibrated and relaxed structure of the cured and annealed amorphous phase is taken through a temperature sweep from 500 K to 45 K. The temperature is increased in the steps of 5 K and the box is let to relax for 200 ps at each temperature, therefore, the cooling rate is 0.025 K/ps. Figure 4.9 shows the density vs. temperature of the amorphous Nylon 6,6. All three replicas of the MD system which were cured and annealed separately, show an excellent repetition demonstrating that the system is uniform and reproducible. The density drops as the system is heated up going through the glass transition. The glass transition (T_g) is computed by computing slopes in the low-temperature region and another in a high-temperature regime of this curve shown in dashed black lines). The point where these linear fit intersects is referred to as the glass transition temperature of a polymer[189]. Based on these calculations, the obtained glass transition temperature for Nylon 6,6 is 325 K or 52 ^{o}C (indicated by the vertical blue line). The experimentally observed T_g value is in the range of 45-55 ^{o}C[190] and also investigated in another computational study[181], therefore, MD simulations predictions are in a close match with that observed in literature.
Similarly, to further analyze the thermal expansion behavior, the change in volume

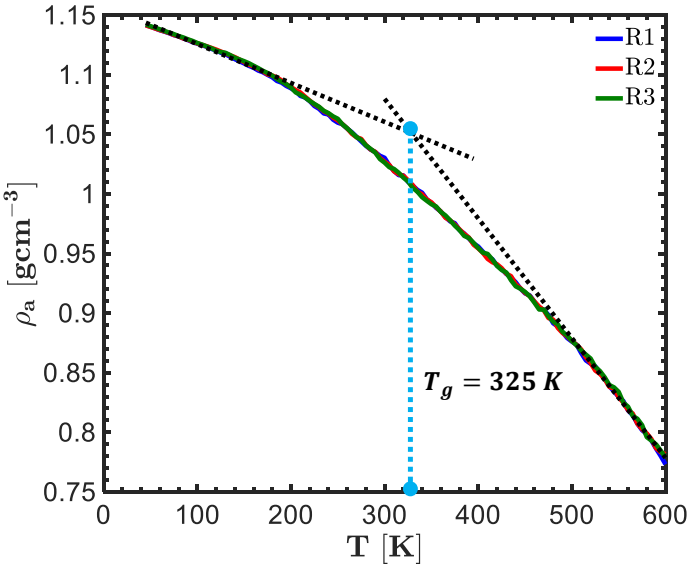

Figure 4.9: Density of the pure amorphous phase vs. temperature of Nylon 6,6, and where, R_1 to R_3 refers to three different replica studied in MD simulations, and dashed black lines are the linear fit and blue dashed line indicate the T_g location

vs. temperature is plotted (Figure 4.10). The change in volume is computed as:

$$\frac{\Delta V(T)}{V_o} = \frac{(V(T) - V_o)}{V_o} \tag{4.6}$$

where, V_o is the volume of the MD box at a reference point and we considered this reference point to be 300 K, therefore, $V_o = V_{300K}$. The factor of 1/3 is multiplied to calculate the linear one-dimension length change. Volume change takes into account the change in length along all three dimensions as a result of the isotropic nature of the amorphous phase.

As shown in Figure 4.10, a polynomial of degree 3 is fit in the data points to fit using least square regression in MATLAB. The polynomial fit between T and $\frac{\Delta V(T)}{V_o}$ takes the following forms:

$$f(T) = C_3T^3 + C_2T^2 + C_1T + C_0 \tag{4.7}$$

The next step is to evaluate the coefficient of thermal expansion (CTE) which is defined as $\alpha(T) = \frac{\Delta L}{L_o(T-T_o)}$. Therefore, we can get the CTE by taking the first

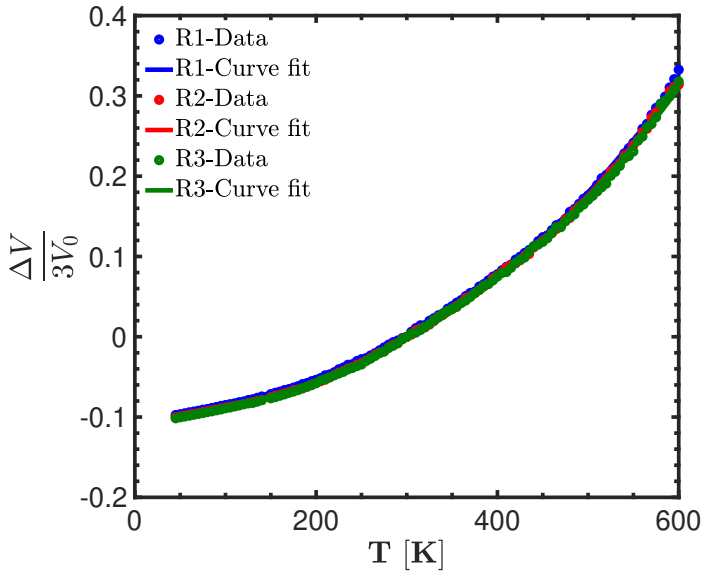

Figure 4.10: Normalized change in volume vs. temperature of Nylon 6,6, and where, R_1 to R_3 refers to three different replica, markers and solid line indicate the data points from MD and curve fit, respectively

derivative of Eqn. 4.7 with respect to Temperature:

$$\frac{df(T)}{dT} = 3C_3T^2 + 2C_2T + C_1 \tag{4.8}$$

Figure 4.11 shows the CTE for amorphous Nylon 6,6 as a function of temperature computed using Eqn. 4.8 for all three replicas studied in this work. It is evident that the thermal expansion is a non-linear function of temperature and shows a very small variation among different MD replicas.

Furthermore, thermal expansion coefficients at 300 K from MD simulations is 28.38×10^{-5} $^o\text{C}^{-1}$ and the experimentally observed CTE for amorphous is 17.86×10^{-5} $^o\text{C}^{-1}$ [1, 2].

4.3.1.2 Crystalline phase

The $\alpha-$triclinic phase which is the most prominent phase of Nylon 6,6, is simulated for its thermal response. The temperature of the box is increased from 200 K to 900 K in the steps of 20 K and the box is relaxed for 200 ps at each temperature step.

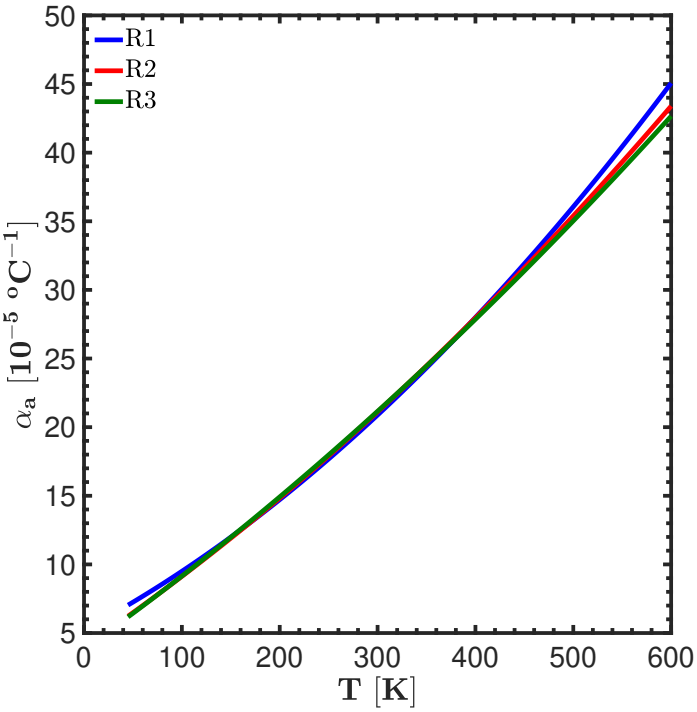

Figure 4.11: Thermal expansion coefficient vs. temperature of Nylon 6,6, and where, R_1 to R_3 refer to three different replicas studied in MD simulations

Figure 4.12 shows the density of the crystalline phase with temperature. There is a clear phase transformation transition at 580 K which indicates the melting point. However, the experimentally observed melting point of the Nylon 6,6 crystalline phase is 513 K, therefore, MD simulations are over-predicting the melting point. This is due to the fact that we are simulating the continuous periodic single crystal which assumes infinite dimensions in the in-plane directions. This results in limiting the mobility of the ordered chains in sliding mode over each other.

This is a crystal with hydrogen bonds in one plane, another plane has Van der Waals interaction between adjacent chains, and the third dimension has long chains connected by covalent bonds. Therefore, the thermal expansion response is orthotropic which means the deformation in response to temperature is different in the three principal directions. Figure 4.13 deformation of the simulations box in each dimension. The three directions are the three principal directions of a cubic box and are referenced as per the coordinate system defined in Figure 4.3(a). The thermal expan-

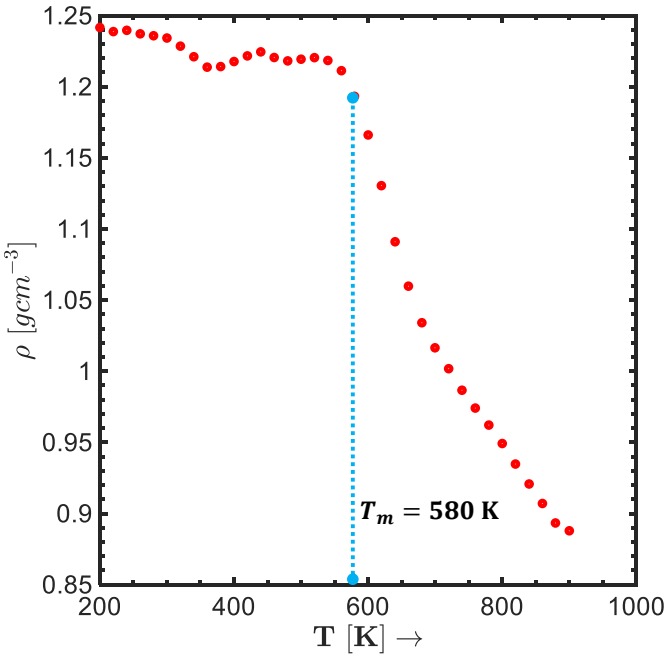

Figure 4.12: Density vs. Temperature for pure crystalline Nylon 6,6, the vertical dashed blue line indicates the melting point (T_m)

sion in $z-$direction is negative which is attributed to the covalent bonded long chains along this direction that contracts upon raising the kinetic energy of the system. This is similar to what has been observed experimentally for the crystalline phase in chain-direction[1, 2]. These covalently bonded chains are one of the reasons for the negative thermal expansion of the highly drawn fibers along their drawing axis as the longest axis of the crystalline phase platelets aligns in this direction.

The transverse directions, even though different extents, show positive thermal expansion upon heating beyond melting. From 200 K to 400 K, the $x-$direction shows contraction upon heating but the slope (or the coefficient of thermal expansion) is lower as compared to $z-axis$. This is the plane in which hydrogen bonds form between two adjacent chains. These hydrogen bonds form a planar sheet and contract in size upon heating, and also observed experimentally [191] However, the $y-axis$ expands upon heating throughout the temperature range. Two planar sheets stack along this direction via van der Waals forces, therefore, the average distance between

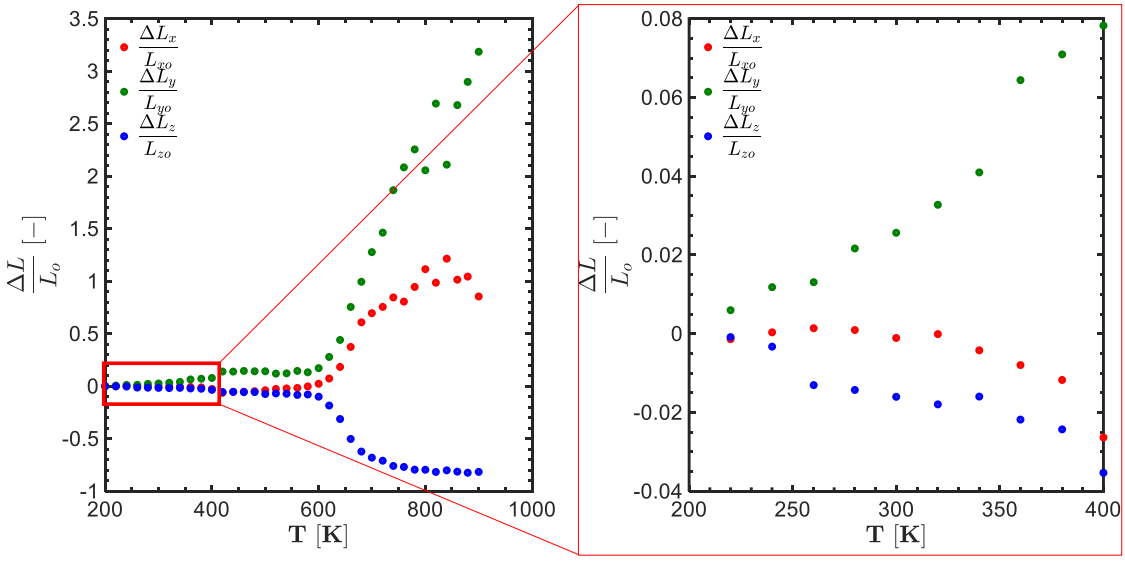

Figure 4.13: Normalized length change vs. Temperature for pure crystalline Nylon 6,6 for three principal axes (indicated by different colors), a zoomed view is shown on the right

these chains increases upon heating the system and suddenly the system collapses along this direction at the melting point. The sudden collapse occurs due to the loss of order in the structure between two chains, and the long chains are able to bend to a large extent resulting in the loss of hydrogen bonds and the structure of the planar sheets.

4.3.2 Simulations of TCPA actuation

The developed FE model is checked for basic features of the TCPA actuators. Verification of the FE model is necessary and helps to ensure whether the model is able to capture the intended physics included in it. The TCPA FE model is verified for the basis actuation response as per the physics of the problem. The coil geometry and the non-linear material properties including in the cylindrical laminates make the problem highly non-linear, and therefore, harder to test on much simpler loading cases. However, the FE model can be tested for some special twist angles of the

muscle is a feature the model should capture to ensure the model's adequacy. There are two ways to introduce the twist in the fiber during the fabrication process. When the twist in the muscle is introduced in the same direction as the orientation of the helical coil, this is referred to as homochiral muscle (shown in Figure 4.14(a))[31]. However, when it is opposite to the coil-helix, it is called heterochiral muscle[31]. The homochiral configuration results in a contracted actuation while the heterochiral muscle shows extension upon heating[31, 32].

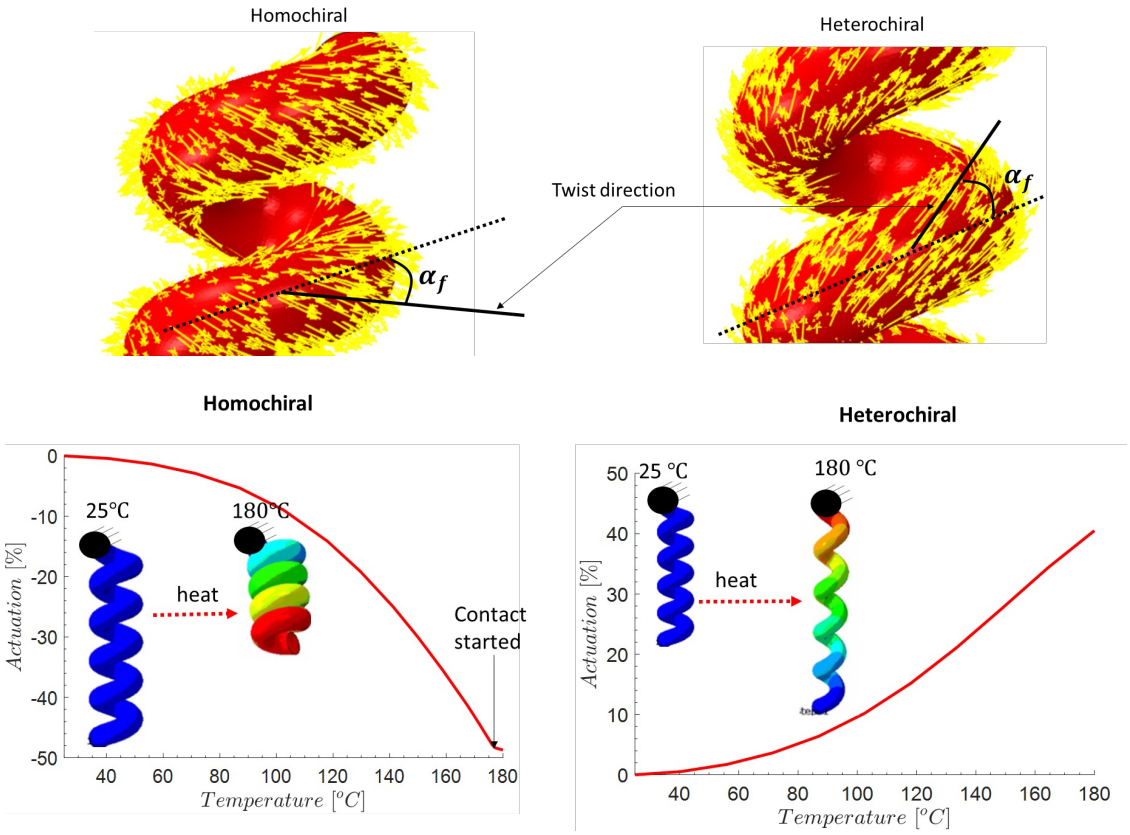

Figure 4.14: The influence of chirality of the muscle: free actuation response for homochiral (left) and heterochiral (right)

Table 4.1: Coil parameters used for FE model studies of Chirality, number of partitions, and angle of twist

Coil parameter	D_{coil}	d_f	p_{coil}	α_f
Value	0.76 mm	0.30 mm	0.53 mm	35^o

Note the direction of the yellow arrows that indicate the orientation of the twist on the

surface of the coil (rotated $2-axis$ in Figure 4.8(b)). The FE model is developed for the muscle parameters given in Table 4.1. Figure 4.14 (b) shows that the developed FE model captures this orientation dependence of the introduced twist with respect to the coil-helix. In the case of a straight fiber which twists introduced in it, that can be thought of as concentric laminates with different orientations. Upon heating such a fiber, the difference in thermal expansion in axial and radial direction will result in a coupling between its axial and torsional response. Therefore, as the fiber will contract axial upon heating, there will be a torsional twist about its axis which means the fiber would have a tendency to untwist from its originally twisted configuration. Now in the case of a coil that has a twisted fiber will result in a coupling between the axial, torsional, and bending of the fiber axis due to its curved geometry. Therefore, the contraction of the coil is a bulk motion as a result of the bending of the coil axis. However, the direction of bending depends on the twist direction about the coil axis which is how we defined the chirality of the TCPA muscle. For a heterochiral TCPA, the bending occurs in the direction that results in the separation of two coils from each other, therefore, an extension of the muscle upon heating.

4.3.2.1 Influence of number of partitions

A key assumption made in this FE model is that the TCPA can be represented as a finite number of concentric helices. Therefore, we tested the TCPA response for the cases when we divide the cross-section into 5 or 10 concentric partitions (shown in Figure 4.15(a)). The muscle parameters considered for this study are given in Table 4.1. The discretized twist angle for each annulus is computed at its outer radius. Figure 4.15(b) shows the contraction as a percent of the coil's initial length. It is evident that the 5 partitions are enough to represent the concentric helices FE model. The lower number of partitions case shows more contraction which is expected as thicker annuli have larger twist angles assigned to them since the twist

angle value is computed at the outer radius of the annulus. This difference grows more with high temperature as the larger deformation occurs at a higher temperature, therefore, a more pronounced difference in the actuation response between the two cases. However, the difference is less than 5% at the maximum temperature location which is reasonable as the lesser number of partitions model saves on FE mesh size.

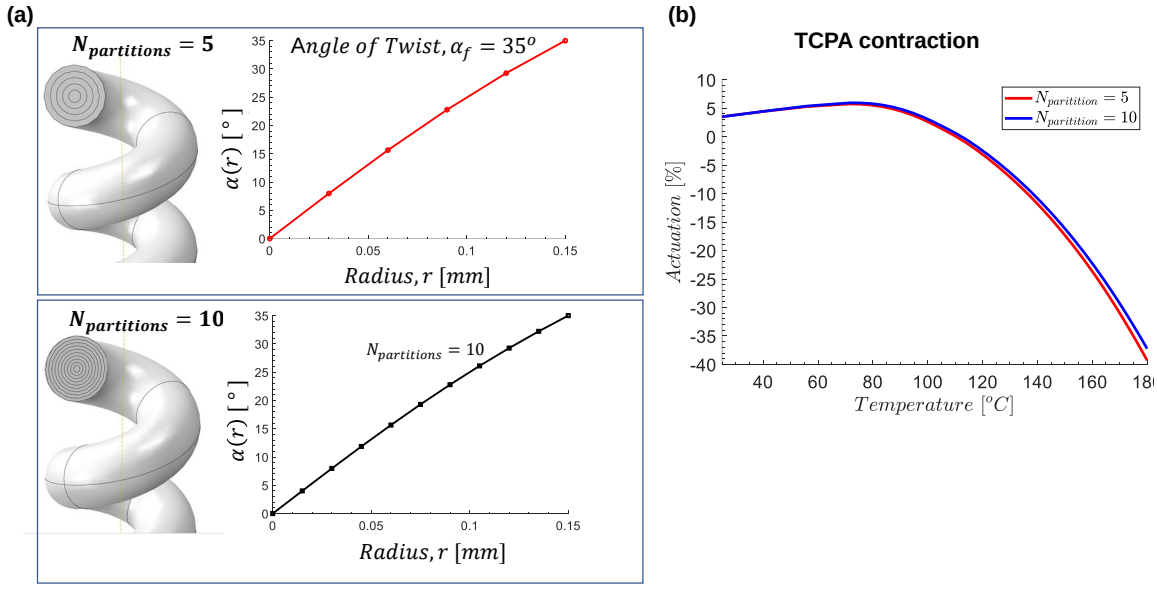

Figure 4.15: (a) Two cases of coil geometry showing the number of concentric partitions, and their respective distribution of orientation as a function of fiber radius and (b) shows the contraction of the TCPA upon heating measured w.r.t its undeformed length

4.3.3 FE Model Validation

The continuum scale model of the TCPA is implemented using the finite element framework. Material properties of the precursor fiber are considered from experimental testing from literature and some data provided by Prof. Sameh Tawfick's research group at UIUC. However, the thermal expansion values are modified based on the actuation response of the TCPA using constant load actuation experimental data. The experimental tests of the coil are conducted by Prof. Sameh Tawfick's research group at UIUC for validation of the FE model. The coil parameters considered for

validation study are shown in Table 4.2, and the meaning of the coil parameters can be referred from Figure 4.7. A small load of value $P = 0.2\ N$ is applied on one end of the coil and the other end is kept fixed in all directions. Five coils with five partitions are modeled in the FE model. The thermal expansion in the radial direction is modified to achieve the response which matches the experimental actuation response the closest. Initially, the coil is kept at 23 ^{o}C and then loaded at this temperature by applying the load P. After the coil deforms under static loading conditions, the temperature is raised to a target value of 122 ^{o}C under static analysis in ABAQUS/-Standard. In this case, the actuation stroke is measured as the percent change in length with respect to the loaded length of the TCPA muscle. Figure 4.16 shows the

Table 4.2: Coil parameters used for validation of the model

Coil parameter	D_{coil}	d_f	p_{coil}	α_f
Value	4.35 mm	1 mm	4.57 mm	31^o

comparison of the model actuation with the experimentally measured values as the TCPA is heated up. The FE model is able to capture the actuation response of the coil and is in close agreement with the experimentally observed response. The thermal expansion coefficient is modified by translating the $\alpha_{22}(T)$ vs. T curve (Figure 4.5(b)) by 15 ^{o}C to the right which results in a reduction in the CTE values. This also implies that the actuation response of the coil is highly sensitive to the value of CTE in the radial direction.

Since this is a highly non-linear problem to model as it includes the creeping of the TCPA as well which we do not model in this work. However, the model captures the initial softening of the TCPA up to 80 ^{o}C, even though experimentally, it shows more softening which might be due to the creep deformation of the muscle. Overall, the agreement of the model with the experiments gives us the confidence to look into parametric studies to understand the actuation mechanisms in further detail.

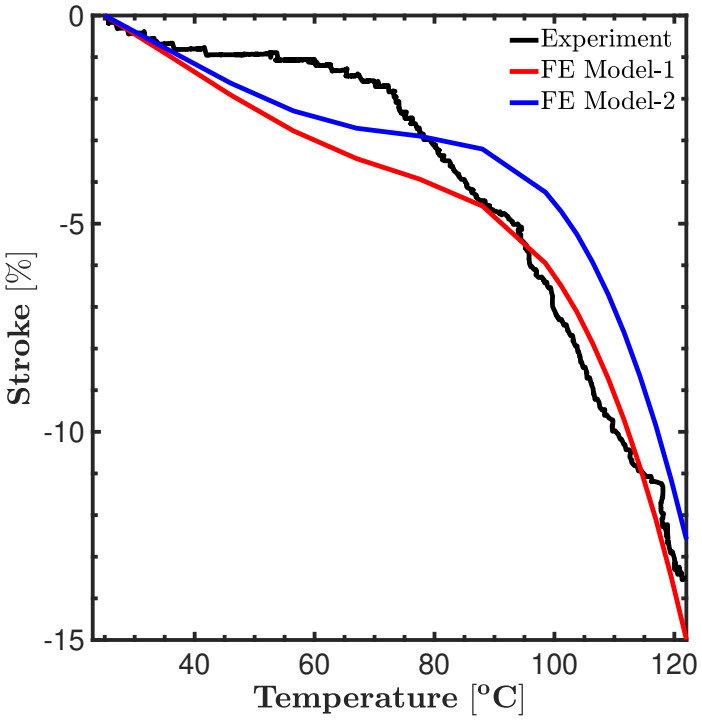

Figure 4.16: The actuation stroke of the TCPA muscle vs. temperature from FE model and its comparison with experimental values (courtesy of Prof. Sameh Tawfick's research group at UIUC), FE model-1 is using the material properties as is and FE model-2 is values modified by shifting $\alpha_{22}(T) = \alpha_{33}(T)$ by 15 ^{o}C

4.3.4 Parameteric Studies of TCPA

4.3.4.1 Influece of twist angle

An important feature the FE model should capture is the extent of the twist on the fiber. The muscle parameters for this model are given in Table 4.1. Figure 4.17 shows that the free actuation response for a homochiral muscle increases as more twist is introduced in it. However, this advantage will start stagnating as we approach more towards $\alpha_f = 90^o$ which is not physically possible. Furthermore, the precursor fiber has to undergo very large permanent deformation in torsional shear mode to attain a high value of twist angle. The high value of twist is introduced such that the precursor fiber doesn't fracture. The case of $\alpha_f = 0$ shows that the muscle is not able to contract, even though small, but, it extends upon heating. This behavior is in line with the experimentally observed effect of angle of twist in literature[31, 167] and in

other computational models[177, 192].

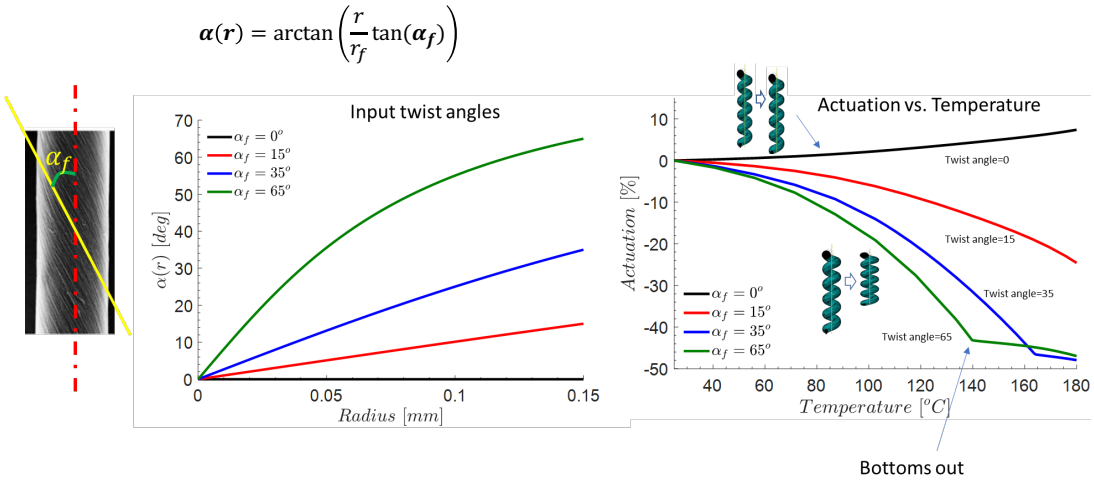

Figure 4.17: The value of angle of twist a function of radius (left), and the resulting free actuation response of the TCPA muscle (right)

4.3.4.2 Influence of material anisotropy

This has been hypothesized that the origin of the large contraction is due to the negative thermal expansion of the fiber axis. In this work, we look at this hypothesis critically and make an attempt to understand what are the key parameters responsible for the large actuation of the TCPA actuators. As we have shown in previous sections the FE model captures the physics of the actuation and is adequate for further investigations. We conduct a parametric study on the influence of material anisotropy. The TCPA coil parameters considered for anisotropy cases are given in Table 4.3. There are two sources of material anisotropy: one in the elasticity tensor, and the second lies in the coefficient of thermal expansion matrix. Therefore, there are primarily four combinations, where we assume isotropy in one of the properties. Table 4.4 shows the four cases for which we look into the TCPA actuation response. The baseline case is Case-4 where both elasticity and CTE matrix has anisotropy. The isotropic elasticity case is assumed to have the modulus along the fiber direction with Poisson's ratio of 0.33. The fiber axis CTE is assumed for the case of the isotropic CTE matrix. Both

material properties are assumed to have temperature dependence as in their original values.

Table 4.3: Coil parameters used for FE model studies of material anisotropy

Coil parameter	D_{coil}	d_f	p_{coil}	α_f
Value	3.37 mm	1.0 mm	1.55 mm	42^o

Table 4.4: Key cases considered for the influence of material anisotropy

Case	Elasticity tensor	CTE matrix
1	Isotropic	Isotropic
2	Isotropic	Transversely-Isotropic
3	Transversely-Isotropic	Isotropic
4	Transversely-Isotropic	Transversely-Isotropic

Figure 4.18 shows the actuation response for the four cases of material anisotropy in the fiber. The case of anisotropy in CTE matrix shows the contraction despite the anisotropy in the elasticity. Case-2 and Case-4 are very close to each other, just shifted by the initial loaded state whereas Case-4 shows larger static deformation at room temperature. This is due to the fact that the isotropic elasticity tensor shows higher stiffness along the fiber axis as the angle of twist doesn't reduce the effective axial stiffness. The case where both properties are isotropic is basically the case of a TCPA muscle fabricated using an isotropic material with negative CTE. Such a fiber does not show any contraction, instead, it extends upon heating as a result of the elastic modulus softening. These four cases provide an insight into the key features a precursor fiber should have to fabricate the TCPA muscle for large actuation. Overall, anisotropy in CTE is responsible for the actuation irrespective of the type of material symmetry in the stiffness tensor.

4.4 Conclusions

In this work, we conducted multi-scale computational studies of the semi-crystalline polymer-based twisted and coiled polymer actuators (TCPA). At the nano-scale, the

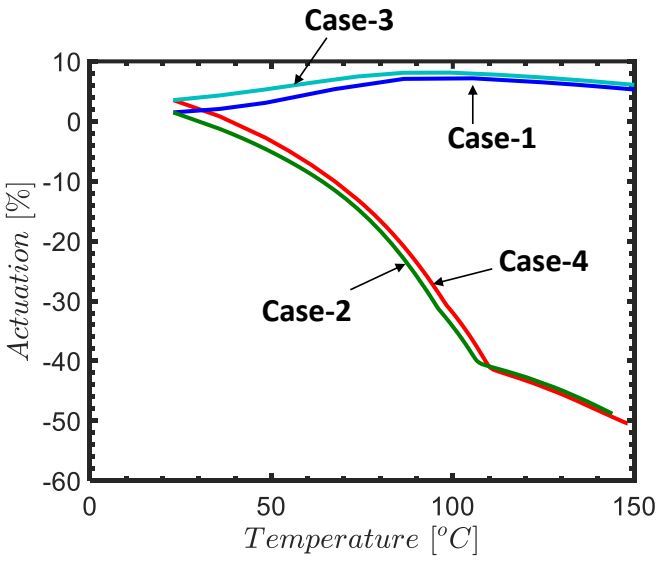

Figure 4.18: Actuation response of a TCPA muscle with material anisotropy in elastic tensor or thermal expansion (CTE) matrix

two phases of Nylon 6,6 are investigated for their thermal behavior. At the continuum scale, a finite element model is developed for the TCPA and used to understand the fundamental factors responsible for the large actuation stroke of these actuators. The following conclusions are drawn:

- All-atom molecular dynamics (MD) simulation models are developed for pure amorphous and pure crystalline phases of Nylon 6,6 semi-crystalline polymer to look into their thermal behavior.

- The coefficient of thermal expansion (CTE) of the amorphous phase is positive and non-linear function of temperature. The glass-transition temperature value predicted by the MD model is in good agreement with that observed experimentally in the literature.

- The thermal response of the pure $\alpha - triclinic$ phase of the crystalline Nylon show that the crystal has a negative CTE along its longest dimension or the along the covalently bonded chains. This is responsible for the negative CTE of the highly drawn precursor fibers that are used for TCPA.

- A continuum-scale model is developed that captures the physics of the actuation. The model is validated and found to be reasonably accurate and adequate to capture different aspects of the TCPAs such as chirality of the coil, angle of twist, etc.

- The objective of the study was to look into the key factors responsible for the large actuation of the TCPA muscle. The insights from this study include that the anisotropy in the CTE matrix plays a major role as compared to that in the elasticity tensor of the material.

- This framework opens the scope to investigate new types of material candidates and explore the design space to optimize the performance of actuators that derives their actuation response from nano-scale and micro-scale structures.

CHAPTER V

Understanding Additive manufacturing using Molecular Dynamics

Additive manufacturing of a single crystalline metallic column at nanoscale is studied using molecular dynamics simulations. In the model, a melt pool is incrementally added and cooled to a target temperature under isobaric conditions to build a metallic column from the bottom up. The polyhedral template matching (PTM) is used to observe the evolution of atomic-scale defects during this process. The solidification is seen to proceed in two directions for an added molten layer. The molten layer in contact with the cooler lattice has a fast solidification front that competes with the slower solidification front that starts from the top of the melt layer. The defect structure formed strongly depends on the speed of the two competing solidification fronts. Up to a critical layer thickness, the defect-free single crystals are obtained as the faster solidification front reaches the top of the melt pool before the initiation of the slower front from the top. A slower cooling rate leads to a reduction in defects, however, the benefits diminish below a critical rate. The defect content can be significantly reduced by raising the temperature of the powder bed to a critical temperature. This temperature is governed by two competing mechanisms: the slower cooling rates at higher temperatures and the increase in amorphousness as one gets closer to the melting point of the metal. Finally, the effect of an added soft inclusion (SiS) and a

hard inclusion (SiC) on the defect structures is explored. The hard inclusion leads to a retained defect structure while soft inclusions reduce defective content compared to pure metal.

5.1 Background

Molecular dynamics simulations can capture the non–equilibrium physics by efficiently representing the inter-atomic interactions during solidification using the well-calibrated interatomic potentials. Although only small volumes (nanoscale) can be simulated, such simulations have allowed the prediction of bulk phenomena in the past including the understanding of metal curves [193, 194], nucleation and grain growth [195], solidification defects [196, 197], and the vacancy formation during solidification [198]. Kurian et al. [199] recently employed large–scale molecular dynamics simulations to study the melt behavior and its interaction with nano-powdered particles and subsequent solidification. This study showed the process of crystal nucleation in the melt and the emergence of grain boundaries as well as voids during the process. Another study by Jiang et al. [200] employed molecular dynamics simulations to understand the crystallization and cluster evolution patterns for various laser powers and scan rates in $Fe_{50}Ni_{50}$ amorphous alloy. These investigations demonstrated that the low scanning speeds allow increased crystallization into body-centered cubic (BCC) structures. Furthermore, the low energy density of the laser diminishes crystallization and leads to a more amorphous structure [200]. However, a detailed account of atomic–scale defects as a function of process parameters was not performed in these studies, and this is the goal of the current work.

During the solidification of grains, various defect structures form that are either unstable (e.g. self–interstitial) which are relieved during reheating, or more stable defect structures (e.g. high angle grain boundaries) that persist after the process. Understanding the formation of defects as a function of parameters such as cooling rates,

particle bed temperature, presence of inclusions, etc. has not yet been carried out via molecular simulations. Hu et al. have experimentally studied the effect of cooling rates on the microstructural characteristics in a MAM process [201] and found that fast cooling rates result in small grain size and at the slower cooling rates, large grain structures were observed. There have also been experimental investigations on the effect of layer thickness by Sui et al. [202], and on the influence of substrate temperature (preheated bed) [203] on the microstructure evolution and its mechanical performance [39]. By increasing the substrate temperature to 1000 ^{o}C, mitigation in the extent of the microcrack density was observed in Tungsten as compared to preheated bed at 200 ^{o}C. In this study, we analyze the effect of such process parameters by idealizing an additive column at the nanoscale using molecular dynamics (MD) as shown in Figure 1.5 (right). Fundamental reasons for these effects are analyzed and interpreted at the atomistic scale.

In this work, we model the melting and cooling of successive layers of the material. The simulations idealize the process at nanoscale and the metallic column simulated in this work, in the context of nanoscale additive process (shown in Fig.1.5(right)). Because of the length and time scale limitations of molecular dynamics, we consider this approach as geared towards investigating defect mechanisms in a corresponding 3D printed nanoscale material rather than conventional metal additive manufacturing. Additionally, the simulation set–up is specific to capturing layer-to-layer interactions, rather than track–to–track interactions (seen in Figure 1.5(left)) across meltpools. To simulate this process, we first obtain the equilibrated density of the liquid metal at a temperature above the melting point. A liquid melt of this density is then poured onto a solidified substrate in a layer–by–layer fashion along the build direction (we choose $< 001 >$ for both Cu and Al systems) followed by cooling down the system to a target temperature. The study primarily aims to understand the defect structure and its origin as a function of several process variables such as cooling rates, layer

thickness, and bed temperature from an atomistic viewpoint. Section 5.3 presents a detailed discussion of the phenomena that leads to the differentiation of single crystals into dislocation defects or amorphous regions as a function of these process variables. In the latter part of the section, we simulate the effect of inclusions in the melt on the resulting defect structure. Section 5.4 presents the key conclusions drawn from this study.

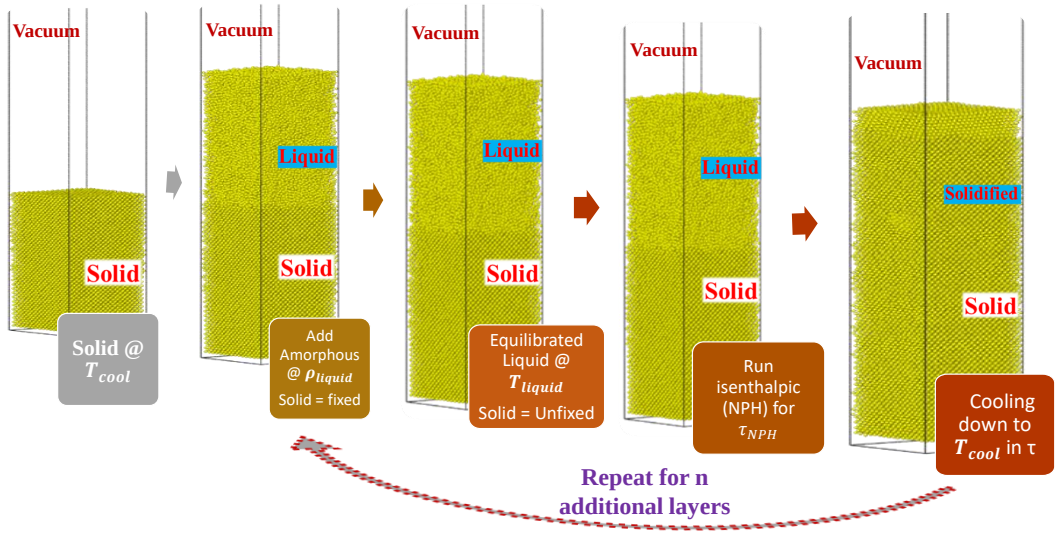

Figure 5.1: Steps for molecular dynamics simulation of the additive manufacturing process.

5.2 Methods

All MD simulations are performed using the large-scale atomic/molecular massively parallel simulator (LAMMPS) [157]. A supercell of copper of user–specified dimensions is generated as the basis for an initial solid seed region with periodicity in all directions. The supercell is initially equilibrated to a target bed temperature (T_{cool}) using NPT simulation that employed an Andersen barostat [204] at atmospheric pressure and a Nosé-Hoover (NH) thermostat [205]. The Andersen barostat only allows

isotropic changes to the unit cell and ensures that the FCC lattice has the correct equilibrium volume at room temperature. To estimate the density of the liquid (ρ_{liquid}) at the melting temperature, this cell is heated to T_{liquid} using another NPT simulation. The liquid cell density is noted and subsequently used while adding liquid layers during the additive process.

During the deposition simulation, the following process is followed (shown in Figure 5.1). The equilibrated supercell (at T_{cool}) of a known thickness (t) is initialized at a target temperature (T_{cool}) and a vacuum layer is created on top. At each deposition stage, the same volume as the solid supercell is amorphously packed at the top of the solid column at the liquid density ρ_{liquid} estimated previously. The solid atoms are then fixed and an NVT simulation is used to equilibrate the liquid layer to the melt temperature (T_{liquid}) using velocity re-scaling. The solid atoms are then unfixed and the system is run under constant enthalpic (NPH) step to simulate interaction of the molten layer with the substrate allowing remelting of the substrate layers. This step is performed for a duration of $\tau_{NPH} = 5$ ps within which the isenthalpic interaction leads to remelting in the substrate layers without any solidification. This is followed by a cool–down starting from the equilibrated velocities using the NH thermostat and an Andersen barostat at atmospheric pressure. Along the build direction, a vacuum region is maintained to avoid self–interactions along the build axis. The entire cell is cooled back to a set temperature (T_{cool}) over a specified time (τ). Once cooled back to T_{cool}, the melt layer equilibrates approximately to a layer thickness (t) accounting for contraction during cooling. In the next deposition stage (for the second melt pool), the process is repeated by amorphously packing another liquid layer at the top of the newly solidified structure at the known liquid density ρ_{liquid} and repeating the cooling steps detailed above.

The layer thickness and cooling time can be controlled in the simulation. Higher substrate temperatures (use of preheated beds) can be simulated by changing the

equilibration temperatures set for the thermostat. For an exhaustive account, the effect of the following parameters are investigated in this work:

- Cooling time (τ) of each deposited layer
- Thickness of deposited layers (t)
- Target cooling temperature (T_{cool}) of each deposited layer
- Influence of a soft (SiS_2) and hard (SiC) inclusion in each deposited layer

The structure type in the simulation box is identified by performing the polyhedral template matching (PTM) [206] in Ovito [207, 208], an open–source visualization tool. PTM is preferred over conventional common neighbor analysis (CNA) [209] due to its ability to classify the atomic configurations even at elevated temperatures near the melting point. The root mean square (RMS) error cutoff of 0.14 is used for the PTM analysis. Since FCC metals are chosen in this study, we refer to the FCC content in the lattice as the defect–free content for the additive column. In the perfect FCC crystal lattice, three equivalent close-packed planes are aligned along the $< 111 >$ direction, which leads to an atomic stacking sequence of the form ABCABCABC. A typical defect is the formation of a stacking fault, which occurs when the stacking sequence changes through removal or misalignment of one of the layers in the form ABCABABC. Such regions are identified to be of hexagonal close-packed (HCP) form in the software. The higher energy crystal structures of the body centered cubic (BCC) form are also identified. The clusters that do not fall under the classification of cubic or hexagonal crystals are termed 'amorphous' and may contain defects such as grain boundary dislocations, shockley partials, vacancies, and self–interstitial in addition to disordered clusters. The actual nature of these amorphous defects is obtained through observation. These clusters are identified at the end of the cooling time for each layer. After an i^{th} layer is added to the additive column, the percentage of each structure is computed at layer number L_i using the following equation:

$$\%FCC^i = \frac{N^i_{FCC}}{N^i_{total}} \times 100; \%Amorphous^i = \frac{N^i_{Amorphous}}{N^i_{total}} \times 100 \tag{5.1}$$

where, we refer to $i = 0$ as the initial solid crystal and for $i = 1$ as the first liquid layer (L_1) added and so on. N^i_{FCC}, $N^i_{Amorphous}$ and N^i_{total} are the number of FCC atoms, amorphous atoms and total number of atoms after the i^{th} layer is added to the additive column, respectively.

5.3 Results and Discussion

The molecular dynamics simulations in these examples are carried out for face-centered cubic (FCC) copper (melting point of 1358 K) using an embedded atom model (EAM) potential describing the atomic interactions [54]. The lattice constant of copper is $a = 3.597$ Å at $T_{cool} = 300$ K. The melt is heated to 1500 K and at this temperature, the density is computed as $\rho_{liquid} = 7.8$ gcm^{-3}. Each liquid layer is equilibrated at $T_{liquid} = 1500$ K for 25 ps before adding to the solidified column. The size ($x \times y \times z$) of the initial supercell considered in this case is $16a \times 16a \times 16a$, with the last number indicating the thickness (t) along the build direction (z). Figure 5.2 shows the evolution of FCC content (as given by Eq. 5.1) for each added molten layer during cooling within a time of 50 ps. Eight layers in total are simulated. Initial FCC content is low due to the amorphous nature of the liquid melt but tends to increase as the system solidifies to a crystalline structure at room temperature.

Figure 5.2 shows that the first melt layer solidifies rapidly (within 60 ps) from the defect–free substrate, but locks in around 5% defects. The subsequent layers take more and more time to achieve a stable defect profile. This is related to the decrease in solidification front speeds as the defects in the substrate increase, which is studied later in this section. As molten layer 2 is added and equilibrated, some of the defects in layer 1 are ameliorated (see animation01 in SI). However, the defect volume fraction

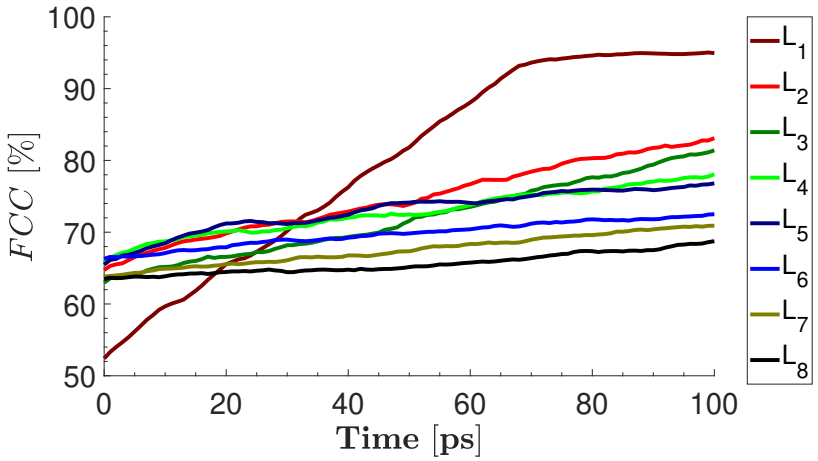

Figure 5.2: Evolution of FCC structure with cooling time for $16a \times 16a \times 32a$ system.

continues to increase from layer 3 onwards due to a lack of sufficient cooling time to eliminate defects. Figure 5.3b shows the temperature profile of a few atomic layers in the solidified part at the interface. The remelting step is very quick and the remelted layers solidify pretty quickly as the heat flows to the solid part under NPH step. There are 2-3 layers that remelt at the interface. It is observed that remelting is uniform for top 2 layers at the interface as can be seen in Figure 5.3a, however, further layers show non-uniform remelting in their cross sections. The temperature profile for atomic layers 3-5 show that it does not reach the melting point of Cu and the temperature is computed as an average for the atomic layer that have some non-melted portion in it.

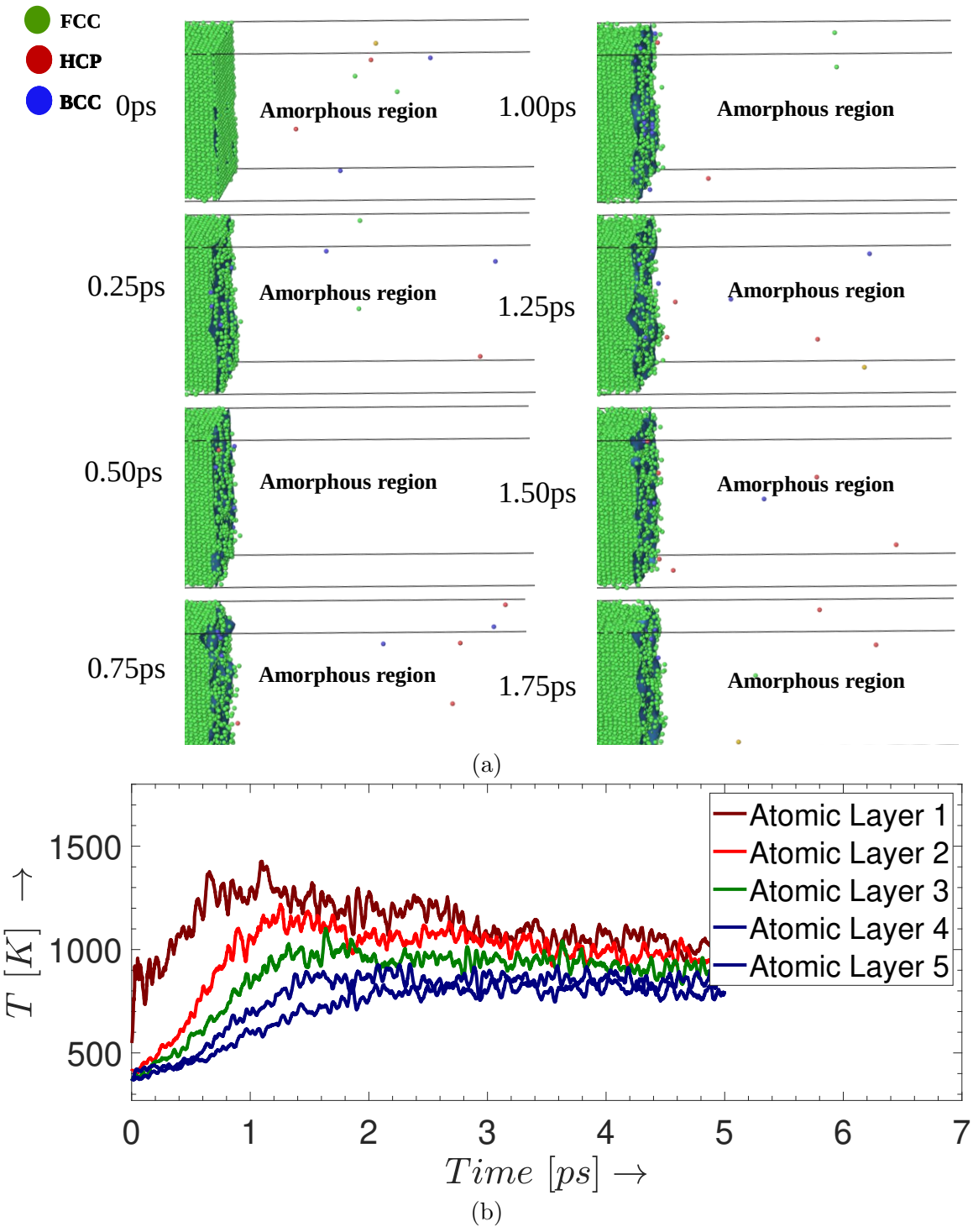

Figure 5.3: Remelting of the interface under constant NPH step (a) and temperature vs. time for top five atomic layers of the solid underneath under constant NPH step

Figure 5.4 presents this effect of cooling time on the defects in detail. For the 50 ps

cooling time detailed previously, the number of defects increases with the number of layers. However, as the cooling time given to the melt is raised to 100 ps, the defect volume fraction significantly reduces with an increase in the number of layers due to sufficient time given for rearrangement and the elimination of higher energy defects. Nevertheless, the slow cooling benefits are lost after 500 ps as the resultant defects are stable and cannot be removed even if the cooling time is increased to 1000 ps (see animation02 for 500 ps case in SI). At 1000 ps cooling time, the percentage of defect–free content converges towards 98% as the number of layers is increased.

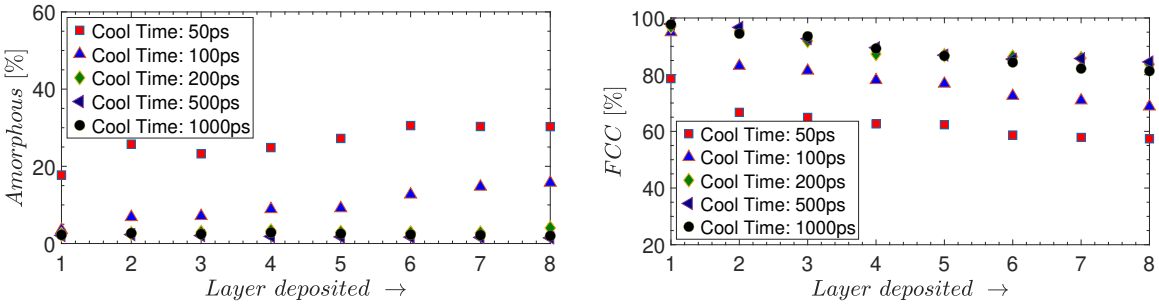

Figure 5.4: Amorphous (a) and FCC (b) structure type evolution as a function of added layers for different cooling times in a $16a \times 16a \times 32a$ system.

5.3.1 Influence of layer thickness on defects

In this parametric study, the thickness of the melt region is increased keeping the orthogonal dimensions fixed. This simulates larger volumes of molten material added at each step, corresponding to higher energy processing, which affects the solidification kinetics in the build direction ($z - axis$). The number of atoms in the initial solid and for the liquid layer for four of the thicknesses studied here is presented in Table 5.1. The system is cooled down to $T_{cool} = 300$ K at a cooling time (τ) of 500 ps for all cases. The thickness in the build direction (z-axis) is varied starting from $10a$ lattice units to $192a$ keeping the transverse dimensions fixed at $16a \times 16a$. The layer thickness, layer-wise number of atoms, and the total number of atoms (at the end of

the eighth layer) for some of the thickness cases are shown in Table 5.1.

Table 5.1: System parameters for different melt layer thickness studies.

System	**Thickness** (nm)	**Atoms-solid**	**Atoms-liquid**	**Maximum atoms**
$16a \times 16a \times 16a$	5.783	16,896	∼14,221	132,088
$16a \times 16a \times 32a$	11.565	33,280	∼28,284	261,663
$16a \times 16a \times 48a$	17.348	49,664	∼42,702	395,008
$16a \times 16a \times 96a$	32.698	98,816	∼86,462	776,986
$16a \times 16a \times 192a$	65.396	197,120	∼172,597	1,554,385

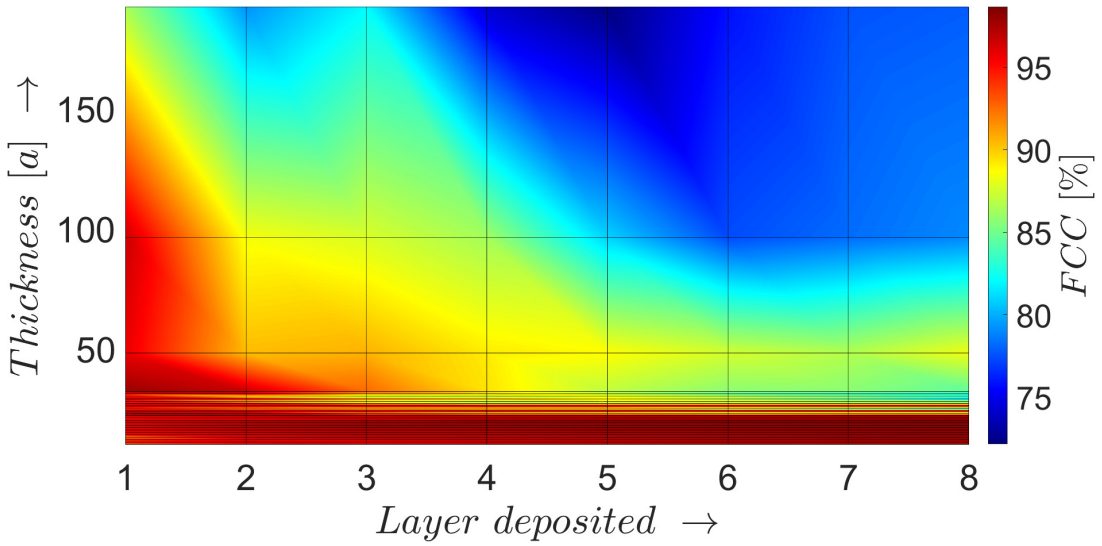

Figure 5.5: Contour plot of FCC percentage as a function of layer thickness and the number of layers.

Figure 5.5 shows the FCC content in the cooled down layers (on the horizontal axis) for different melt thickness (vertical axis). We can see that the FCC fraction is converged at layer 4 to layer 5 for all the thicknesses studied. For lower melt thicknesses, we see single crystal growth with no significant defect structure. However, at higher thicknesses of added layers, a significant amount of defects emerges. A clear threshold thickness beyond which the trend of perfect crystallization changes to a defective structure is seen. For the case of Cu at 500 ps cooling time, this threshold value is estimated to be $24a \pm 2a$ (from 3 replica runs), at and beyond which the defect starts initiating and evolving with additional layers to the additive column.

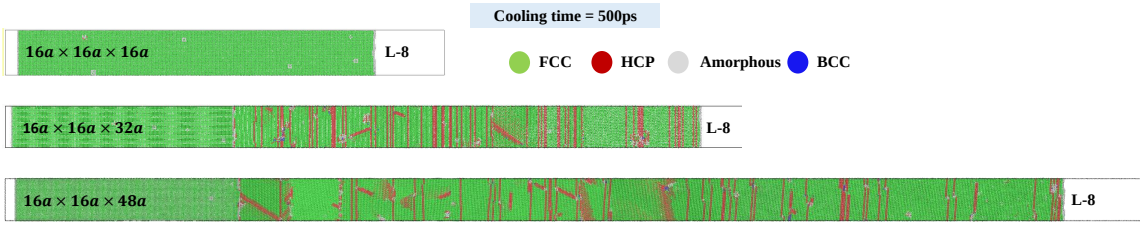

Figure 5.6: Snapshot of the structures produced for three different deposited layer thicknesses at the end of deposition of eight layers.

Figure 5.6 shows the defect structure at the end of the addition of layer number 8 for different thicknesses in the additive column. For the $16a$ thickness case, almost perfect crystallization is seen with a negligible fraction of stable dislocation loops. As the thickness of the molten layer is doubled to $32a$, grain boundaries emerge and a polycrystal structure is seen, delineated by grain boundaries (identified as amorphous/white regions). The first grain contains vertical stacking faults while subsequent grains contain slanted twin boundaries or a combination of stacking faults and twin boundaries. The larger melt thickness simulated ($48a$) also forms larger grains, that initially contain amorphous regions of high dislocation densities, as seen in the last layer (Figure 5.6(bottom)). These regions would subsequently reform during the addition of more layers to form smaller sub–grains. Overall, although different grain sizes are seen for $32a$ and $48a$ cases, the percentage of defects for these two cases are approximately similar.

The results seen here can be interpreted by studying the solidification kinetics in the melt. The solidification is primarily seen to proceed along two directions for an added molten layer as shown in Figure 5.7 for the $96a$ thickness case. The molten layer in contact with the cooler substrate lattice has a fast solidification front that sweeps across the molten layer. The crystal orientation of the substrate is maintained in general. The solidification front at the top, in general, does not have the same crystal orientation as the substrate, and thus, when the two fronts interact, grain boundaries are formed.

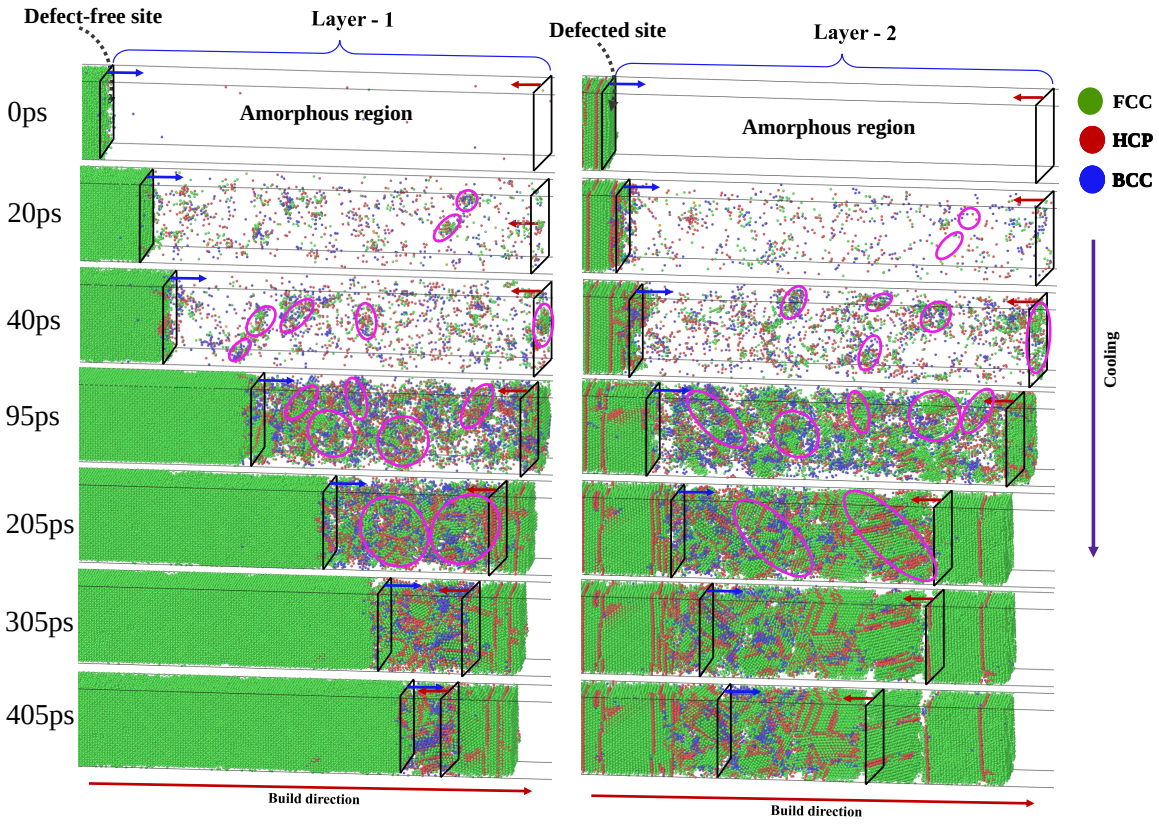

Figure 5.7: Evolution of two solidification fronts demonstrating the cooling mechanism for a 96a thickness case for (left) layer-1 solidification with a perfectly crystalline substrate; and (right) layer-2 which nucleates from the defects left over at the top of layer-1.

For small layer thicknesses, defect–free single crystals are obtained as the faster solidification front reaches the top of the melt pool before the initiation or within the early stages of initiation of the slower front from the top. The critical layer thickness can be analytically found using the speeds of the solidification fronts as follows. The solidification speeds as measured from the case in Figure 5.7 are tabulated in Table 5.2 (refer animation03 and animation04 in SI for layer-1 and layer-2, respectively). The solidification speed from a defect–free substrate is $v = 1.95$ Å/ps. The front speed at the top layer is much lower (0.494 Å/ps). The crystal structure for subsequent layers begins to form stable crystals only after a delay of $\tau \approx 40$ ps compared to the faster front. To identify the threshold thickness for achieving a single crystal, one needs to ensure that the fast solidification front reaches the top before the crystal

Table 5.2: The value of solidification front speed at the bottom and top of the melt pool estimated for $96a$ thickness case.

Solidification front	$F_{bottom}^{crystal}$	F_{bottom}^{defect}	F_{top}^{free}
Solidification front speed [Å/ps]	1.95	0.768	0.494

(with a different orientation) has a chance to fully initiate at the top. This threshold thickness ($t_{critical}$) can be calculated as $t_{critical} = v\tau$ which is about $23a$, the threshold thickness as seen in Figure 5.5 for the formation of defect–free single crystals. Figure 5.6 shows the FCC distribution snapshot at the end of cooling of the 8^{th} layer for $16a$ thickness case which demonstrates a single crystal structure below the threshold.

Increasing the thickness of the melt beyond this critical thickness leads to an increase in the number of defects due to the interaction between two solidification fronts. The presence of defects on the substrate further slows down the primary solidification front. As seen in Figure 5.7, if the substrate contains a large number of defect structures (layer 2 as shown at 0 ps), the solidification front velocity moves at a slower pace (v = 0.768 Å/ps compared to v = 1.95 Å/ps for solidification from a defect–free substrate). However,it is always faster than the solidification front that moves down from the top of the melt. This would mean that the solidification fronts meet roughly mid–way for layer 2 compared to layer 1 as seen in Figure 5.7 and result in a grain boundary. The slower speed of the fronts from defective substrate also implies that it takes more time to achieve stable defect structures as the number of layers increase, a feature previously seen in Figure 5.2.

In addition to the interaction between the two solidification fronts, each front interacts with homogeneous nuclei (shown as pink ellipsoids) formed within the melt as shown in Figure 5.7. These nuclei when absorbed into the two larger solidification fronts leave defect remnants. For smaller thicknesses (e.g. $32a$ case shown in Figure 5.6), these nuclei do not have time to grow as the solidification front rapidly covers the melt. However, the cases with larger thicknesses (e.g. $48a$ case shown in Figure

5.6) have significantly large chunks of amorphous regions as the solidification fronts interact with larger and more differentiated internal nuclei that would take longer to coalesce into the primary crystallized region. These regions have higher interfacial energies that are relieved as the additive process proceeds through the formation of fine sub–grains.

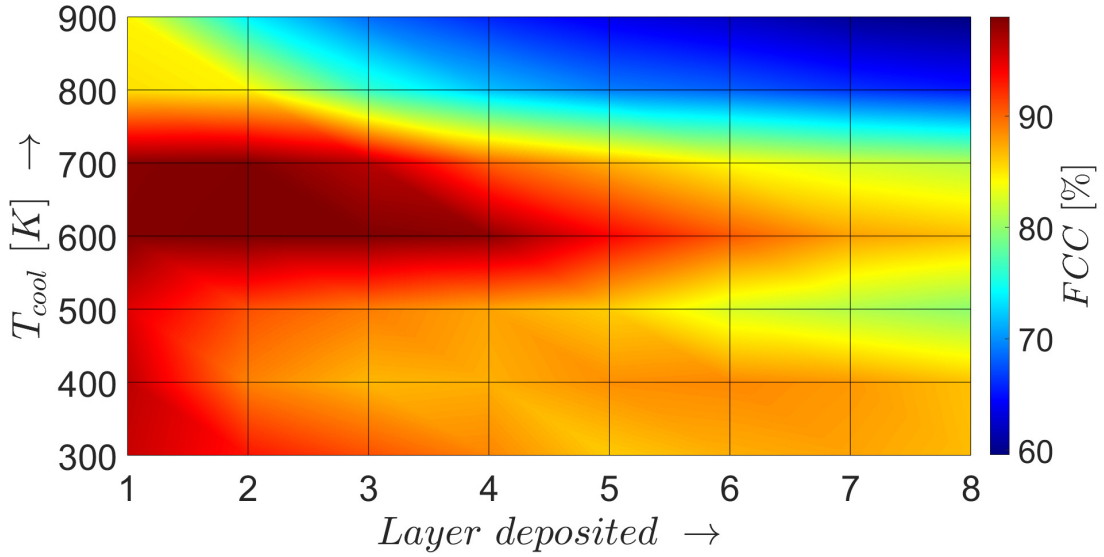

Figure 5.8: FCC structure percentage obtained as a function of bed temperature and the number of layers deposited. A cooling time of 500 ps and a $48a$ layer thickness is used.

5.3.2 Effect of preheated beds

In the study outlined in the previous section, each layer was cooled down to the room temperature $T_{cool} = 300$ K. Experimentally, it is known that preheating the powder beds to higher temperatures leads to fewer defects in the final product. For example, electron beam melted (EBM) parts have lower microcracks compared to selective laser melted (SLM) parts primarily owing to the lower cooling rate due to preheated powder beds and a vacuum chamber that dissipates heat away slower. In the molecular simulations, preheated beds can be simulated by increasing the parameter T_{cool}. For this section, we cool down each layer of the additive column to a

temperature T_{cool} from 300 K to 900 K with an increment of 100 K. A layer thickness of $28a$ and cooling time of 500 ps are chosen for the simulations.

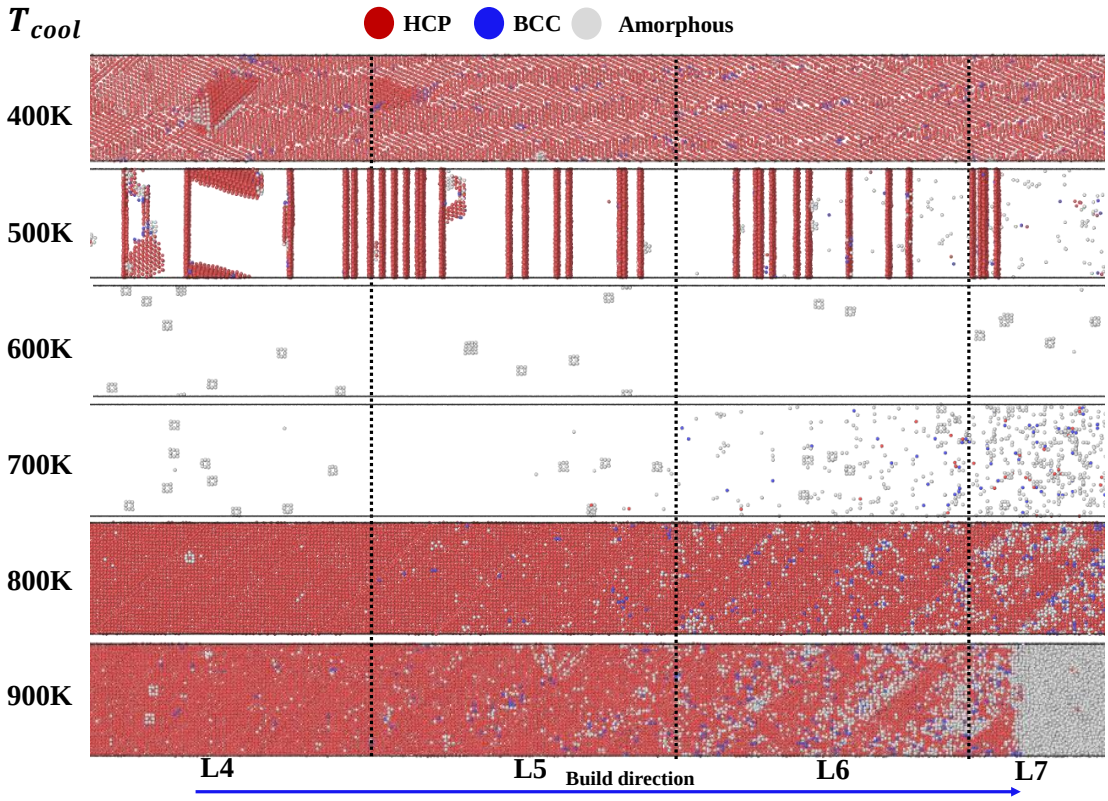

Figure 5.9: Defect structure after cooling to different substrate temperatures (T_{cool}) (only 4 layers, i.e. $L_5 - L_7$ shown).

Figure 5.8 plots the percentage of the FCC content for different layers as a function of T_{cool}. Starting from a higher defect content at 300 K, the defects initially improve as a function of temperature reaching almost a defect–free single crystal at 600 K. As the temperature is further increased, defects again begin to increase significantly with temperature. At higher bed temperatures, the temperature drop per unit time needed is lower for the same time of cooling which implies the slow cooling rates. Slow cooling rates are beneficial to reduce defects as the atoms have more time to rearrange and reduce defects as seen earlier in Figure 5.4. On the contrary, there is an increase in defects beyond 600 K. This unusual behavior can be explained by looking at the defect structures formed at different cooling temperatures.

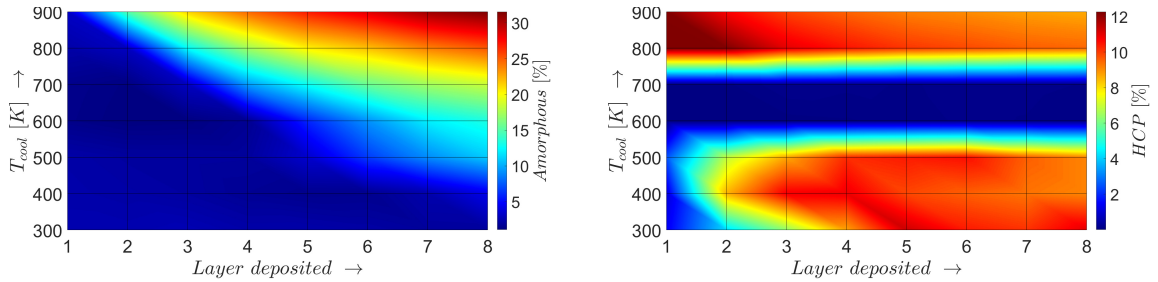

(a) *Amorphous* % (b) *HCP* %

Figure 5.10: Defect evolution in the additive column under different substrate temperatures with an increase in the number of layers depicting (a) percentage of amorphous regions and (b) percentage of HCP regions.

Figure 5.9 shows the defect structure for various temperatures of the bed. Only the defects are shown in this figure (and the FCC structure is hidden). At 400 K and 500 K, most defects are of stacking fault type or grain and twin boundaries. At 600 K and 700 K all these defects are entirely removed. The most amorphous region pertains to the uncrystalized portion remained on the last layer. This is due to the fact that at higher cooling temperatures for this thickness system ($16a \times 16a \times 48a$), 500 ps of cool time is not enough for last layers as the column becomes larger. Therefore, as the temperature is further increased, the amorphous content significantly increases while a content of stacking faults remain similar to that of the lower temperatures. Figure 5.10 shows the split between amorphous and HCP–type defects as a function of bed temperature for different layers. As seen in Figure 5.10(a), the amorphous content begins to increase from 500 K, going toward the melting point of copper. At 900 K, as much as a third of the content is fully amorphous and no benefits of slow cooling rates are seen. Figure 5.10(b) shows that the HCP content increases as the substrate's temperature is decreased below 600 K towards the room temperature. Thus, two mechanisms compete as the bed temperature is raised: (1) the slower cooling rates leading to lower stacking fault type defects and (2) high energy amorphous content as one goes closer to the melting point. The interaction between these mechanisms gives a sweet spot for the temperature of the preheated beds for copper at 600 K.

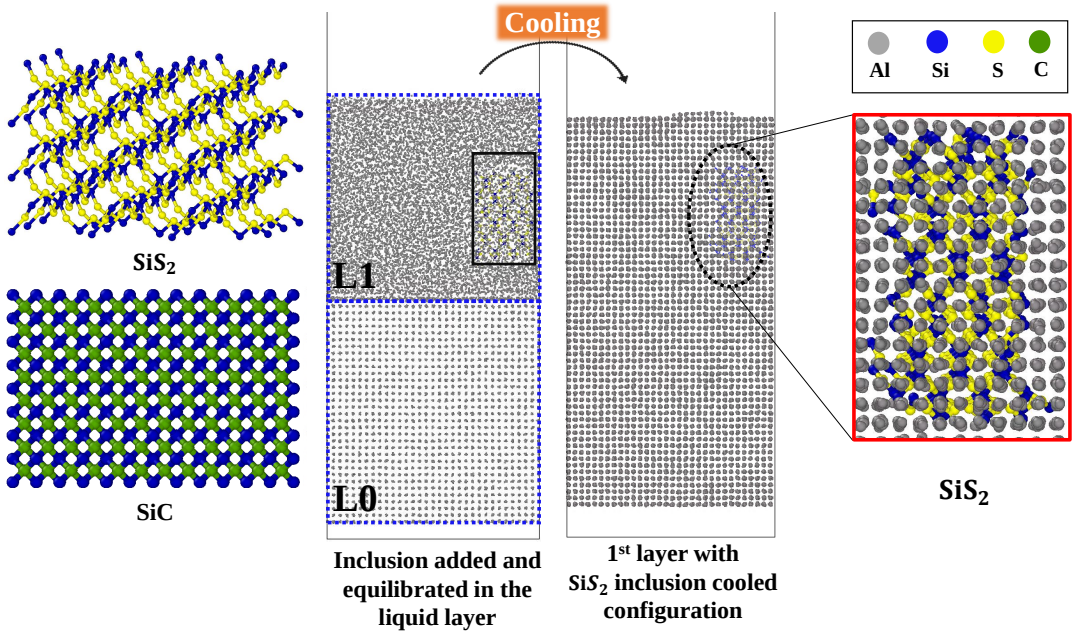

Figure 5.11: (left) Inclusion SiS_2 and SiC (right) SiS_2 as solidified in first layer of Al matrix after cooling down ($V_f = 2.76\%$ for SiS_2 and $V_f = 2.88\%$ for SiC)

5.3.3 Effect of inclusions

In this section, the effect of inclusions on atomistic scale defect evolution is studied. It is known that the use of high temperature stable, soft inclusions lead to improved toughness in the final structure, for example, multi-component oxide, oxy-sulfide or sulfide inclusions in iron welds [210]. Two types of inclusions are chosen in this study: a soft inclusion (silicon disulfide, having a melting point of 1363 K, and elastic modulus of 32 GPa) and a hard inclusion (silicon carbide, with the melting point of 3003 K, and elastic modulus of 323 GPa). To simulate inclusions in the melt, the melting point of the inclusions should be higher than the substrate such that the inclusion is retained in the melt. Because of the higher melting point of copper (1358 K), an Aluminum substrate (melting point of 933 K) was chosen for this example. The structure and density of the constituents are additionally listed in Table 5.3. The consistent valence force field (CVFF) [57] was used for the bonded interactions of SiS_2 and SiC inclusions. Aluminum lattice was modeled using the EAM potential

as described in [54].

Table 5.3: Crystal properties of Al matrix, SiS_2 and SiC inclusions

System	Structure	Elastic Modulus	Melting point	Density at RT
Al [211]	FCC	70.2 GPa	933 K	2.70 gcm^{-3}
SiS_2 [212]	Tetragonal	32 GPa	1363 K	2.20 gcm^{-3}
SiC [212]	Cubic	323 GPa	3003 K	3.17 gcm^{-3}

Leonard-Jones (LJ) potential [57] is used for non-bonded interaction of S-Al interaction for SiS_2 inclusion simulations. Al-SiC systems have been studied with Morse potential for interface fracture [60] and interface properties [61]. The Morse pairwise interactions energy is computed as follows:

$$E = D_o \left[e^{-2\alpha(r-r_o)} - 2e^{-\alpha(r-r_o)} \right] \quad r < r_c \tag{5.2}$$

where, r is the distance between two particles, and the cut-off distance $r_c = 10$ Å. Other parameters for the Al-Si and Al-C non–bonded interactions using Morse potential, were originally obtained by Zhao et al. [3] and are summarized in Table 5.4. The LJ potential is similar in behavior to the Morse potential at the equilibrium distance but deviates as the distance between atoms gets shorter. Morse potential is primarily designed to avoid the singularity of the LJ potential as the interatomic distance goes to zero. This improves the system dynamics in cases where atomic collisions are expected, however, the equilibrium structure is expected to be similar.

Table 5.4: Values of the Morse potential parameters obtained by applying an inverse method to *ab initio* data [3].

Pair	Parameter	Value
Al-Si	D_o	0.4824 eV
	α	1.322 $Å^{-1}$
	r_o	2.92 Å
Al-C	D_o	0.4691 eV
	α	1.738 $Å^{-1}$
	r_o	2.246 Å

First, the equilibrated density of pure Al at 1100 K is obtained by running NPT simulation at 1 bar pressure conditions and the density was observed to stabilize at $\rho_{liquid} = 2.297$ gcm^{-3}. Each layer of this melt density at 1100 K was added to the additive column. To insert the inclusion, atoms in the amorphous layer (with a volume equivalent to the volume and shape of the inclusion) are carved out by deletion from this melt pool layer. The melt with inclusion is again equilibrated at 1100 K at which point Aluminum melts while the inclusion is retained. The same process as explained in the 'methods' section is repeated for modeling sequential addition of the melt. The system is cooled to room temperature with a cooling time of 100 ps. An Al $16a \times 16a \times 16a$ thickness system is chosen for this study and a single inclusion is added at each layer. Fig 5.11 depicts the inclusions SiS_2 and SiC in the first layer of solidified Al melt after cooling down. Volume fractions of the inclusion for the two cases studied are similar with $V_f = 2.76\%$ for SiS_2 and $V_f = 2.88\%$ for SiC inclusion.

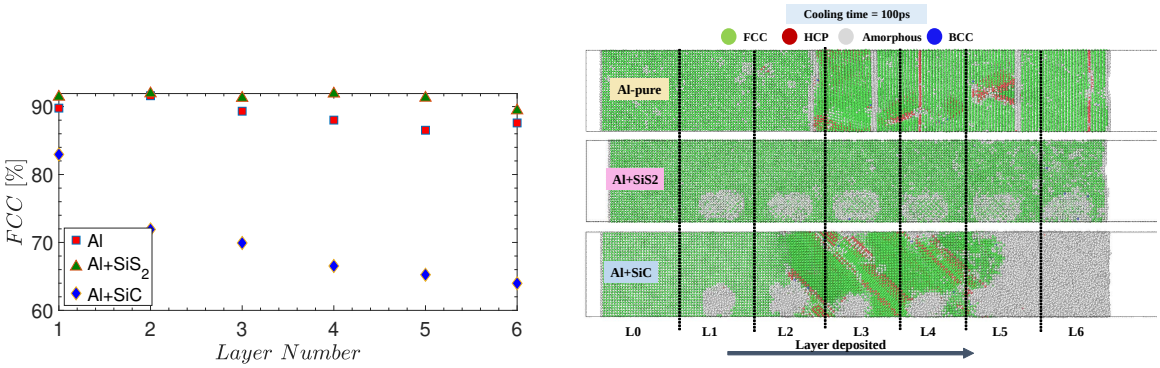

(a) FCC % (b) CNA snapshots

Figure 5.12: (a) FCC percentage evolution as a function of the deposited number of layers for pure Al compared against Al with two inclusions studied here and (b) defect snapshots after deposition of six layers for $16a$ layer thickness.

Figure 5.12a shows the influence of the soft (SiS_2) and the hard (SiC) inclusion on defect evolution as compared to a process with pure Al. The soft inclusion showed the lowest defect percentage and the hard inclusion showed a significant amount of defects. Figure 5.12b depicts the defect structure after the sixth melt layer is cooled. Pure Al forms a polycrystalline structure with grain boundaries (amorphous vertical

regions) under these conditions with a few retained stacking faults. The soft inclusion results in the retention of the single crystal orientation and the stacking faults are eliminated.

Solidification velocities of the pure Al and Al with SiS_2 are found to be similar, showing that the SiS_2 inclusion does not inhibit or enhance solidification front speeds. However, it partially shields interaction between the competing solidification fronts. On the other hand, solidification fronts move much slower in the case of a harder SiC inclusion. In this case, large amorphous regions are formed around the precipitate. This amorphous region is seen at layers 5 and 6 in Figure 5.12b (bottom) but also formed when layers 1 to 4 were added. These regions subsequently reformed into a twinned region emanating from the precipitate (as seen in layers 2-4). Due to the lack of defects, the use of softer inclusions in metal powders is worth pursuing in the future to achieve products with improved fracture properties.

5.4 Conclusions

In this work, we use molecular dynamics simulations to systematically model a nanoscale additive column to investigate the influence of layer thickness, cooling time, target cooling temperature, and alloy inclusions on the final defect structure. Such simulations, although idealizing a very complex additive manufacturing process, can capture the non–equilibrium physics at the nanoscale that leads to the formation of defect structures. It is found that the percentage of the defect–free content of copper converges when a sufficient number of layers are added. The solidification is primarily seen to proceed along two directions for an added molten layer. The molten layer in contact with the cooler lattice has a fast solidification front that competes with the slower solidification front starting from the top of the melt layer. The defect structure formed strongly depends on the interactions between these competing solidification fronts. The key takeaways from these simulations are as follows:

- A lower cooling rate leads to a reduction in defects, however, the benefits diminish below a critical rate as stable dislocation defects form that cannot be further eliminated.

- Up to a critical layer thickness, the defect–free single crystals are obtained as the faster solidification front reaches the top of the melt pool before the stable formation of the slower front from the top.

- As the thickness of the molten layer increases beyond a critical thickness, grain boundaries emerge and a polycrystalline structure is formed. The grain sizes typically increase with the layer thickness. However, for the large melt thicknesses, the amorphous regions of high dislocation densities are formed as the solidification fronts interact with more differentiated homogeneous nuclei. These regions subsequently reform to create smaller sub–grains.

- The defect content can be significantly reduced by raising the temperature of the powder bed to a critical temperature. At low bed temperatures, the faster cooling rates lead to significant dislocation defects. At higher temperatures, the cooling rates are lower leading to a lower dislocation content. However, higher temperatures also lead to an increase in amorphous content. There is a critical value of temperature that balances both the dislocation defects and the amorphous content.

- Finally, the effect of added soft inclusion (SiS_2) and a hard inclusion (SiC) on the defect structure in Aluminum is studied. SiC inclusion significantly slows down the solidification front leading to retained defect structure. However, the addition of SiS_2 does not modify the solidification velocity compared to pure Al. Additionally, the presence of SiS_2 is seen to reduce defect content compared to the pure metal.

The presented results are an initial step towards a computational understanding of the additive process parameter–crystal structure relationship in a non–equilibrium setting. This study can be improved by considering the effect of actual laser heating profiles, surface cooling in a non–vacuum environment, and the interaction of melt pools. The methodology can also be used to model the evolution of residual stresses in the unit cell as a function of process parameters and simulate the stress–strain response after processing. A critical advantage of a first principle approach is that the simulations can be used to perform alloy design, as the preliminary inclusion case presented here, but with improved modeling of formation and dispersion of multiple inclusions.

CHAPTER VI

Conclusions and Future Work

6.1 Summary

In this thesis, we employed molecular dynamics (MD) simulations to investigate the structure, dynamics, and properties of three distinct material classes: vitrimers, semicrystalline polymers, and metals. By leveraging MD simulations, which offer valuable insights when experimental data is limited, we aimed to uncover underlying mechanisms and predict macroscopic responses in these materials.

Vitrimers, designed to address the non-recyclability of thermoset plastics, feature dynamic cross-links that impart malleability under thermal stimuli. However, a lack of understanding regarding their mechanical behavior has hindered their aerospace applications. Our research utilized MD simulations to gain insights into the thermomechanical response of vitrimers. We developed a novel capability to simulate dynamic cross-linking reactions under various thermomechanical loading conditions using a topological reaction scheme. Additionally, we demonstrated the molecular-level healing of damaged vitrimer systems. The outcomes of this work enable the development of innovative computational techniques to model the intricate interplay between chemistry and mechanics in vitrimers, establish links between the evolution of thermomechanical properties and molecular mechanisms, and deepen our understanding of the molecular-scale creep behavior of vitrimers, which is challenging to

characterize experimentally.

Another focus of our research was the simulation of twisted and coiled polymer actuators (TCPA) based on semicrystalline polymers. TCPAs leverage the thermal expansion mismatch between their amorphous and crystalline phases, enabling significant actuation strokes. Through all-atom MD simulations, we explored the thermal behavior of these phases, determining their coefficients of thermal expansion (CTE) and glass-transition temperature. Leveraging this data, we developed a finite element model for TCPAs and validated it against experimental results. The model allowed us to investigate the effects of parameters such as chirality, twist angle, and anisotropy on actuation performance. We found that the CTE mismatch played a dominant role in achieving large actuation, while the elasticity tensor had a minor influence. This comprehensive study enhances our understanding of the underlying physics of TCPAs and presents avenues for optimizing their design and performance.

Lastly, we examined the additive manufacturing (AM) of metal parts, a process involving the gradual modification of solids through the addition of new material layers. Specifically, we focused on thermally-enabled metal additive manufacturing (MAM), which involves rapid heating of powder beds, generating large thermal gradients, followed by high cooling rates of small material volumes. Nanoscale atomistic simulations were employed to model the MAM process and establish correlations between process parameters and material properties. We observed that raising the temperature of the powder bed to a critical level significantly reduced defect content. Furthermore, we demonstrated the capability of our simulations to perform alloy design, exemplified by the study of the effect of adding hard and soft inclusions on defect structure.

6.2 Future work directions

This thesis showcases the power of MD simulations in investigating the intricate behavior of materials. Our findings contribute to the development of computational techniques for modeling the complex interplay between chemistry and mechanics in vitrimers, elucidate the molecular mechanisms underlying the thermomechanical response of materials, enhance our understanding of TCPAs and their optimization, and provide valuable insights into the additive manufacturing of metal parts. Ultimately, the goal of such simulations is to provide physics based principles to guide design optimization of materials [213, 214, 215].

6.2.1 Vitrimers

While this thesis has made significant strides in understanding the behavior of vitrimers, there are several exciting avenues for further exploration. One important aspect to investigate is the effect of surface morphology on the healing process. Specifically, it would be valuable to study how notches or cracks in vitrimer materials can heal under thermal loads (shown in Figure 6.1). Initial simulations have shown promising results, revealing crack tip blunting as a healing mechanism. By conducting more in-depth simulations, we can gain insights into the dynamics and mechanisms involved in the healing process and quantify the extent to which different surface features affect healing efficiency.

Furthermore, an intriguing area of future research involves explicitly simulating the effects of catalysts on the healing behavior of vitrimers. Catalysts play a crucial role in promoting cross-linking reactions and enhancing healing capabilities. By incorporating catalysts into our MD simulations [216], we can examine their influence on the healing kinetics and assess their effectiveness in facilitating the restoration of mechanical properties in damaged vitrimer systems.

Additionally, the effects of additives that can prevent creep in vitrimers present an

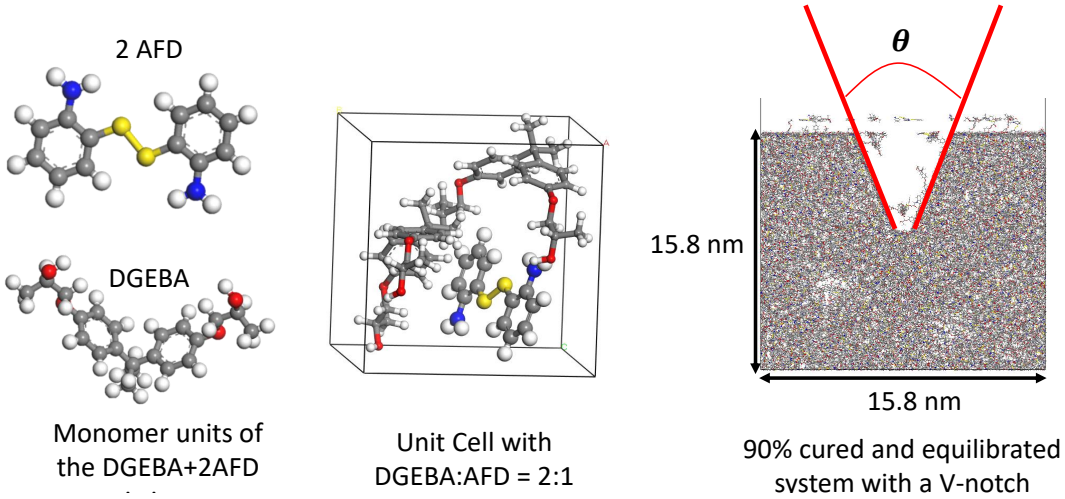

Figure 6.1: Vitrimer monomers structures (DGEBA+2AFD) and its repeated unit-cell, and a V-notch system prepared to probe into its healing behavior

interesting avenue for future investigation. MD simulations provide a powerful tool to explore the impact of different additives on the creep behavior of vitrimer materials. By systematically introducing various additives and characterizing their interactions at the molecular level, we can gain insights into the mechanisms through which they hinder creep and potentially identify novel additives with enhanced creep resistance. Another intriguing approach to prevent creep in vitrimers is the incorporation of permanent bonds within the material structure. By introducing a certain level of permanent bonding, we can explore how it influences the mechanical behavior and creep resistance of vitrimers. MD simulations offer a means to investigate the molecular-scale effects of permanent bonds and determine their optimal concentration and distribution within the material to achieve the desired mechanical properties.

6.2.2 Semi–Crystalline Polymers

In this thesis, we have developed a computational model for twisted and coiled polymer actuators (TCPAs) that can capture their nonlinear thermo-mechanical behavior and predict their actuation performance under various loading conditions. The model can also be used to optimize the design parameters of TCPAs and explore their po-

tential applications in smart materials, soft robotics, and artificial muscles. However, there are still some limitations and challenges that need to be addressed in future work.

One area of interest is simulating the drawing process of fibers and studying the behavior of the coefficient of thermal expansion (CTE) using molecular dynamics (MD) simulations. By capturing the intricate molecular-level interactions and structural changes during the drawing process, MD simulations can offer valuable insights into the resulting mechanical and thermal properties of the fibers. Investigating the CTE behavior of these fibers would provide crucial information for applications where dimensional stability is critical. By correlating the molecular-level dynamics with macroscopic properties, it becomes possible to optimize the drawing process and tailor the fibers' thermal response to specific requirements.

Another important direction for future research involves understanding the elastic properties of multiphase semicrystalline polymers. In the present thesis, each phase was modeled separately, focusing on their individual thermal behaviors. However, the interactions between the crystalline and amorphous phases can significantly impact the overall mechanical properties. To capture these effects, a combined nano-scale structure can be constructed, considering the influence of the two phases on each other's thermomechanical behavior. For instance, the extent of the crystalline phase can influence the glass-transition behavior of the amorphous phase. By developing a more detailed all-atom model that incorporates the interactions between phases, it becomes possible to establish a comprehensive structure-properties relationship, enabling the tailoring of the drawing process of precursor fibers to achieve desired property metrics.

Moreover, it would be beneficial to explore the impact of processing conditions on the formation and arrangement of crystalline domains in semicrystalline polymers. By systematically varying the processing parameters, such as cooling rate, pressure, and

annealing conditions, it becomes possible to investigate the resulting microstructure and its influence on the material's mechanical and thermal properties. MD simulations can provide insights into the molecular-scale mechanisms governing the formation of crystalline domains and their organization, leading to a better understanding of structure-property relationships and guiding the optimization of processing conditions for desired material properties.

Furthermore, the incorporation of more complex and realistic models, such as non-equilibrium or non-linear approaches, can offer deeper insights into the behavior of semicrystalline polymers under various loading conditions. These advanced models can capture the non-linear stress-strain behavior, time-dependent responses, and large deformation characteristics of the material, allowing for a more accurate representation of its mechanical properties. Additionally, the current model can be coupled with an electro-thermal heating model in a finite element framework to simulate the actuation behavior in multi-physics settings in ABAQUS/CAE.

6.2.3 Metal additive manufacturing

The results presented in this thesis represent an initial step towards comprehending the relationship between additive process parameters and crystal structure in a non-equilibrium setting. However, there are several avenues for further improvement and exploration. One area that warrants further investigation is the consideration of actual laser heating profiles during the additive manufacturing process [217]. The current study assumes idealized heating conditions, but in reality, the laser heat source may exhibit non-uniform profiles. Incorporating realistic laser heating profiles into the simulations would provide a more accurate representation of the thermal gradients and temperature distribution, allowing for a better understanding of their impact on the material's microstructure and mechanical properties.

Additionally, the influence of surface cooling in a non-vacuum environment is an essential aspect to consider. During additive manufacturing, rapid cooling of the material occurs due to heat dissipation to the surrounding environment. By incorporating the effects of surface cooling into the simulations, we can gain insights into the resulting microstructural evolution and potentially identify strategies to optimize cooling conditions for improved material properties. Another important direction for future research involves the interaction of melt pools during the additive manufacturing process. In a multi-layered deposition, successive melt pools can influence each other, affecting the final microstructure and mechanical properties [218, 219]. Investigating the interaction of melt pools through advanced simulation techniques would provide valuable insights into the thermal history and solidification behavior of the material, leading to a more accurate representation of the additive manufacturing process.

The methodology presented in this thesis can be extended to model the evolution of residual stresses in the unit cell as a function of process parameters. Residual stresses can significantly influence the material's mechanical behavior and stability. By simulating the development of residual stresses and their distribution within the material, we can gain insights into their origins and devise strategies to mitigate their detrimental effects. The deformation response in polycrystalline state is dominated by mechanisms such as slip, twin [220, 221, 222] and their interactions with grain boundaries [223, 224], and associated size effects [225, 226]. To better understand the role of processing on the mechanical behavior, MD simulations of the simulated volumes can be performed to provide valuable information to deformation models at higher length scales [227]. By subjecting the simulated material to various mechanical tests, such as tensile or compression tests [228], we can analyze its stress-strain behavior and validate the computational predictions against experimental data.

In terms of alloy design, the preliminary inclusion case presented in this thesis can be expanded to include improved modeling of the formation and dispersion of multiple inclusions and their role on mechanical response [229]. This would enable more comprehensive investigations into the effects of various inclusion types, sizes, and distributions on the material's defect structure, mechanical properties, and performance. To further enhance the accuracy of simulations, the actual effect of the laser on the melting process should be considered. This involves simulating laser-matter interactions using ab-initio molecular dynamics (MD) simulations. Figure 6.2 shows a schematic of the laser-matter interaction model, and by employing ab-initio MD, we can study the laser absorptivity of different materials, which is a crucial property for computational simulations at the macroscale. We have conducted some of preliminary studies where we looked at the absorptivity spectra of pure metals and alloys. Lastly, the use of advanced simulation techniques, such as tight-binding density functional theory (DFT) or machine-learned potentials [230], holds promise for simulating more complex materials, including high entropy alloys. Exploring these techniques would allow for a deeper understanding of the behavior and properties of such materials under additive manufacturing conditions.

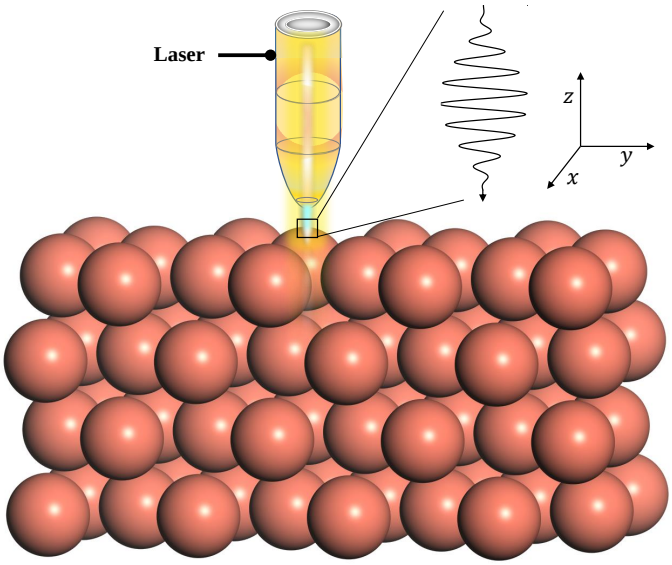

Figure 6.2: Schematic of a laser-matter interaction where the laser is modeled as an electromagnetic field pulse interacting with the electrons in the lattice

APPENDIX

APPENDIX A

Vitrimer Model with dynamics reactions capability

A.1 Reactions in MD simulations

Figure A.1 shows the schematic of a cutoff and probability-based algorithm which identifies a reaction site based on a user input template and modifies the bonding and neighboring atoms as per user specification. The bonding can have two bonding atoms only in one reaction, but the user can add any number of reactions.

A.2 Curing of Vitrimer

The vitrimer simulation box is filled with THE monomer mixture and then the curing of the system is performed using *bond/react* algorithm in LAMMPS[76, 77]. The epoxide ring opening reaction is not modeled, instead an open ring with a hydroxy group attached in the DGEBA unit is modeled direction for the curing process. To carry out the polymerization, the primary and secondary amine reactions are modeled. The pre and post reaction template for the primary and secondary reactions are shown in Figure A.2(a) and A.2(b), respectively.

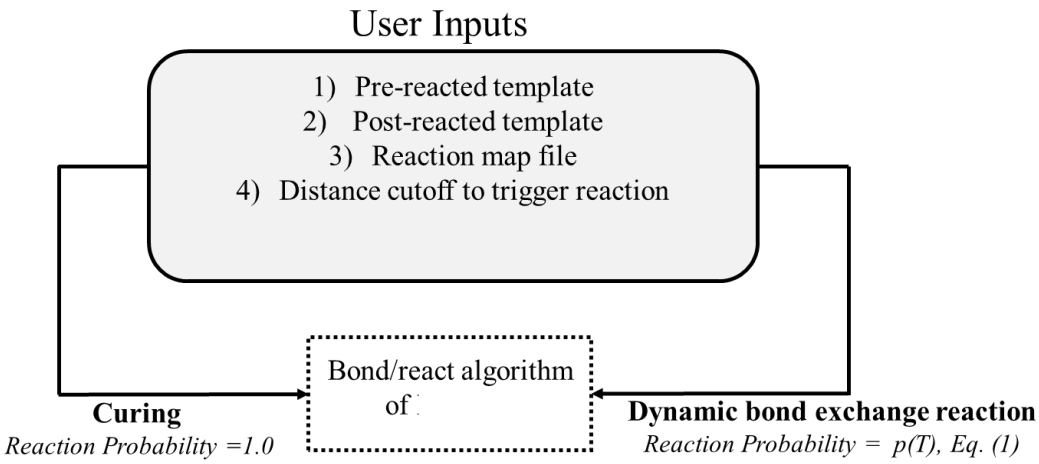

Figure A.1: Using probability of the reaction in the bond/react algorithm for curing dynamic bond exchange reactions in LAMMPS

Cross-linking of the neat vitrimer and vitrimer/CNT nanocomposite are shown in Figure A.3 and A.4, respectively.

A.3 Annealing protocol

To obtain an equilibrated density of the cured mixture, we heat (600K) and cool (1K) at 1 bar of pressure under NPT simulations for 50ps and repeat this cycle until the density of the annealed vitrimer is converged. Converged density plots for neat vitrimer and vitrimer/CNT nanocomposite are Shown in Figure A.5(a) and A.5(b), respectively.

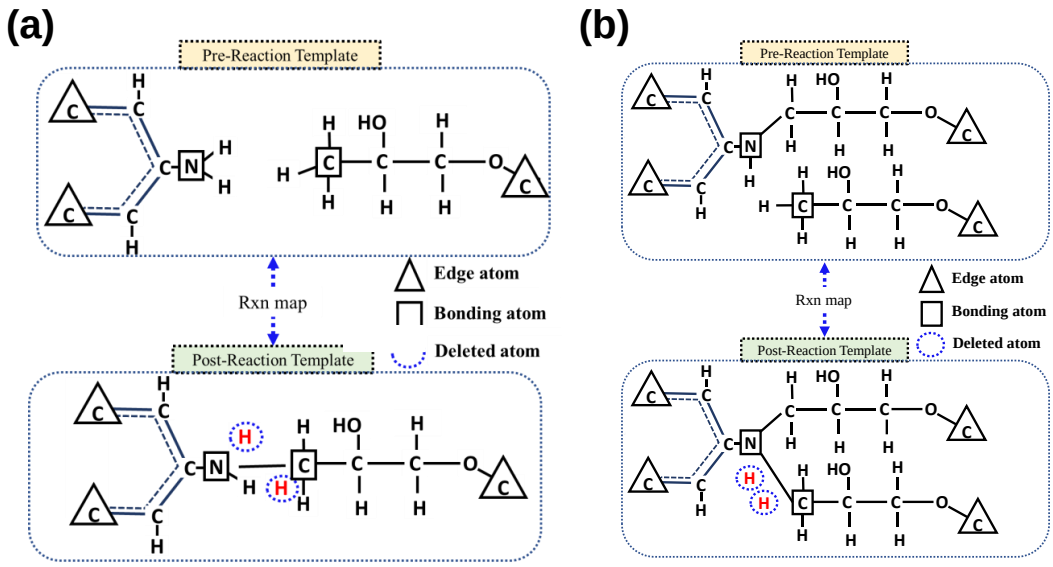

Figure A.2: Reaction template for (a) primary amine and (b) secondary amine reactions in the vitrimer curing

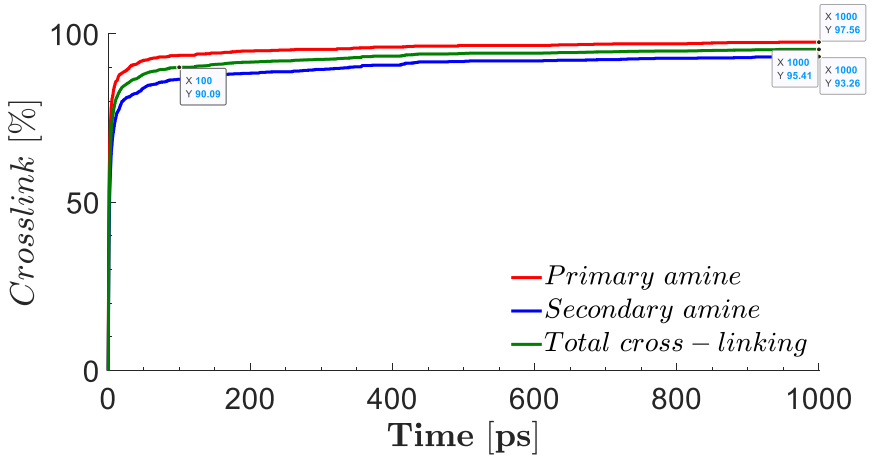

Figure A.3: Crosslinking vs. time during the curing process of neat vitrimer

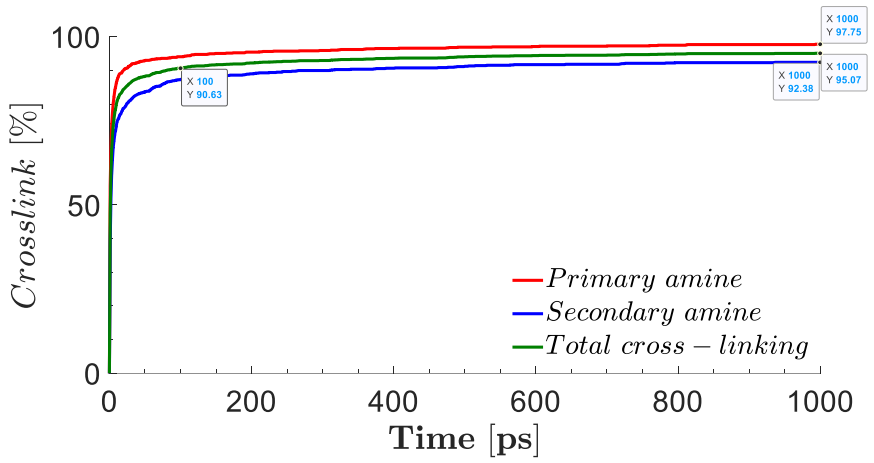

Figure A.4: Crosslinking vs. time during the curing process of vitrimer/CNT nanocomposite

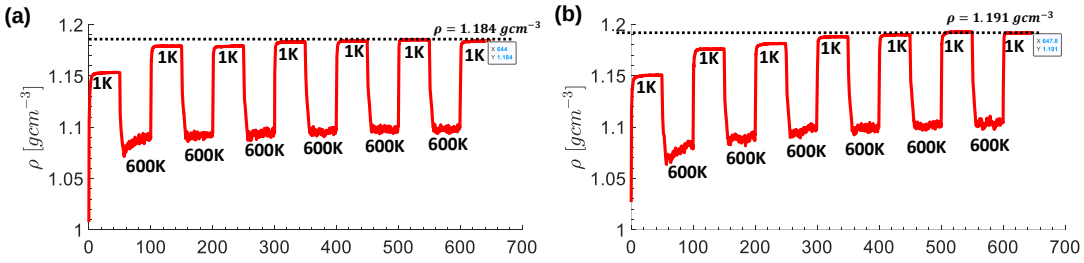

Figure A.5: Density convergence of the cured (a) neat vitrimer and (b) vitrimer/CNT nanocomposite under annealing

BIBLIOGRAPHY

BIBLIOGRAPHY

[1] CL Choy, FC Chen, and EL Ong. Anistropic thermal expansion of oriented crystalline polymers. *Polymer*, 20(10):1191–1198, 1979.

[2] CL Choy, FC Chen, and K Young. Negative thermal expansion in oriented crystalline polymers. *Journal of Polymer Science: Polymer Physics Edition*, 19(2):335–352, 1981.

[3] Hanyue Zhao and Nanxian Chen. An inverse adhesion problem for extracting interfacial pair potentials for the Al(0 0 1)/3C-SiC(0 0 1) interface. *Inverse Problems*, 24(3):035019, jun 2008.

[4] Michael Rubinstein, Ralph H Colby, et al. *Polymer physics*, volume 23. Oxford university press New York, 2003.

[5] ULF Gedde. *Polymer physics*. Springer Science & Business Media, 1995.

[6] Pierre-Gilles De Gennes and Pierre-Gilles Gennes. *Scaling concepts in polymer physics*. Cornell university press, 1979.

[7] David Kumar, Deepak Pawar, Gurmeet Singh, Sudhir Kamle, and PM Mohite. Development and analysis of aeroelastically tailored carbon fiber-cnt/pp composite bioinspired wings. In *33rd AIAA Applied Aerodynamics Conference*, page 3158, 2015.

[8] D Kumar, G Singh, PM Mohite, EM Lau, and Y-C Wang. Role of flexibility on the aerodynamic performance of a resonating hummingbird-inspired wing. *The Aeronautical Journal*, 127(1308):193–212, 2023.

[9] Amar K Mohanty, Feng Wu, Rosica Mincheva, Minna Hakkarainen, Jean-Marie Raquez, Deborah F Mielewski, Ramani Narayan, Anil N Netravali, and Manjusri Misra. Sustainable polymers. *Nature Reviews Methods Primers*, 2(1):46, 2022.

[10] Miao Hong and Eugene Y-X Chen. Future directions for sustainable polymers. *Trends in Chemistry*, 1(2):148–151, 2019.

[11] Damien Montarnal, Mathieu Capelot, François Tournilhac, and Ludwik Leibler. Silica-like malleable materials from permanent organic networks. *Science*, 334(6058):965–968, 2011.

[12] Mathieu Capelot, Miriam M Unterlass, François Tournilhac, and Ludwik Leibler. Catalytic control of the vitrimer glass transition. *ACS Macro Letters*, 1(7):789–792, 2012.

[13] Mathieu Capelot, Miriam M. Unterlass, François Tournilhac, and Ludwik Leibler. Catalytic control of the vitrimer glass transition. *ACS Macro Lett.*, 1(7):789–792, 2012.

[14] Rachel L Snyder, Claire AL Lidston, Guilhem X De Hoe, Maria JS Parvulescu, Marc A Hillmyer, and Geoffrey W Coates. Mechanically robust and reprocessable imine exchange networks from modular polyester pre-polymers. *Polym. Chem.*, 2020.

[15] Wim Denissen, Guadalupe Rivero, Renaud Nicolaÿ, Ludwik Leibler, Johan M Winne, and Filip E Du Prez. Vinylogous urethane vitrimers. *Adv. Funct. Mater.*, 25(16):2451–2457, 2015.

[16] Wusha Miao, Weike Zou, Yingwu Luo, Ning Zheng, Qian Zhao, and Tao Xie. Chemistry for covalent adaptable polymer networks structural tuning of polycaprolactone based thermadapt shape memory polymer. *Polym. Chem.*, 11:1369–1374, 2020.

[17] Xiangxu Chen, Matheus A Dam, Kanji Ono, Ajit Mal, Hongbin Shen, Steven R Nutt, Kevin Sheran, and Fred Wudl. A thermally re-mendable cross-linked polymeric material. *Sci.*, 295(5560):1698–1702, 2002.

[18] Chane Yuan, Min Zhi Rong, Ming Qiu Zhang, Ze Ping Zhang, and Yan Chao Yuan. Self-healing of polymers via synchronous covalent bond fission/radical recombination. *Chem. Mater.*, 23(22):5076–5081, nov 2011.

[19] Philip Taynton, Huagang Ni, Chengpu Zhu, Kai Yu, Samuel Loob, Yinghua Jin, H. Jerry Qi, and Wei Zhang. Repairable woven carbon fiber composites with full recyclability enabled by malleable polyimine networks. *Adv. Mater.*, 28(15):2904–2909, 2016.

[20] Pengfei Zhang and Guoqiang Li. Advances in healing-on-demand polymers and polymer composites. *Prog. Polym. Sci.*, 57:32–63, 2016.

[21] Yang Yang, Zhiqiang Pei, Xiqi Zhang, Lei Tao, Yen Wei, and Yan Ji. Carbon nanotube–vitrimer composite for facile and efficient photo-welding of epoxy. *Chem. Sci.*, 5(9):3486–3492, 2014.

[22] José L Pons. *Emerging actuator technologies: a micromechatronic approach.* John Wiley & Sons, 2005.

[23] István Mihálcz. Fundamental characteristics and design method for nickel-titanium shape memory alloy. *Periodica Polytechnica Mechanical Engineering*, 45(1):75–86, 2001.

[24] Neeraj Sharma, Tilak Raj, and Kamal Jangra. Applications of nickel-titanium alloy. *Journal of Engineering and Technology*, 5(1):1, 2015.

[25] DM Bigg. Mechanical property enhancement of semicrystalline polymers—a review. *Polymer Engineering & Science*, 28(13):830–841, 1988.

[26] C. L. Choy, S. P. Wong, and K. Young. Temperature dependence of the thermal expansivity of polymer crystals: Linear chain model. *Journal of Polymer Science: Polymer Physics Edition*, 22:979–991, 6 1984.

[27] A Keller and MJ Machin. Oriented crystallization in polymers. *Journal of Macromolecular Science, Part B: Physics*, 1(1):41–91, 1967.

[28] Leo Mandelkern. *Crystallization of Polymers: Volume 2, Kinetics and Mechanisms*. Cambridge University Press, 2004.

[29] Roland Seguela. Critical review of the molecular topology of semicrystalline polymers: The origin and assessment of intercrystalline tie molecules and chain entanglements. *Journal of Polymer Science Part B: Polymer Physics*, 43(14):1729–1748, 2005.

[30] Roland Séguéla. On the natural draw ratio of semi-crystalline polymers: review of the mechanical, physical and molecular aspects. *Macromolecular Materials and Engineering*, 292(3):235–244, 2007.

[31] Carter S Haines, Márcio D Lima, Na Li, Geoffrey M Spinks, Javad Foroughi, John DW Madden, Shi Hyeong Kim, Shaoli Fang, Mônica Jung de Andrade, Fatma Göktepe, et al. Artificial muscles from fishing line and sewing thread. *science*, 343(6173):868–872, 2014.

[32] Carter S Haines, Na Li, Geoffrey M Spinks, Ali E Aliev, Jiangtao Di, and Ray H Baughman. New twist on artificial muscles. *Proceedings of the National Academy of Sciences*, 113(42):11709–11716, 2016.

[33] Lawrence E Murr, Sara M Gaytan, Diana A Ramirez, Edwin Martinez, Jennifer Hernandez, Krista N Amato, Patrick W Shindo, Francisco R Medina, and Ryan B Wicker. Metal fabrication by additive manufacturing using laser and electron beam melting technologies. *Journal of Materials Science & Technology*, 28(1):1–14, 2012.

[34] Dirk Herzog, Vanessa Seyda, Eric Wycisk, and Claus Emmelmann. Additive manufacturing of metals. *Acta Materialia*, 117:371–392, sep 2016.

[35] Amit Bandyopadhyay, Yanning Zhang, and Susmita Bose. Recent developments in metal additive manufacturing. *Current Opinion in Chemical Engineering*, 28:96–104, 2020.

[36] Chi Zhang, Fei Chen, Zhifeng Huang, Mingyong Jia, Guiyi Chen, Yongqiang Ye, Yaojun Lin, Wei Liu, Bingqing Chen, Qiang Shen, Lianmeng Zhang, and Enrique J. Lavernia. Additive manufacturing of functionally graded materials: A review. *Materials Science and Engineering A*, 764:138209, sep 2019.

[37] Raeann VanSickle, David Foehring, Huck Beng Chew, and John Lambros. Microstructure effects on fatigue crack growth in additively manufactured Ti–6Al–4V. *Materials Science and Engineering A*, 795:139993, sep 2020.

[38] P. Bajaj, A. Hariharan, A. Kini, P. Kürnsteiner, D. Raabe, and E. A. Jägle. Steels in additive manufacturing: A review of their microstructure and properties. *Materials Science and Engineering A*, 772:138633, jan 2020.

[39] Nima Shamsaei, Aref Yadollahi, Linkan Bian, and Scott M Thompson. An overview of direct laser deposition for additive manufacturing; part ii: Mechanical behavior, process parameter optimization and control. *Additive Manufacturing*, 8:12–35, 2015.

[40] Jamison L Bartlett and Xiaodong Li. An overview of residual stresses in metal powder bed fusion. *Additive Manufacturing*, 27:131–149, 2019.

[41] Liang Wang, Sergio D. Felicelli, and James E. Craig. Experimental and numerical study of the LENS rapid fabrication process. *Journal of Manufacturing Science and Engineering, Transactions of the ASME*, 131(4):0410191–0410198, aug 2009.

[42] Liang Wang, Sergio D Felicelli, and Phillip Pratt. Residual stresses in lens-deposited aisi 410 stainless steel plates. *Materials Science and Engineering: A*, 496(1-2):234–241, 2008.

[43] Jinghao Li, Xianglin Zhou, Mathieu Brochu, Nikolas Provatas, and Yaoyao Fiona Zhao. Solidification microstructure simulation of ti-6al-4v in metal additive manufacturing: A review. *Additive Manufacturing*, 31:100989, 2020.

[44] Scott M Thompson, Linkan Bian, Nima Shamsaei, and Aref Yadollahi. An overview of direct laser deposition for additive manufacturing; part i: Transport phenomena, modeling and diagnostics. *Additive Manufacturing*, 8:36–62, 2015.

[45] Shijia Chen, Gildas Guillemot, and Charles André Gandin. Three-dimensional cellular automaton-finite element modeling of solidification grain structures for arc-welding processes. *Acta Materialia*, 115:448–467, aug 2016.

[46] Xuxiao Li and Wenda Tan. Numerical investigation of effects of nucleation mechanisms on grain structure in metal additive manufacturing. *Computational Materials Science*, 153:159–169, oct 2018.

[47] O. Zinovieva, A. Zinoviev, and V. Ploshikhin. Three-dimensional modeling of the microstructure evolution during metal additive manufacturing. *Computational Materials Science*, 141:207–220, jan 2018.

[48] P Prabhakar, William J Sames, R Dehoff, and Sudarsanam Suresh Babu. Computational modeling of residual stress formation during the electron beam melting process for inconel 718. *Additive Manufacturing*, 7:83–91, 2015.

[49] Seshadev Sahoo and Kevin Chou. Phase-field simulation of microstructure evolution of Ti-6Al-4V in electron beam additive manufacturing process. *Additive Manufacturing*, 9:14–24, jan 2016.

[50] Joel Heang Kuan Tan, Swee Leong Sing, and Wai Yee Yeong. Microstructure modelling for metallic additive manufacturing: a review. *Virtual and Physical Prototyping*, 15(1):87–105, jan 2020.

[51] Daan Frenkel and Berend Smit. *Understanding molecular simulation: from algorithms to applications*, volume 1. Elsevier, 2001.

[52] Loup Verlet. Computer" experiments" on classical fluids. i. thermodynamical properties of lennard-jones molecules. *Physical review*, 159(1):98, 1967.

[53] William C Swope, Hans C Andersen, Peter H Berens, and Kent R Wilson. A computer simulation method for the calculation of equilibrium constants for the formation of physical clusters of molecules: Application to small water clusters. *The Journal of chemical physics*, 76(1):637–649, 1982.

[54] XW Zhou, RA Johnson, and HNG Wadley. Misfit-energy-increasing dislocations in vapor-deposited cofe/nife multilayers. *Physical Review B*, 69(14):144113, 2004.

[55] MI Baskes. Application of the embedded-atom method to covalent materials: a semiempirical potential for silicon. *Physical review letters*, 59(23):2666, 1987.

[56] Michael I Baskes. Modified embedded-atom potentials for cubic materials and impurities. *Physical review B*, 46(5):2727, 1992.

[57] Pnina Dauber-Osguthorpe, Victoria A Roberts, David J Osguthorpe, Jon Wolff, Moniqe Genest, and Arnold T Hagler. Structure and energetics of ligand binding to proteins: Escherichia coli dihydrofolate reductase-trimethoprim, a drug-receptor system. *Proteins: Structure, Function, and Bioinformatics*, 4(1):31–47, 1988.

[58] Thomas E Gartner III and Arthi Jayaraman. Modeling and simulations of polymers: a roadmap. *Macromolecules*, 52(3):755–786, 2019.

[59] Louis A Girifalco and Victor G Weizer. Application of the morse potential function to cubic metals. *Physical Review*, 114(3):687, 1959.

[60] Chinmaya R. Dandekar and Yung C. Shin. Molecular dynamics based cohesive zone law for describing Al-SiC interface mechanics. *Composites Part A: Applied Science and Manufacturing*, 42(4):355–363, apr 2011.

[61] Xuan Luo, Gefei Qian, EG Wang, and Changfeng Chen. Molecular-dynamics simulation of al/sic interface structures. *Physical Review B*, 59(15):10125, 1999.

[62] Huai Sun. Ab initio calculations and force field development for computer simulation of polysilanes. *Macromolecules*, 28(3):701–712, 1995.

[63] Graeme J Ackland and Vaclav Vitek. Many-body potentials and atomic-scale relaxations in noble-metal alloys. *Physical review B*, 41(15):10324, 1990.

[64] Steven J Plimpton and Aidan P Thompson. Computational aspects of many-body potentials. *MRS bulletin*, 37(5):513–521, 2012.

[65] John Edward Jones. On the determination of molecular fields.—ii. from the equation of state of a gas. *Proceedings of the Royal Society of London. Series A, Containing Papers of a Mathematical and Physical Character*, 106(738):463–477, 1924.

[66] A. Ramazani, A. Reihani, A. Soleimani, R. Larson, and V. Sundararaghavan. Molecular dynamics study of phonon transport in graphyne nanotubes. *Carbon*, 123:635 – 644, 2017.

[67] Amin Reihani, Alireza Soleimani, Sajad Kargar, Veera Sundararaghavan, and Ali Ramazani. Graphyne nanotubes: Materials with ultralow phonon mean free path and strong optical phonon scattering for thermoelectric applications. *The Journal of Physical Chemistry C*, 122(39):22688–22698, 2018.

[68] Adri CT Van Duin, Siddharth Dasgupta, Francois Lorant, and William A Goddard. Reaxff: a reactive force field for hydrocarbons. *The Journal of Physical Chemistry A*, 105(41):9396–9409, 2001.

[69] Tao Liang, Yun Kyung Shin, Yu-Ting Cheng, Dundar E Yilmaz, Karthik Guda Vishnu, Osvalds Verners, Chenyu Zou, Simon R Phillpot, Susan B Sinnott, and Adri CT Van Duin. Reactive potentials for advanced atomistic simulations. *Annual review of materials research*, 43:109–129, 2013.

[70] Thomas P Senftle, Sungwook Hong, Md Mahbubul Islam, Sudhir B Kylasa, Yuanxia Zheng, Yun Kyung Shin, Chad Junkermeier, Roman Engel-Herbert, Michael J Janik, Hasan Metin Aktulga, et al. The reaxff reactive force-field: development, applications and future directions. *npj Computational Materials*, 2(1):1–14, 2016.

[71] Ken-ichi Nomura, Rajiv K Kalia, Aiichiro Nakano, and Priya Vashishta. A scalable parallel algorithm for large-scale reactive force-field molecular dynamics simulations. *Computer Physics Communications*, 178(2):73–87, 2008.

[72] Bernd Hartke and Stefan Grimme. Reactive force fields made simple. *Physical Chemistry Chemical Physics*, 17(26):16715–16718, 2015.

[73] Yun Kyung Shin, Tzu-Ray Shan, Tao Liang, Mark J Noordhoek, Susan B Sinnott, Adri CT Van Duin, and Simon R Phillpot. Variable charge many-body interatomic potentials. *MRS bulletin*, 37(5):504–512, 2012.

[74] Donald W Brenner. Empirical potential for hydrocarbons for use in simulating the chemical vapor deposition of diamond films. *Physical review B*, 42(15):9458, 1990.

[75] Donald W Brenner, Olga A Shenderova, Judith A Harrison, Steven J Stuart, Boris Ni, and Susan B Sinnott. A second-generation reactive empirical bond order (rebo) potential energy expression for hydrocarbons. *Journal of Physics: Condensed Matter*, 14(4):783, 2002.

[76] Jacob R Gissinger, Benjamin D Jensen, and Kristopher E Wise. Modeling chemical reactions in classical molecular dynamics simulations. *Polymer*, 128:211–217, 2017.

[77] Jacob R Gissinger, Benjamin D Jensen, and Kristopher E Wise. Reacter: a heuristic method for reactive molecular dynamics. *Macromolecules*, 53(22):9953–9961, 2020.

[78] Enze Chen, Qian Yang, Vincent Dufour-Décieux, Carlos A Sing-Long, Rodrigo Freitas, and Evan J Reed. Transferable kinetic monte carlo models with thousands of reactions learned from molecular dynamics simulations. *The Journal of Physical Chemistry A*, 123(9):1874–1881, 2019.

[79] Matthew K Mcbride, Brady T Worrell, Tobin Brown, Lewis M Cox, Nancy Sowan, Chen Wang, Maciej Podgorski, Alina M Martinez, and Christopher N Bowman. Enabling Applications of Covalent Adaptable Networks. *Annu. Rev. Chem. Biomol. Eng*, 10:175–198, 2019.

[80] Wim Denissen, Johan M Winne, and Filip E Du Prez. Vitrimers: permanent organic networks with glass-like fluidity. *Chem. sci.*, 7(1):30–38, 2016.

[81] Lingqiao Li, Xi Chen, Kailong Jin, and John M. Torkelson. Vitrimers Designed Both to Strongly Suppress Creep and to Recover Original Cross-Link Density after Reprocessing: Quantitative Theory and Experiments. *Macromolecules*, 51(15):5537–5546, aug 2018.

[82] Stijn Billiet, Kevin De Bruycker, Frank Driessen, Hannelore Goossens, Veronique Van Speybroeck, Johan M Winne, and Filip E Du Prez. Triazolinediones enable ultrafast and reversible click chemistry for the design of dynamic polymer systems. *Nat. chem.*, 6(9):815, 2014.

[83] Wim Denissen, Guadalupe Rivero, Renaud Nicolaÿ, Ludwik Leibler, Johan M Winne, and Filip E Du Prez. Vinylogous urethane vitrimers. *Adv. Funct. Mater.*, 25(16):2451–2457, 2015.

[84] Chunyu Li and Alejandro Strachan. Molecular dynamics predictions of thermal and mechanical properties of thermoset polymer epon862/detda. *Polymer*, 52(13):2920 – 2928, 2011.

[85] Tomonaga Okabe, Yutaka Oya, Koichi Tanabe, Gota Kikugawa, and Kenichi Yoshioka. Molecular dynamics simulation of crosslinked epoxy resins: Curing and mechanical properties. *Eur. Polym. J.*, 80:78 – 88, 2016.

[86] Nicholas Fasanella and Veera Sundararaghavan. Atomistic modeling of thermomechanical properties of swnt/epoxy nanocomposites. *Model. Simul. Mater. Sci. Eng.*, 23(6):065003, 2015.

[87] Vikas Varshney, Soumya S. Patnaik, Ajit K. Roy, and Barry L. Farmer. Heat transport in epoxy networks: A molecular dynamics study. *Polymer*, 50(14):3378 – 3385, 2009.

[88] A Kumar, V Sundararaghavan, and A R Browning. Study of temperature dependence of thermal conductivity in cross-linked epoxies using molecular dynamics simulations with long range interactions. *Model. Simul. Mater. Sci. Eng.*, 22(2):025013, 2014.

[89] A Lakshmanan, S Srivastava, A Ramazani, and V Sundararaghavan. Thermal conductivity of pillared graphene-epoxy nanocomposites using molecular dynamics. *Applied Physics Letters*, 112(15):151902, 2018.

[90] Nicholas A. Fasanella and Veera Sundararaghavan. Atomistic modeling of thermal conductivity of epoxy nanotube composites. *JOM*, 68(5):1396–1410, May 2016.

[91] Ananyo Bandyopadhyay, Pavan K. Valavala, Thomas C. Clancy, Kristopher E. Wise, and Gregory M. Odegard. Molecular modeling of crosslinked epoxy polymers: The effect of crosslink density on thermomechanical properties. *Polymer*, 52(11):2445 – 2452, 2011.

[92] Susanta Ghosh, Abhishek Kumar, Veera Sundararaghavan, and Anthony M. Waas. Non-local modeling of epoxy using an atomistically-informed kernel. *International Journal of Solids and Structures*, 50(19):2837 – 2845, 2013.

[93] Susanta Ghosh, Veera Sundararaghavan, and Anthony M. Waas. Construction of multi-dimensional isotropic kernels for nonlocal elasticity based on phonon dispersion data. *International Journal of Solids and Structures*, 51(2):392 – 401, 2014.

[94] N Vu-Bac, MA Bessa, Timon Rabczuk, and Wing Kam Liu. A multiscale model for the quasi-static thermo-plastic behavior of highly cross-linked glassy polymers. *Macromolecules*, 48(18):6713–6723, 2015.

[95] Simone Ciarella, Francesco Sciortino, and Wouter G Ellenbroek. Dynamics of vitrimers: Defects as a highway to stress relaxation. *Physical review letters*, 121(5):058003, 2018.

[96] Bernardo Oyarzún and Bortolo Matteo Mognetti. Efficient sampling of reversible cross-linking polymers: Self-assembly of single-chain polymeric nanoparticles. *Journal of Chemical Physics*, 148(11), mar 2018.

[97] Jian-Bo Wu, Shu-Jia Li, Hong Liu, Hu-Jun Qian, and Zhong-Yuan Lu. Dynamics and reaction kinetics of coarse-grained bulk vitrimers: a molecular dynamics study. *Physical Chemistry Chemical Physics*, 21(24):13258–13267, 2019.

[98] Frank Smallenburg, Ludwik Leibler, and Francesco Sciortino. Patchy particle model for vitrimers. *Physical Review Letters*, 111(18), oct 2013.

[99] Francesco Sciortino. Three-body potential for simulating bond swaps in molecular dynamics. *European Physical Journal E*, 40(1), jan 2017.

[100] Hua Yang, Kai Yu, Xiaoming Mu, Yujie Wei, Yafang Guo, and H. Jerry Qi. Molecular dynamics studying on welding behavior in thermosetting polymers due to bond exchange reactions. *RSC Advances*, 6(27):22476–22487, 2016.

[101] Yaguang Sun, Hua Yang, Wenjie Xia, and Yafang Guo. Molecular dynamics simulations of surface welding in crosslinked networks with thermally reversible linkages. *Applied Surface Science*, 527:146947, oct 2020.

[102] Hua Yang, Kai Yu, Xiaoming Mu, Xinghua Shi, Yujie Wei, Yafang Guo, and H Jerry Qi. A molecular dynamics study of bond exchange reactions in covalent adaptable networks. *Soft Matter*, 11(31):6305–6317, 2015.

[103] Steve Plimpton. Fast parallel algorithms for short-range molecular dynamics. Technical report, Sandia National Labs., Albuquerque, NM (United States), 1993.

[104] Alaitz Rekondo, Roberto Martin, Alaitz Ruiz de Luzuriaga, Germán Cabañero, Hans J Grande, and Ibon Odriozola. Catalyst-free room-temperature self-healing elastomers based on aromatic disulfide metathesis. *Mater. Horiz.*, 1(2):237–240, 2014.

[105] Alaitz Ruiz de Luzuriaga, Jon M Matxain, Fernando Ruipérez, Roberto Martin, José M Asua, Germán Cabañero, and Ibon Odriozola. Transient mechanochromism in epoxy vitrimer composites containing aromatic disulfide crosslinks. *J. Mater. Chem. C*, 4(26):6220–6223, 2016.

[106] Alaitz Ruiz de Luzuriaga, Roberto Martin, Nerea Markaide, Alaitz Rekondo, Germán Cabañero, Javier Rodríguez, and Ibon Odriozola. Epoxy resin with exchangeable disulfide crosslinks to obtain reprocessable, repairable and recyclable fiber-reinforced thermoset composites. *Mater. Horiz.*, 3(3):241–247, 2016.

[107] V. Sundararaghavan and A. Kumar. Molecular dynamics simulations of compressive yielding in cross-linked epoxies in the context of argon theory. *Int.J.Plasticity*, 47:111 – 125, 2013.

[108] Ralf Steudel. Properties of sulfur-sulfur bonds. *Angew. Chem.Int.Edit.*, 14(10):655–664, 1975.

[109] Nathan J Van Zee and Renaud Nicolaÿ. Vitrimers: Permanently crosslinked polymers with dynamic network topology. *Progress in Polymer Science*, page 101233, 2020.

[110] Yanwu Zhou, Ramon Groote, Johannes G.P. Goossens, Rint P. Sijbesma, and Johan P.A. Heuts. Tuning PBT vitrimer properties by controlling the dynamics of the adaptable network. *Polymer Chemistry*, 10(1):136–144, jan 2019.

[111] Kunhao Yu, An Xin, and Qiming Wang. Mechanics of self-healing polymer networks crosslinked by dynamic bonds. *Journal of the Mechanics and Physics of Solids*, 121:409–431, dec 2018.

[112] Jasmine Gupta, Cletus Nunes, and Sriramakamal Jonnalagadda. A molecular dynamics approach for predicting the glass transition temperature and plasticization effect in amorphous pharmaceuticals. *Mol. Pharm.*, 10(11):4136–4145, nov 2013.

[113] EA Boulter, M Cohen, and ML Deviney. High-service temperature polyether amide thermoset resins-new materials for electrical insulation and high strength composites. In *Proceedings: Electrical Insulation Conference and Electrical Manufacturing and Coil Winding Conference*, pages 249–253. IEEE, 1997.

[114] Mariana Ionita. Multiscale molecular modeling of swcnts/epoxy resin composites mechanical behaviour. *Compos. B. Eng.*, 43(8):3491–3496, 2012.

[115] Ali Shokuhfar and Behrouz Arab. The effect of cross linking density on the mechanical properties and structure of the epoxy polymers: molecular dynamics simulation. *J. mol. model.*, 19(9):3719–3731, 2013.

[116] CK Knox, J Andzelm, JL Lenhart, AR Browning, and S Christensen. High strain rate mechanical behavior of epoxy networks from molecular dynamics simulations. In *27th Army Science Conference Proceedings*, 2010.

[117] John M Barton, AS Deazle, I Hamerton, BJ Howlin, and JR Jones. The application of molecular simulation to the rational design of new materials: 2. prediction of the physico-mechanical properties of linear epoxy systems. *Polymer*, 38(17):4305–4310, 1997.

[118] Luman Zhang, Niels De Greef, Gerhard Kalinka, Bart Van Bilzen, Jean-Pierre Locquet, Ignaas Verpoest, and Jin Won Seo. Carbon nanotube-grafted carbon fiber polymer composites: damage characterization on the micro-scale. *Compos. B. Eng.*, 126:202–210, 2017.

[119] Asa H Barber, Sidney R Cohen, Shmuel Kenig, and H Daniel Wagner. Interfacial fracture energy measurements for multi-walled carbon nanotubes pulled from a polymer matrix. *Compos. Sci. Technol.*, 64(15):2283–2289, 2004.

[120] Terumasa Tsuda, Toshio Ogasawara, Fei Deng, and Nobuo Takeda. Direct measurements of interfacial shear strength of multi-walled carbon nanotube/peek composite using a nano-pullout method. *Compos. Sci. Technol.*, 71(10):1295–1300, 2011.

[121] Omid Zabihi, Mojtaba Ahmadi, Saeid Nikafshar, Karthik Chandrakumar Preyeswary, and Minoo Naebe. A technical review on epoxy-clay nanocomposites: Structure, properties, and their applications in fiber reinforced composites. *Composites Part B: Engineering*, 135:1–24, 2018.

[122] Naheed Saba, Mohammad Jawaid, Othman Y Alothman, MT Paridah, and Azman Hassan. Recent advances in epoxy resin, natural fiber-reinforced epoxy composites and their applications. *Journal of Reinforced Plastics and Composites*, 35(6):447–470, 2016.

[123] María L. Arias, Patricia M. Frontini, and Roberto J.J. Williams. Analysis of the damage zone around the crack tip for two rubber-modified epoxy matrices exhibiting different toughenability. *Polymer*, 44:1537–1546, 3 2003.

[124] Gurmeet Singh, David Kumar, and PM Mohite. Damage modelling of epoxy material under uniaxial tension based on micromechanics and experimental analysis. *Archive of Applied Mechanics*, 87(4):721–736, 2017.

[125] Pavan Kumar Penumakala, Jose Santo, and Alen Thomas. A critical review on the fused deposition modeling of thermoplastic polymer composites. *Composites Part B: Engineering*, 201:108336, 2020.

[126] Dhaiwat N Trivedi and Nikunj V Rachchh. Graphene and its application in thermoplastic polymers as nano-filler-a review. *Polymer*, 240:124486, 2022.

[127] Jie Zheng, Zhuang Mao Png, Shi Hoe Ng, Guo Xiong Tham, Enyi Ye, Shermin S. Goh, Xian Jun Loh, and Zibiao Li. Vitrimers: Current research trends and their emerging applications. *Materials Today*, 51:586–625, 12 2021.

[128] Pengfei Zhang and Guoqiang Li. Advances in healing-on-demand polymers and polymer composites. *Progress in Polymer Science*, 57:32–63, 2016.

[129] Shafiqul Islam and Gajanan Bhat. Progress and challenges in self-healing composite materials. *Materials Advances*, 2(6):1896–1926, 2021.

[130] Seppe Terryn, Jakob Langenbach, Ellen Roels, Joost Brancart, Camille Bakkali-Hassani, Quentin-Arthur Poutrel, Antonia Georgopoulou, Thomas George Thuruthel, Ali Safaei, Pasquale Ferrentino, et al. A review on self-healing polymers for soft robotics. *Materials Today*, 47:187–205, 2021.

[131] Xiaoguang Li, Siwu Wu, Shuangjian Yu, Chong Xiao, Zhenghai Tang, and Baochun Guo. A facile one-pot route to elastomeric vitrimers with tunable mechanical performance and superior creep resistance. *Polymer*, 238:124379, 2022.

[132] Amber M Hubbard, Yixin Ren, Dominik Konkolewicz, Alireza Sarvestani, Catalin R Picu, Gary S Kedziora, Ajit Roy, Vikas Varshney, and Dhriti Nepal. Vitrimer transition temperature identification: Coupling various thermomechanical methodologies. *ACS Applied Polymer Materials*, 3(4):1756–1766, 2021.

[133] William N Findley and Francis A Davis. *Creep and relaxation of nonlinear viscoelastic materials*. Courier corporation, 2013.

[134] W Bradley, WJ Cantwell, and Hans Henning Kausch. Viscoelastic creep crack growth: a review of fracture mechanical analyses. *Mechanics of Time-Dependent Materials*, 1:241–268, 1997.

[135] Mário F Sá, Augusto M Gomes, João R Correia, and Nuno Silvestre. Creep behavior of pultruded gfrp elements–part 1: Literature review and experimental study. *Composite Structures*, 93(10):2450–2459, 2011.

[136] Hal F Brinson, L Catherine Brinson, et al. *Polymer engineering science and viscoelasticity: An introduction*. Springer, 2008.

[137] SW Bradley, PM Puckett, WL Bradley, and HJ Sue. Viscoelastic creep characteristics of neat thermosets and thermosets reinforced with e-glass. *Journal of Composites, Technology and Research*, 20(1):51–58, 1998.

[138] Robert A. Riggleman, Kenneth S. Schweizer, and Juan J. De Pablo. Nonlinear creep in a polymer glass. *Macromolecules*, 41:4969–4977, 7 2008.

[139] Wei Jian and Denvid Lau. Creep performance of cnt-based nanocomposites: A parametric study. *Carbon*, 153:745–756, 11 2019.

[140] Zhicheng Chang, Yafei Wang, Zhiyu Zhang, Ke Gao, Guanyi Hou, Jianxiang Shen, Liqun Zhang, and Jun Liu. Creep behavior of polymer nanocomposites: Insights from molecular dynamics simulation. *Polymer*, 228:123895, 7 2021.

[141] A Plaseied and A Fatemi. Tensile creep and deformation modeling of vinyl ester polymer and its nanocomposite. *Journal of Reinforced Plastics and Composites*, 28(14):1775–1788, 2009.

[142] Hau-Nan Lee, Keewook Paeng, Stephen F Swallen, and MD Ediger. Direct measurement of molecular mobility in actively deformed polymer glasses. *Science*, 323(5911):231–234, 2009.

[143] Chanwook Park, Geonwoo Kim, Jiwon Jung, Balaji Krishnakumar, Sravendra Rana, and Gun Jin Yun. Enhanced self-healing performance of graphene oxide/vitrimer nanocomposites: A molecular dynamics simulations study. *Polymer*, 206:122862, 10 2020.

[144] Amber M Hubbard, Yixin Ren, Catalin R Picu, Alireza Sarvestani, Dominik Konkolewicz, Ajit K Roy, Vikas Varshney, and Dhriti Nepal. Creep mechanics of epoxy vitrimer materials. *ACS Applied Polymer Materials*, 2022.

[145] Wenhao Liu, Daniel F Schmidt, and Emmanuelle Reynaud. Catalyst selection, creep, and stress relaxation in high-performance epoxy vitrimers. *Industrial & Engineering Chemistry Research*, 56(10):2667–2672, 2017.

[146] Shuyin Jiao and Yashashree Kulkarni. Molecular dynamics study of creep mechanisms in nanotwinned metals. *Computational Materials Science*, 110:254–260, 12 2015.

[147] Gurmeet Singh, Anthony M Waas, and Veera Sundararaghavan. Understanding defect structures in nanoscale metal additive manufacturing via molecular dynamics. *Computational Materials Science*, 200:110807, 2021.

[148] Gurmeet Singh and Veera Sundararaghavan. Modeling self-healing behavior of vitrimers using molecular dynamics with dynamic cross-linking capability. *Chemical Physics Letters*, 760:137966, 2020.

[149] P. Keblinski, D. Wolf, and H. Gleiter. Molecular-dynamics simulation of grain-boundary diffusion creep. *Interface Science 1998 6:3*, 6:205–212, 7 1998.

[150] V. Yamakov, D. Wolf, S. R. Phillpot, and H. Gleiter. Grain-boundary diffusion creep in nanocrystalline palladium by molecular-dynamics simulation. *Acta Materialia*, 50:61–73, 1 2002.

[151] Ricardo Simoes, António M Cunha, and Witold Brostow. Molecular dynamics simulations of polymer viscoelasticity: effect of the loading conditions and creep behaviour. *Modelling and Simulation in Materials Science and Engineering*, 14(2):157, 2006.

[152] Robert A Riggleman, Hau-Nan Lee, Mark D Ediger, and Juan J De Pablo. Free volume and finite-size effects in a polymer glass under stress. *Physical Review Letters*, 99(21):215501, 2007.

[153] Iwan H Sahputra and Andreas T Echtermeyer. Creep–fatigue relationship in polymer: Molecular dynamics simulations approach. *Macromolecular Theory and Simulations*, 24(1):65–73, 2015.

[154] A. L. Bowman, S. Mun, S. Nouranian, B. D. Huddleston, S. R. Gwaltney, M. I. Baskes, and M. F. Horstemeyer. Free volume and internal structural evolution during creep in model amorphous polyethylene by molecular dynamics simulations. *Polymer*, 170:85–100, 4 2019.

[155] Xueliang Li, Xiaoyu Zhang, Jianzhong Chen, Li Huang, and Yong Lv. Uniaxial tensile creep behavior of epoxy-based polymer using molecular simulation. *Polymers*, 13(2):261, 2021.

[156] Wim Denissen, Johan M Winne, and Filip E Du Prez. Vitrimers: permanent organic networks with glass-like fluidity. *Chemical science*, 7(1):30–38, 2016.

[157] Steve Plimpton. Fast parallel algorithms for short-range molecular dynamics. *Journal of Computational Physics*, 117(1):1–19, 1995.

[158] Aidan P Thompson, H Metin Aktulga, Richard Berger, Dan S Bolintineanu, W Michael Brown, Paul S Crozier, Pieter J in't Veld, Axel Kohlmeyer, Stan G Moore, Trung Dac Nguyen, et al. Lammps-a flexible simulation tool for particle-based materials modeling at the atomic, meso, and continuum scales. *Computer Physics Communications*, 271:108171, 2022.

[159] Vikas Varshney, Soumya S Patnaik, Ajit K Roy, and Barry L Farmer. A molecular dynamics study of epoxy-based networks: cross-linking procedure and prediction of molecular and material properties. *Macromolecules*, 41(18):6837–6842, 2008.

[160] Mohammad Atif Faiz Afzal, Andrea R. Browning, Alexander Goldberg, Mathew D. Halls, Jacob L. Gavartin, Tsuguo Morisato, Thomas F. Hughes, David J. Giesen, and Joseph E. Goose. High-throughput molecular dynamics simulations and validation of thermophysical properties of polymers for various applications. *ACS Applied Polymer Materials*, 3:630, 2 2021.

[161] Xueliang Li, Xiaoyu Zhang, Jianzhong Chen, Li Huang, and Yong Lv. The mechanical properties and creep behavior of epoxy polymer under the marine environment: A molecular dynamics investigation. *Materials Today Communications*, 28:102737, 9 2021.

[162] Lik ho Tam, Jinqiao Jiang, Zechuan Yu, John Orr, and Chao Wu. Molecular dynamics investigation on the interfacial shear creep between carbon fiber and epoxy matrix. *Applied Surface Science*, 537:148013, 1 2021.

[163] Herbert Edelsbrunner and Ernst P Mücke. Three-dimensional alpha shapes. *ACM Transactions on Graphics (TOG)*, 13(1):43–72, 1994.

[164] Alexander Stukowski. Computational analysis methods in atomistic modeling of crystals. *JOM*, 66(3):399–407, 2014.

[165] Sheng Wang, Songqi Ma, Qiong Li, Xiwei Xu, Binbo Wang, Kaifeng Huang, Yanlin Liu, and Jin Zhu. Facile preparation of polyimine vitrimers with enhanced creep resistance and thermal and mechanical properties via metal coordination. *Macromolecules*, 53(8):2919–2931, 2020.

[166] Chunbing Wu and Wen Zheng. Position and force control of a twisted and coiled polymeric actuator. *IEEE Access*, 8:137226–137234, 2020.

[167] Lokesh Saharan and Yonas Tadesse. Novel twisted and coiled polymer artificial muscles for biomedical and robotics applications. *Materials for Biomedical Engineering: Nanobiomaterials in Tissue Engineering*, pages 45–75, 2019.

[168] Sameh Tawfick and Yichao Tang. Stronger artificial muscles, with a twist. *Science*, 365(6449):125–126, 2019.

[169] Hetao Chu, Xinghao Hu, Zhong Wang, Jiuke Mu, Na Li, Xiaoshuang Zhou, Shaoli Fang, Carter S Haines, Jong Woo Park, Si Qin, et al. Unipolar stroke, electroosmotic pump carbon nanotube yarn muscles. *Science*, 371(6528):494–498, 2021.

[170] Yara Almubarak and Yonas Tadesse. Twisted and coiled polymer (tcp) muscles embedded in silicone elastomer for use in soft robot. *International Journal of Intelligent Robotics and Applications*, 1:352–368, 2017.

[171] Dharshika Kongahage and Javad Foroughi. Actuator materials: review on recent advances and future outlook for smart textiles. *Fibers*, 7(3):21, 2019.

[172] Min Zou, Sitong Li, Xiaoyu Hu, Xueqi Leng, Run Wang, Xiang Zhou, and Zunfeng Liu. Progresses in tensile, torsional, and multifunctional soft actuators. *Advanced Functional Materials*, 31(39):2007437, 2021.

[173] Benjamin Pawlowski, Jiefeng Sun, Jing Xu, Yingxiang Liu, and Jianguo Zhao. Modeling of soft robots actuated by twisted-and-coiled actuators. *IEEE/ASME Transactions on Mechatronics*, 24(1):5–15, 2018.

[174] Jun Zhang, Kaushik Iyer, Anthony Simeonov, and Michael C Yip. Modeling and inverse compensation of hysteresis in supercoiled polymer artificial muscles. *IEEE Robotics and Automation Letters*, 2(2):773–780, 2017.

[175] Farzad Karami and Yonas Tadesse. Modeling of twisted and coiled polymer (tcp) muscle based on phenomenological approach. *Smart Materials and Structures*, 26(12):125010, 2017.

[176] Jiefeng Sun and Jianguo Zhao. Physics-based modeling of twisted-and-coiled actuators using cosserat rod theory. *IEEE Transactions on Robotics*, 38(2):779–796, 2021.

[177] Qianxi Yang and Guoqiang Li. A top-down multi-scale modeling for actuation response of polymeric artificial muscles. *Journal of the Mechanics and Physics of Solids*, 92:237–259, 2016.

[178] Youyong Li and William A Goddard. Nylon 6 crystal structures, folds, and lamellae from theory. *Macromolecules*, 35(22):8440–8455, 2002.

[179] Howard W Starkweather Jr and Robert E Moynihan. Density, infrared absorption, and crystallinity in 66 and 610 nylons. *Journal of polymer science*, 22(102):363–368, 1956.

[180] Howard W Starkweather Jr, George E Moore, John E Hansen, Thomas M Roder, and Richard E Brooks. Effect of crystallinity on the properties of nylons. *Journal of Polymer Science*, 21(98):189–204, 1956.

[181] Tanya L. Chantawansri, In Chul Yeh, and Alex J. Hsieh. Investigating the glass transition temperature at the atom-level in select model polyamides: A molecular dynamics study. *Polymer*, 81:50–61, 12 2015.

[182] Rakesh H Mehta. Physical constants of various polyamides. *Polymer Handbook, fourth ed., John Wiley & Sons, Hoboken, New Jersey, USA*, pages 121–133, 1999.

[183] Kohji Tashiro and Yayoi Yoshioka. Molecular dynamics simulation of the structural and mechanical property changes in the brill transition of nylon 10/10 crystal. *Polymer*, 45:4337–4348, 2004.

[184] F. C. Chen, C. L. Choy, S. P. Wong, and K. Young. Negative thermal expansivity of polymer crystals: Planar zig-zag chain model. *Journal of Polymer Science: Polymer Physics Edition*, 19:971–981, 6 1981.

[185] F. C. Chen, C. L. Choy, and K. Young. Negative thermal expansion of polymer crystals: Lattice model. *Journal of Polymer Science: Polymer Physics Edition*, 18:2313–2322, 12 1980.

[186] G. K. White and C. L. Choy. Thermal expansion and grüneisen parameters of isotropic and oriented polyethylene. *Journal of Polymer Science: Polymer Physics Edition*, 22:835–846, 5 1984.

[187] N Vasanthan. Crystallinity determination of nylon 66 by density measurement and fourier transform infrared (ftir) spectroscopy. *Journal of Chemical Education*, 89(3):387–390, 2012.

[188] Michael Smith. *ABAQUS/Standard User's Manual, Version 6.9*. Dassault Systèmes Simulia Corp, 2009.

[189] Rickey J Seyler. *Assignment of the glass transition*, volume 1249. Astm International, 1994.

[190] In-Chul Yeh, B Christopher Rinderspacher, Jan W Andzelm, LaShonda T Cureton, and John La Scala. Computational study of thermal and mechanical properties of nylons and bio-based furan polyamides. *Polymer*, 55(1):166–174, 2014.

[191] LG Kazaryan, LA Zezina, and NN Pavlov. Thermal expansion of the crystalline lattice of polyamides. *Polymer Science USSR*, 29(5):1052–1058, 1987.

[192] Robert Hunt, Zakai Olsen, and Kwang Kim. Thermo-mechanical response of the twisted and coiled polymer actuator (tcpa): A finite element analysis (fea). *Smart Materials and Structures*, 30, 6 2021.

[193] A. V. Karavaev, V. V. Dremov, and T. A. Pravishkina. Precise calculation of melting curves by molecular dynamics. *Computational Materials Science*, 124:335–343, nov 2016.

[194] Ebrahim Asadi, Mohsen Asle Zaeem, Sasan Nouranian, and Michael I. Baskes. Two-phase solid-liquid coexistence of Ni, Cu, and Al by molecular dynamics simulations using the modified embedded-atom method. *Acta Materialia*, 86:169–181, mar 2015.

[195] Xiaoxiao Sui, Yongjian Cheng, Naigen Zhou, Binbing Tang, and Lang Zhou. Molecular dynamics simulation of the solidification process of multicrystalline silicon from homogeneous nucleation to grain coarsening. *CrystEngComm*, 20(25):3569–3580, jun 2018.

[196] Avik Mahata and Mohsen Asle Zaeem. Evolution of solidification defects in deformation of nano-polycrystalline aluminum. *Computational Materials Science*, 163:176–185, jun 2019.

[197] Yasushi Shibuta and Toshio Suzuki. A molecular dynamics study of cooling rate during solidification of metal nanoparticles. *Chemical Physics Letters*, 502(1-3):82–86, jan 2011.

[198] H. Y. Zhang, F. Liu, Y. Yang, and D. Y. Sun. The Molecular Dynamics Study of Vacancy Formation during Solidification of Pure Metals. *Scientific Reports*, 7(1):1–8, dec 2017.

[199] Sachin Kurian and Reza Mirzaeifar. Selective laser melting of aluminum nano-powder particles, a molecular dynamics study. *Additive Manufacturing*, 35:101272, oct 2020.

[200] Qi Jiang, Haishun Liu, Jinyan Li, Dengfeng Yang, Yue Zhang, and Weiming Yang. Atomic-level understanding of crystallization in the selective laser melting of Fe50Ni50 amorphous alloy. *Additive Manufacturing*, 34:101369, aug 2020.

[201] Xiaohua Hu, Andrzej Nycz, Yousub Lee, Benjamin Shassere, Srdjan Simunovic, Mark Noakes, Yang Ren, and Xin Sun. Towards an integrated experimental and computational framework for large-scale metal additive manufacturing. *Materials Science and Engineering: A*, 761:138057, 2019.

[202] Guanghua Sui and Ming C Leu. Investigation of layer thickness and surface roughness in rapid freeze prototyping. *J. Manuf. Sci. Eng.*, 125(3):556–563, 2003.

[203] A. V. Müller, G. Schlick, R. Neu, C. Anstätt, T. Klimkait, J. Lee, B. Pascher, M. Schmitt, and C. Seidel. Additive manufacturing of pure tungsten by means of selective laser beam melting with substrate preheating temperatures up to 1000 C. *Nuclear Materials and Energy*, 19:184–188, may 2019.

[204] Hans C Andersen. Molecular dynamics simulations at constant pressure and/or temperature. *The Journal of chemical physics*, 72(4):2384–2393, 1980.

[205] Alex A Samoletov, Carl P Dettmann, and Mark AJ Chaplain. Thermostats for "slow" configurational modes. *Journal of Statistical Physics*, 128(6):1321–1336, 2007.

[206] Peter Mahler Larsen, Søren Schmidt, and Jakob Schiøtz. Robust structural identification via polyhedral template matching. *Modelling and Simulation in Materials Science and Engineering*, 24(5):055007, 2016.

[207] Alexander Stukowski. Visualization and analysis of atomistic simulation data with ovito–the open visualization tool. *Modelling and Simulation in Materials Science and Engineering*, 18(1):015012, 2009.

[208] Alexander Stukowski. Structure identification methods for atomistic simulations of crystalline materials. *Modelling and Simulation in Materials Science and Engineering*, 20(4):045021, 2012.

[209] Daniel Faken and Hannes Jónsson. Systematic analysis of local atomic structure combined with 3D computer graphics. *Computational Materials Science*, 2(2):279–286, mar 1994.

[210] T Koseki and G Thewlis. Overview inclusion assisted microstructure control in c–mn and low alloy steel welds. *Materials Science and Technology*, 21(8):867–879, 2005.

[211] GV Sin'Ko and NA Smirnov. Ab initio calculations of elastic constants and thermodynamic properties of bcc, fcc, and hcp al crystals under pressure. *Journal of Physics: Condensed Matter*, 14(29):6989, 2002.

[212] Maarten De Jong, Wei Chen, Thomas Angsten, Anubhav Jain, Randy Notestine, Anthony Gamst, Marcel Sluiter, Chaitanya Krishna Ande, Sybrand Van Der Zwaag, Jose J Plata, et al. Charting the complete elastic properties of inorganic crystalline compounds. *Scientific data*, 2(1):1–13, 2015.

[213] Ruoqian Liu, Abhishek Kumar, Zhengzhang Chen, Ankit Agrawal, Veera Sundararaghavan, and Alok Choudhary. A predictive machine learning approach for microstructure optimization and materials design. *Scientific reports*, 5(11551):1 – 12, 2015.

[214] Arindam Paul, Pinar Acar, Ruoqian Liu, Wei-Keng Liao, Alok Choudhary, Veera Sundararaghavan, and Ankit Agrawal. Data sampling schemes for microstructure design with vibrational tuning constraints. *AIAA journal*, 56(3):1239–1250, 2018.

[215] Pınar Acar, Veera Sundararaghavan, and Nicholas Fasanella. Multiscale optimization of nanocomposites with probabilistic feature descriptors. *AIAA Journal*, 56(7):2936–2941, 2018.

[216] Gurmeet Singh, Vikas Varshney, and Veera Sundararaghavan. Understanding creep in vitrimers: Insights from molecular dynamics simulations. *arXiv preprint arXiv:2304.05518*, 2023.

[217] Frank Abdi, Amirhossein Eftekharian, Dade Huang, Raul B Rebak, Mohamed Rahmane, Veera Sundararaghavan, Alec Kanyuck, Satyandra K Gupta, Senthil Arul, Vaibhav Jain, et al. Grain boundary engineering of new additive manufactured polycrystalline alloys. *Forces in Mechanics*, page 100033, 2021.

[218] Iman Javaheri, Mohsen Taheri Andani, and Veera Sundararaghavan. Large-scale synthesis of metal additively-manufactured microstructures using markov random fields. *Computational Materials Science*, 206:111228, 2022.

[219] Iman Javaheri and Veera Sundararaghavan. Polycrystalline microstructure reconstruction using markov random fields and histogram matching. *Computer-Aided Design*, 120:102806, 2020.

[220] A Githens, S Ganesan, Z Chen, J Allison, V Sundararaghavan, and S Daly. Characterizing microscale deformation mechanisms and macroscopic tensile properties of a high strength magnesium rare-earth alloy: A combined experimental and crystal plasticity approach. *Acta Materialia*, 186:77–94, 2020.

[221] Mohammadreza Yaghoobi, Zhe Chen, Aeriel D Murphy-Leonard, Veera Sundararaghavan, Samantha Daly, and John E Allison. Deformation twinning and detwinning in extruded mg-4al: In-situ experiment and crystal plasticity simulation. *International Journal of Plasticity*, 155:103345, 2022.

[222] Zhe Chen, Mohammadreza Yaghoobi, Veera Sundararaghavan, John Allison, and Samantha Daly. The effects of microstructure on deformation twinning in mg we43. *Materials Science and Engineering: A*, 859:144189, 2022.

[223] Mohsen Taheri Andani, Aaditya Lakshmanan, Mohammadreza Karamooz-Ravari, Veera Sundararaghavan, John Allison, and Amit Misra. A quantitative study of stress fields ahead of a slip band blocked by a grain boundary in unalloyed magnesium. *Scientific reports*, 10(1):1–8, 2020.

[224] Mohsen Taheri Andani, Aaditya Lakshmanan, Veera Sundararaghavan, John Allison, and Amit Misra. Quantitative study of the effect of grain boundary parameters on the slip system level hall-petch slope for basal slip system in mg-4al. *Acta Materialia*, 200:148–161, 2020.

[225] Aaditya Lakshmanan, Mohammadreza Yaghoobi, Krzysztof S Stopka, and Veera Sundararaghavan. Crystal plasticity finite element modeling of grain size and morphology effects on yield strength and extreme value fatigue response. *journal of materials research and technology*, 19:3337–3354, 2022.

[226] Aaditya Lakshmanan, Mohsen Taheri Andani, Mohammadreza Yaghoobi, John Allison, Amit Misra, and Veera Sundararaghavan. A combined experimental and crystal plasticity study of grain size effects in magnesium alloys. *Journal of Magnesium and Alloys*, 2023.

[227] Mohammadreza Yaghoobi, Sriram Ganesan, Srihari Sundar, Aaditya Lakshmanan, Shiva Rudraraju, John E Allison, and Veera Sundararaghavan. Prismsplasticity: An open-source crystal plasticity finite element software. *Computational Materials Science*, 169:109078, 2019.

[228] Sangmin Lee and Veera Sundararaghavan. Calibration of nanocrystal grain boundary model based on polycrystal plasticity using molecular dynamics simulations. *International Journal for Multiscale Computational Engineering*, 8(5):509–522, 2010.

[229] Ellen LS Solomon, Anirudh Raju Natarajan, Arunabha Mohan Roy, Veera Sundararaghavan, Anton Van der Ven, and Emmanuelle A Marquis. Stability and strain-driven evolution of β' precipitate in mg-y alloys. *Acta Materialia*, 166:148–157, 2019.

[230] Veera Sundararaghavan and Nicholas Zabaras. Weighted multibody expansions for computing stable structures of multiatom systems. *Phys. Rev. B*, 77:064101, Feb 2008.